ZADÁNÍ DIPLOMOVÉ PRÁCE

I. OSOBNÍ A STUDIJNÍ ÚDAJE

Příjmení: **Schmidt** Jméno: **Jaroslav** Osobní číslo: **410210**

Fakulta/ústav: **Fakulta stavební**

Zadávající katedra/ústav: **Katedra mechaniky**

Studijní program: **Stavební inženýrství**

Studijní obor: **Konstrukce pozemních staveb**

II. ÚDAJE K DIPLOMOVÉ PRÁCI

Název diplomové práce:

Experimental and numerical analysis of laminated glass under dynamic loading

Název diplomové práce anglicky:

Experimental and numerical analysis of laminated glass under dynamic loading

Pokyny pro vypracování:

Seznam doporučené literatury:

Jméno a pracoviště vedoucí(ho) diplomové práce:

Ing. Tomáš Janda, Ph.D., katedra mechaniky FSv

Jméno a pracoviště druhé(ho) vedoucí(ho) nebo konzultanta(ky) diplomové práce:

Datum zadání diplomové práce: **02.10.2017** Termín odevzdání diplomové práce: **07.01.2018**

Platnost zadání diplomové práce: _____

Ing. Tomáš Janda, Ph.D. podpis vedoucí(ho) práce	podpis vedoucí(ho) ústavu/katedry	prof. Ing. Alena Kohoutková, CSc. podpis děkana(ky)

III. PŘEVZETÍ ZADÁNÍ

Diplomant bere na vědomí, že je povinen vypracovat diplomovou práci samostatně, bez cizí pomoci, s výjimkou poskytnutých konzultací. Seznam použité literatury, jiných pramenů a jmen konzultantů je třeba uvést v diplomové práci.

. _____ _____

Datum převzetí zadání Podpis studenta

© ČVUT v Praze, Design: ČVUT v Praze, VIC

CZECH TECHNICAL UNIVERSITY IN PRAGUE

Experimental and numerical analysis of laminated glass under dynamic loading

by

Jaroslav Schmidt

A thesis submitted in partial fulfillment for the
degree of Master

in the
Faculty of Civil Engineering
Department of Mechanics

January 5, 2018

Declaration of Authorship

I, JAROSLAV SCHMIDT, declare that this thesis titled, 'Experimental and numerical analysis of laminated glass under dynamic loading' and the work presented in it are my own. I confirm that:

- This work was done wholly or mainly while in candidature for a academic degree at this University.
- Where any part of this thesis has previously been submitted for a degree or any other qualification at this University or any other institution, this has been clearly stated.
- Where I have consulted the published work of others, this is always clearly attributed.
- Where I have quoted from the work of others, the source is always given. With the exception of such quotations, this thesis is entirely my own work.
- I have acknowledged all main sources of help.
- Where the thesis is based on work done by myself jointly with others, I have made clear exactly what was done by others and what I have contributed myself.

Signed: _____

Date: _____

"If you want to find the secrets of the universe, think in terms of energy, frequency and vibration."

Nikola Tesla

CZECH TECHNICAL UNIVERSITY IN PRAGUE

Abstract

Faculty of Civil Engineering
Department of Mechanics

Master's degree

by Jaroslav Schmidt

Laminated glass is layered material, which consist of brittle solid glass layers and polymer viscous interlayer. This composition makes analysis hard and complex. Several simplifying approaches was invented, but little knowledge about its behavior requires performing relatively accurate and demanding analyses. In this paper such one is introduced, where we focus on the dynamic analysis of laminated glass beams and on the analysis of viscous properties of polymer interlayer. The thesis is divided into two parts. The first one is focused on the material description via the generalized Maxwell model introducing the way of extracting data from the rheometer experiment. In this part the calibration process is also introduced. In the second part, the rheometer data for two types of an interlayer ply are used for eigenvalue analysis of three-layered beams, the finite element analysis and the experimental measurement. From the results it is evident, that available measurement methods are very accurate for natural frequency prediction, but not so satisfying for damping estimate. Therefore, the work presents natural vibration analysis methodology for laminated glass beams and introduces problems for further research.

ČESKÉ VYSOKÉ UČENÍ TECHNICKÉ V PRAZE

Abstrakt

Fakulta stavební
Katedra mechaniky

Magisterský stupeň

Jaroslav Schmidt

Lepené sklo je vrstvený kompozitní materiál, který je složen ze skleněných vrstev a viskózních polymerních mezivrstev. Kvůli této vrstvené kompozici je mechanická analýza složitá a časově náročná. V minulosti byla sice vyvinuta řada zjednodušujících metod pro výpočet vlastností lepeného skla, ale stále ještě nedostatečné znalosti o chování tohoto materiálu volají po použití přesných a časově náročných analýz. Tato práce se zaměřuje na provedení takové analýzy. Konkrétně se práce zaměřuje na analýzu vlastního kmitání nosníků z lepeného skla. Práce je rozdělena do dvou základních částí. První se zaměřuje na vytvoření modelu pro popis viskózních vlastností polymerní mezivrstvy. Ta vykazuje silnou časovou a teplotní závislost. Pro správnou kalibraci materiálového modelu jsou použity experimentální data z rheometru. Výstupem z kalibračního procesu je plný popis zobecněného Maxwellova řetězce. Tyto data slouží jako vstupní parametry do následné modální analýzy nosníků, která je součástí druhé části práce. Zde je odvozena a představena jak numerická analýza vlastního kmitání tak i následná experimentální validace. Z výsledků práce je zřejmé, že námi představený numerický model je schopen s velkou přesností predikovat vlastní frekvence nosníků z lepeného skla. Ukázalo se, že předpověď tlumení nedává tak uspokojivé výsledky. Práce tedy představuje modální analýzu dvou typů vrstvených nosníků a představuje problémy pro další výzkum.

Acknowledgements

I would first like to thank my thesis advisor Ing. Tomáš Janda, Ph.D. The door to Dr. Janda office was always opened whenever I ran into a trouble spot or had a question about my research or writing. He consistently allowed this thesis to be my own work, but steered me in the right direction whenever he thought I needed it.

I would also like to acknowledge Prof. Ing. Michal Šejnoha, Ph.D. as the second reader of this thesis, and I am gratefully indebted to him for his very valuable comments on this thesis.

I extend my appreciation to Dr. Plachý for providing us with the results of natural vibration measurements and to Dr. Valentin for allowing us to carry out the viscoelastic measurements.

Finally, I must express my very profound gratitude to my parents and to my fiancée for providing me with unfailing support and continuous encouragement throughout my years of study and through the process of researching and writing this thesis. This accomplishment would not have been possible without them. Thank you.

This work was supported by the Grant Agency of the Czech Technical University in Prague, grant No. SGS17/043/OHK1/1T/11 and by the GACR grant No. GA16-14770S.

Contents

Declaration of Authorship **iii**

Abstract **vii**

Abstrakt **viii**

Acknowledgements **ix**

List of Figures **xiii**

List of Tables **xv**

Abbreviations **xvii**

Symbols **xix**

1 Introduction to laminated glass **1**
1.1 Brief history of glass 1
1.2 Solid glass behavior 1
1.3 Tempered glass 3
1.4 Laminated glass 4
1.5 Laminated glass model 5

2 Dynamic viscoelasticity **9**
2.1 Basic types of connection 9
Kelvin model 10
Maxwell model 11
2.2 Maxwell model under harmonic load 12
2.3 Phasor formulation 15
2.4 Generalized Maxwell model 18
2.5 Parameters identification 20
2.6 Influence of temperature 21

3 Experiments **23**
3.1 Rheometer experiment 23
3.2 Transformation of rheometer output 24

3.3 Calibration of the Maxwell model 26
3.3.1 Linear calibration 27
3.3.2 Nonlinear calibration 28

4 Results from rheometer **29**
4.1 Measurement scenario 29
EVA scenario 29
PVB scenario 30
4.2 Results 30
4.3 Calibration 34

5 Finite element for laminated glass **37**
5.1 Mindlin beam ODE 37
5.2 Weak solution 41
5.3 Discretization 43
5.4 Linear approximation and discussion 45
5.5 Multi-layer model 46
5.6 Viscoelastic beam 49

6 Dynamic analysis **51**
6.1 Natural vibration analysis 51
6.2 Application to elastic-viscoelastic-elastic beams 52
6.3 Numerical solution 53

7 Validation **57**
7.1 Experiment setup 57
7.2 EVA and PVB foil 59

8 Conclusions **63**

A Newton methods **65**

B Gauss-Newton method for fitting **67**

Bibliography **69**

List of Figures

1.1 Stress curve in tip of crack . . . 2
1.2 Glass flaws on surface . . . 2
1.3 Stress distribution along the thickness of prestressed glass beam loaded bending moment . . . 3
1.4 Three-layer laminated glass . . . 4
1.5 Laminated glass kinematics and damage stages in bending . . . 5
1.6 Effective thickness principle diagram . . . 5
1.7 Different types of elements and corresponding FE meshes . . . 6

2.1 Two basic types of rheological connection . . . 9
2.2 Response of strain to constant prescribed stress in the Kelvin model . . . 11
2.3 Response of strain on constant prescribed stress in Maxwell model . . . 12
2.4 Graph of prescribed strain and corresponding stress with all parameters equal zero . . . 14
2.5 Vibration of Maxwell model without transient events . . . 14
2.6 Phasor in complex plane generating sinus wave on real axis . . . 15
2.7 Two phasors in complex plane generating two shifted goniometric functions on real axis . . . 16
2.8 Phasor diagrams for elastic and viscoelastic response . . . 18
2.9 Generalized maxwell model . . . 19
2.10 Storage modulus of one Maxwell cell in frequency domain . . . 20
2.11 Meaning of scale factor in logarithmic scale . . . 21

3.1 Rheometer apparatus . . . 23
3.2 Principal scheme of rheometer . . . 24
3.3 Rheometer setup . . . 25
3.4 Torsional strain . . . 25

4.1 Storage and loss moduli of PVB03 sample in dependence on frequency for two consecutive runs . . . 31
4.2 Storage and loss moduli of EVA07 sample in dependence on frequency for three consecutive runs . . . 32
4.3 Curves for EVA07 sample for temperature 30°C over three consecutive runs 33
4.4 Curves for EVA07 sample for temperature 60°C over three consecutive runs 33
4.5 Curves for PVB03 sample for temperature 30°C and 40°C over three consecutive runs . . . 34
4.6 Mastercurve of storage modulus for specimen with EVA foil for experimental data and curve of mathematical estimation . . . 35

4.7 Mastercurve of storage modulus for specimen with PVB foil for experimental data and curve of mathematical estimation 35
4.8 Mastercurve of EVA foil for all measurement runs. 36

5.1 Reactions on infinitesimal small piece of beam without external forces . . 38
5.2 Deflection of Mindlin beam 40
5.3 Example of two approximation functions in finite element approach 47
5.4 Kinematics of layered multi-node beam 47

7.1 Experimental setup for simulation of free-free boundary conditions 57
7.2 First six mode shapes from MEscopeVES software on tested 3x9 grid . . . 58
7.3 Bandwidth of damped system with 3dB level 59
7.4 Quantile-quantile plots for storage and loss moduli of laminated glass with EVA foil and errors 60
7.5 Quantile-quantile plots for storage and loss moduli of laminated glass with PVB foil and errors 61

A.1 Newton method graphically 65

List of Tables

4.1 Measurement scenario for EVA foil 30
4.2 Measurement scenario for PVB foil 30
4.3 EVA07 parameters 30
4.4 PVB03 parameters 30
4.5 Parameters of generalized Maxwell chain and WLF equation for EVA07 mastercurve 34
4.6 Parameters of generalized Maxwell chain and WLF equation for PVB03 mastercurve 35

7.1 Mechanical properties of solid glass layers 59
7.2 Mechanical properties of EVA foil interlayer 59
7.3 Prony series for EVA and PVB foils 59
7.4 Experiment and numerical results for laminated glass with EVA foil . . . 60
7.5 Experiment and numerical results for laminated glass with PVB foil . . . 60

Abbreviations

FEM	**F**inite **E**lement **M**ethod
FE	**F**inite **E**lement
3D	**3**-**D**imensional
2D	**2**-**D**imensional
1D	**1**-**D**imensional
WLF equation	**W**illiams-**L**andel-**F**erry equation
EVA	**E**thylene-**V**inyl **A**cetate
PVB	**P**oly**V**inyl **B**utyral
ODE	**O**rdinary **D**ifferential **E**quation
DSR	**D**ynamic **S**hear **R**heometer

Symbols

General notation	
f	Scalar
$\boldsymbol{f}$	Column vector
$\mathbf{A}$	Matrix
i	Imaginary unit
p^*	Complex number
$\bullet^{(k)}$	k-th estimation
$\dot{\bullet}$	First time derivative
$\ddot{\bullet}$	Second time derivative
e	Euler number
Viscoelasticity	
G^*	Complex shear modulus
G'	Storage shear modulus
G''	Loss shear modulus
G_∞	Elastic constant of single spring
$\tau(t)$	Shear stress
$\gamma(t)$	Shear strain
$\tau_e(t)$	Shear stress in elastic cell
$\tau_v(t)$	Shear stress in viscous cell
$\gamma_e(t)$	Shear strain in elastic cell
$\dot{\gamma}_v(t)$	Shear strain rate in viscous cell
G	Elastic constant
η	Viscous constant
t_c	Relaxation time
ω	Angular velocity, angular frequency
τ_0	Shear stress amplitude
γ_0	Shear strain amplitude
δ	Phase-shift
$a_R(T)$	Temperature shift factor
T_R	Reference temperature
C_1, C_2	Parameters of WLF equation
Experiments	
γ_s	Shear strain on specimen level
γ_f	Shear strain in interlayer
δ_s	Circumferential displacement of adapter
δ_f	Circumferential displacement of foil
τ_s	Circumferential shear stress on adapter level

τ_f	Circumferential shear stress in foil
h_s	Height of sample
h_f	Height of foil
R_a	Radius of adapter
R_s	Radius of sample
θ	Rotation of adapter
I_p	Polar moment of inertia
P	Transformation coefficient
$\bar{G}'$	Discrete measurements
F	Objective function
$\boldsymbol{\beta}$	Vector of parameters
$\boldsymbol{r}$	Residue vector
$\mathbf{J}$	Jacobian
$\mathcal{F}$	Set of frequencies
$\mathcal{T}$	Set of temperatures

Beam vibration analysis

$N(x,t)$	Normal force
$V(x,t)$	Shear force
$M(x,t)$	Bending moment
I_y	Moment of inertia of cross section
A	Cross section area
$u(x,y,z,t)$	Component of deflection field in x-direction
$w(x,y,z,t)$	Component of deflection field in z-direction
$\phi_y(x,y,z,t)$	Rotation component of deflection field
$\varepsilon_x(x,z,t)$	Normal strain of beam
$\gamma_{zx}(x,t)$	Shear strain of beam
$\kappa_y(x,t)$	Curvature
$\sigma_x(x,z,t)$	Normal stress on cross section
$\tau_{xz}(x,t)$	Shear stress cross section
E	Young'S modulus of elasticity
G	Shear modulus
k	Shear coefficient
A^*	Reduced area by shear coefficient
Ω	Investigated domain
Γ	Boundary of domain
Γ_u	Boundary of domain where deflection is prescribed
Γ_f	Boundary of domain where force is prescribed
$\bar{\bullet}$	Prescribed value
$\phi_y(x,y,z,t)$	Rotation component of deflection field
$\delta\bullet$	Tested function/Virtual displacement
$\boldsymbol{r}$	Vector of nodal displacements
$\delta\boldsymbol{r}$	Virtual nodal displacements
$\mathbf{N}$	Base functions
$\mathbf{B}$	Geometric matrix
$\mathbf{K}$	Stiffness matrix
$\mathbf{M}$	Matrix of generalized masses
$\mathrm{Loc}\langle\bullet\rangle$	Localization function
L	Length of beam element
h_1, h_3	Heights of glass layers

h_2	Thickness of polymer foil
$\mathbf{T}$	Kinematic conditions transformation matrix
$\mathcal{L}$	Lagrangian function
E_p	Potential energy
E_k	Kinetic energy
η	Loss factor
ζ	Damping ratio

Chapter 1

Introduction to laminated glass

Laminated glass is a layered composite material consisting of glass plates and polymer plies. It is useful to understand the reason leading to laminated glass invention to replace the solid glass. Therefore, the history of glass is briefly introduced and the properties of glass are discussed in this section. Laminated glass invention is discussed subsequently.

1.1 Brief history of glass

Glass is present on Earth from time immemorial because volcanic glass obsidian is one of its naturally occurring types. This material is rapidly cooled magmatic rock where only a very limited crystal growth occurred. First type of glass made by human comes from Egypt dated around 3500 BC. Different types of jewellery and vessels were manufactured. Next milestone has taken place in Roman Empire, where clear glass was made and named *glesum* (originator of the word *glass*). At that time, production was difficult task and glass products were luxury goods. Glass pane in window was a sign of great wealth. During the Middle Ages glass expanded and many houses and almost all important sacral buildings had glass windows (in the form of stained glass). It was a progress from the architectural point of view, but glass still did not play any structural role. In 20th century, new types of glass were invented, for example toughened or tempered glass, the wire glass and finally the laminated glass. The Principle and properties of laminated glass are described in section 1.4 in greater detail. For now, it is sufficient to note that the idea of laminated glass made it possible to think about glass as structural element. More information about the history of glass can be found e.g. in [1] or [2].

1.2 Solid glass behavior

Laminated glass is a complicated material for description, therefore it is important to properly investigate the behavior of individual parts. The behavior of solid glass, which particularly leads to invention of tempered and laminated glass, is discussed in this section.

Glass is almost purely elastic material with relatively high strength. In virtual experiment on perfect solid glass cube without defects under uniaxial load, the result would be the

same stiffness and strength in tension as in compression. Unfortunately, when we do real experiment, strength in tension is significantly smaller than in compression. This phenomenon is caused by various initial defects on the surface and can be explained by stress concentration.

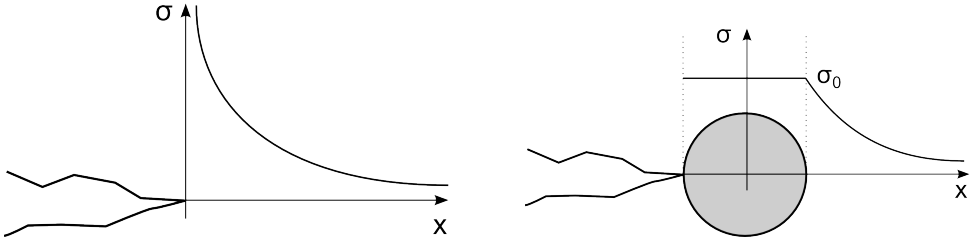

(A) Elastic material (B) Elastoplastic material

FIGURE 1.1: Stress curve in tip of crack

Glass is solid and perfectly homogeneous material at first look, but actually there are microscopic flaws and defects on the plate surface. If the material is capable of plastic yielding then the plastic zone in the crack tip is created, see figure 1.1b. In plastic zone there is a constant level of stress, therefore growth of crack is prevented by force balance. Unfortunately, glass is an elastic material and has almost zero yield capacity. Thus the stress close to the crack tip increases, see figure 1.1a. Inglis [3] showed that stress in the root is a function of the crack tip curvature. In glass, crack is very sharp (curvature near infinite) and stress also goes to infinity at the crack root. Fortunately, at the tips of real glass defects the stress is not infinite and the glass handles certain stress level before collapse. Stress concentration problem appears only when the tensile stress is applied. For compressive force, cracks are closed and stress is transmitted by contact. This fact is illustrated in figure 1.2. Therefore, stress concentration at tip cause orderly smaller strength in tension against compression. Theoretically, compression strength is equal to material point strength.

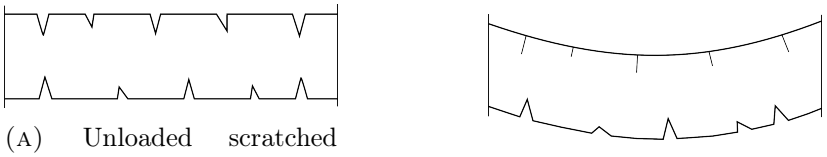

(A) Unloaded scratched beam (B) Loaded scratched beam

FIGURE 1.2: Glass flaws on surface

Similar stress distribution arises when glass material is loaded by force acting on small area. If the force is larger than the material point strength, glass is not capable to balance internal and external forces. In the theoretical case of concentrated force acting on an infinitesimal area, the stress grows to infinity because of non yielding capacity. In this and the previous case, glass behaves elastically until it reaches certain limit in strength. After that, the material collapses without warning. Such behavior is termed fragility or brittleness.

The limited strength was the reason why glass was used only as window infill and not as a load bearing structural material. This has changed with the invention of tempered glass which is discussed in the next section.

1.3 Tempered glass

We discussed earlier, that microscopic cracks reduce the glass strength. To partially eliminate this effect it is possible to modify the initial stress in the glass plane. As shown above, the stress concentration appears only in tension while compression state is favorable. Idea is a preload table of glass by specific tempering.

If glass is heated to 620-675°C [4] in furnace and then rapidly cooled, non zero stress appears along the thickness. Surface will be compressed compared to the middle core which will be in tension. The stress distribution σ_T after cooling is illustrated in Figure 1.3. The figure also shows the stress σ_F corresponding to a positive bending moment acting on the cross section. It is obvious that preloading improves the bending capacity of a glass beam.

The initial state is a properly heated table with a uniform temperature in each point. If cooling process starts, the surface layers are cooled earlier and begin to shrink (tension appears). During first few seconds there is a reverse effect than we want. But after temperature of oven reaches the transition temperature, the surface solidifies and the core is still in a viscous state. In this phase the relaxation is taking place in the middle of the table and the stress is reversed to a required state. Finally, the rest will also cool down and the stress from Figure 1.3 is imprisoned inside.

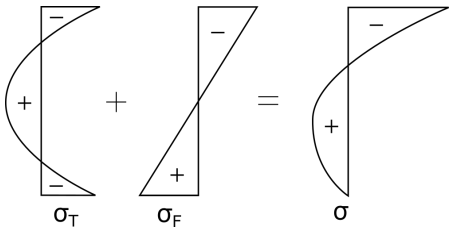

FIGURE 1.3: Stress distribution along the thickness of prestressed glass beam loaded bending moment

Although tempered glass has higher strength, it has a different post-breakable behavior. When a common glass collapses, the crack appears and the stored elastic energy is dissipated. Glass tables normally bursts in several large cracks pattern. On the other hand, prestressed glass stores a certain amount of energy before loading which leads to post-breakable pattern consisting of a large number of relatively harmful pieces. The stored energy also leads to impossibility of post processing cutting or hole drilling in tempered glass. All geometric modification must be done before tempering.

As was explained, the tempered glass is efficient material due to a higher strength in tension but – quid pro quo – the tempered glass has a different post-breakable behavior and a "brittle" glass core. This type is yet better for glass beams and other structural construction, but if the beam fails, the tempered glass does not handle any load and construction completely fails. To improve a post-breakable behavior, the laminated glass was invented.

1.4 Laminated glass

Laminated glass is a layered composite material containing several solid glass layers and polymer interlayers. In this paper we restrict our attention to three-layer beams, which scheme and photo of composition is in Figure 1.4.

(A) Scheme (B) Photo

FIGURE 1.4: Three-layer laminated glass

Laminated glass was invented in automobile industry where it was used for car windscreens. If car is in motion, dynamic impacts of small objects frequently occurs and the glass is susceptible to damage. Increasing strength by tempered glass is not the solution, because when glass still bursts, pieces in form of shard could fly into cabin and hurt someone. These dangers motivated the invention of laminated glass which keeps post-breakable pieces together by transparent polymer interlayer. Laminated glass has many advantages and is an appealing material mainly due to transparency. From automobile industry this invention was extended to other sectors including civil engineering. Laminated glass began to be used as structural elements. Examples include roof, facade, floor systems, columns, staircases, etc.

Polymer ply bonding two glass tables together significantly changes kinematics of the beam and the failure mode. In pure tension and compression (without considering buckling) the interlayer is active, but its effect is negligible. Therefore, we will focus only on bending in the following. To define bounds lets imagine two limit cases: monolithically bonded beams and two beams without cohesion. These two types are illustrated in Figure 1.5a. Top beam represents monolithically bonded tables, where one table carries compression and the other transfers the tension load. On the other hand, bottom beam represents two loosely laid beams where tables are bending independently and the zero shear transmission causes a zero interaction. The image in the middle of Figure 1.5a represents the laminated glass beam where two rigid glass plates are bonded by a flexible ply. This interlayer is not as stiff as glass. Consequently, a monolithic beam and beam without cohesion are boundary cases and the laminated glass behavior is somewhere between. From picture it is obvious that the dominant deformation of a polymer ply is shear. That is why we focus on the shear material parameters of the interlayer in the rest of the text.

The main advantage of laminated glass is the improvement of post-failure behavior. Phases of damage are illustrated in Figure 1.5b. If failure criterion is not exceeded, both glass tables are in elastic state and the stress distribution follows the Hooke law. This is the phase A from Figure 1.5b. Due to interlayer interaction, the stress in glass around a polymer ply is smaller than in the outer surface, which means that in the bottom surface the maximum tension stress is reached. If a critical load exceeds the threshold, the bottom glass plate breaks. Crack commonly passes across the whole thickness. Glass pieces are held together by interlayer, but rigidity of composite suddenly

decreases. Interlayer is loaded by tension and the bending moment is carried by top glass table. This phase is labeled as B in Figure 1.5b. In the third phase, labeled C in the figure, the top table is also damaged and the load is transferred by the interlayer only. In case of float glass, intact polymer ply and the contact compressive stress in damaged glass can transfer some moment. In case of tempered glass, pieces of broken glass are small and the transition of compressive stress is limited. Due to a negligible bending stiffness of the interlayer the completely broken tempered glass behaves like a membrane and only axial tension is transferred.

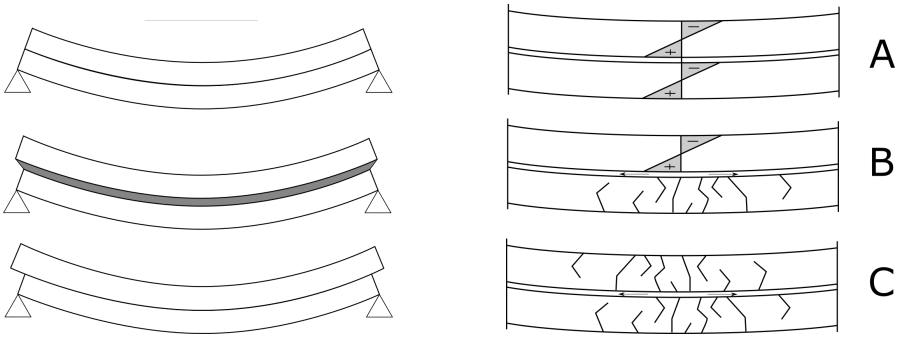

(A) Kinematic of beam (B) Phases of damage

FIGURE 1.5: Laminated glass kinematics and damage stages in bending

1.5 Laminated glass model

To get a sense about glass, a general behavior was presented. Now, we can introduce individual approaches and models for a description of the behavior.

The laminated glass is a complicated and complex material (literally – we will see later when phasor arithmetic is introduced). Solid glass is almost perfectly elastic isotropic material and can be described by two constants, for example E, ν or G and ν. Polymer ply is time and temperature depend at least. For time dependence we utilize theory of viscoelasticity [5] and for temperature we employ the time-temperature superposition concept. Details about viscoelasticity will be discussed in the next chapter. By assuming these theories, the description of the material becomes more challenging. Analytical solution can be obtained only for special cases. For dynamic loading, where complex numbers are used, the closed form solutions are unknown for practically all problems. This impossibility leads to the development of easy-to-use approaches, such as effective thickness concept, which also fulfills needs of engineering practice.

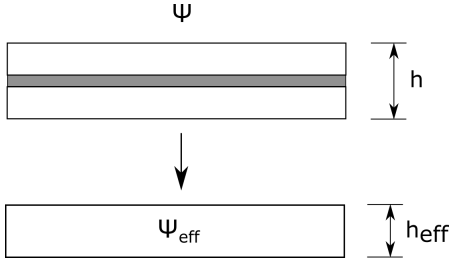

FIGURE 1.6: Effective thickness principle diagram

Generally, effective thickness approaches search for thickness of simple (mostly isotropic and homogeneous) material, which has the same selected property as the original material. For laminated glass it usually means that we search for effective thickness h_{eff} of a monolithic solid glass beam, which have similar certain property, e.g. bending stiffness or natural frequencies, close to the value of laminated beam. Therefore, we approximate property Ψ by effective Ψ_{eff}, mathematically denoted as

$$\Psi \approx \Psi_{eff}\left(h_{eff}\left(\mathcal{G}, \mathcal{M}, \mathcal{B}\right)\right),$$

where $\mathcal{G}$ is a set of geometric parameters and $\mathcal{M}$ a set of material parameters of an laminated glass and $\mathcal{B}$ is a set of parameters, which includes boundary conditions. Principle diagram of a laminated glass effective thickness is illustrated in Figure 1.6.

Two basic types of load and response are investigated: static and dynamic. For static, several effective thickness approaches was developed with satisfactory results. For example, Gallupi's effective thickness [6] for the prediction of deflection and stress based on variational principle. In dynamics we usually solve problems of eigenvalues, eigenvectors and damping of the system. For this task, there is only a few effective thickness approaches. One for eigen-value problems is the dynamic effective thickness from López-Aenlle, Pelayo [7]. For natural frequencies prediction this is approach relatively satisfying but it can not reliably predict damping of a laminated glass beam. Recently, a new dynamic effective thickness [8], which can also predict damping with satisfactory accuracy was introduced based on the Gallupi approach.

Effective thickness approaches are useful tool, but it is not panacea. In special cases or for validation of different approaches, it can be necessary to employ more accurate methods. Impossibility to derive close form solutions leads to the use of numerical methods, such as FEM which follows modern scientific trend.

There is always possibility to use 3D elements for discretization of laminated glass plates. This leads, however, to large number of unknown if we want to maintain certain proportionality between elements size. It is caused by the small thickness of the interlayer due to the overall thickness. This type of mesh is very schematically illustrated in Figure 1.7a. To reduce the number of elements, it is convenient to use more specialized element which includes informations about all layers. This type of multi-layered discretization is again schematically illustrated in Figure 1.7b. From comparison of these types it is obvious that though multi-layered element has more degrees of freedom, it still provides a significant reduction of total number of unknowns. Such type of super element for laminated glass was introduced for example in [9].

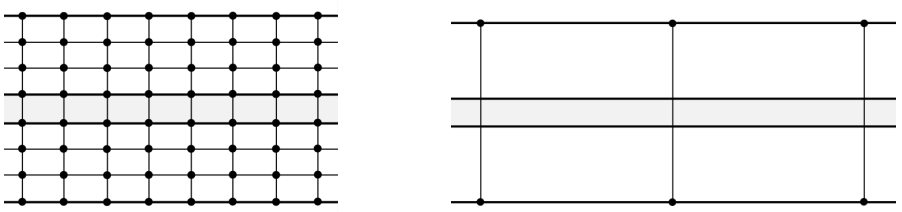

(A) Mesh over thickness (B) Mesh with layered elements

FIGURE 1.7: Different types of elements and corresponding FE meshes

Both approaches (effective thickness and FE analysis) depend on a set of material parameters $\mathcal{M}$. Glass is described by two elastic constants, but interlayer is viscoelastic and must be described by series of parameters. In this paper it is assumed that polymer ply can be characterized by the generalized Maxwell chain extended by WLF equation for temperature dependence. This model requires at least four (realistically about twenty) free parameters, which need to be specified. In the following chapters the viscoelastic model is outlined and the way how to calibrate its parameters from dynamic experiment is described.

Chapter 2

Dynamic viscoelasticity

Many construction materials have stable properties in time and their behavior can be described by several parameters that are constant in time. This is most often caused by fact, that atoms in crystalline grid are in equilibrium and their position is given by potential of atomic, electrostatic and external forces, which must be minimal. However, a typical interlayer in laminated glass is a polymer composed of mutually intertwined polymer chains [10] and time-dependent behaviors occur due to different chain transformations under constant external force.

A material point from axial tensile test can be conceptually represented by single spring with parameter, which corresponds to elastic Young modulus E. It turns out that we can used this so called rheological segments also for time-dependent material models. For theory of viscoelasticity, one more segment apart from spring must be added. The missing link is damper, which keeps the constant ratio between the stress and deformation rate. So, if we act on damper with a constant force, deformation increases linearly in time. If we use only one damper for the characterization of material point, we get ideal Newtonian fluid, but it does not meet requirements for polymers. Therefore, it is appropriate to use combination of several rheological segments.

2.1 Basic types of connection

It is important to understand, that viscoelasticity is engaged only for polymer interlayer, where shear deformation is dominant, recall Figure 1.5a. Thats why shear parameters for rheological models are used. Mentioned rheological schemes always represent material point behavior under axial load.

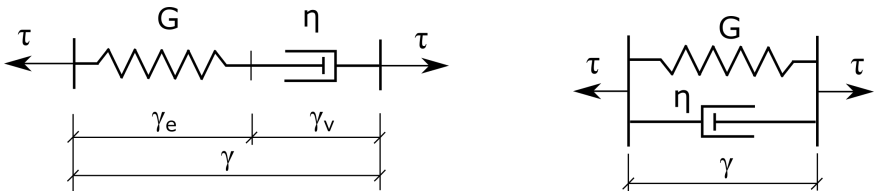

(A) Maxwell model (B) Kelvin model

FIGURE 2.1: Two basic types of rheological connection

In the next text, variables or parameters with lower index e correspond to elastic members, meanwhile lower index v belongs to a damper. Members without index represent behavior of the whole cell. In addition, indexing will be apparent from the following two equations, which are identical for all rheological models. The behavior of a single spring is intuitive. Spring is described by one parameter G, which is coefficient of proportionality between the shear deformation γ_e and the stress τ (both functions of time), thus

$$\tau_e(t) = G\gamma_e(t). \tag{2.1}$$

Similar relationship exist for damper, but it represents Newtonian fluid as mentioned above, so the parameter η which is associated with this member is the coefficient of proportionality between the shear stress τ_v and the rate of deformation $\dot{\gamma}_v$, thus

$$\tau_v(t) = \eta\dot{\gamma}_v(t), \tag{2.2}$$

where the dot denotes differentiation by time. Further properties are already dependent on a connection scheme.

Kelvin model The first type of material model is composed of one damper and one spring in parallel connection, see Figure 2.1b. The behavior is evident from a simple thought experiment, when we try to imagine the response of the model and after that we introduce mathematical equations. We apply force on the boundary of Kelvin cell and because both members are deformed simultaneously and the damper cannot deform immediately, the strain is zero at the beginning of such an experiment. On the other hand, if the time goes to infinity the damper deformation can grow infinitely but spring is limited by $\hat{\tau}/G$, where $\hat{\tau}$ is the prescribed stress. The observation is that after prescribing force, first few moments the contribution of the damper prevails and the deformation grows almost linearly. Later, the contribution of the spring becomes more relevant and the strain evolves to the final value $\hat{\tau}/G$. The mathematical solution confirm this conception. Condition of continuity and the equilibrium condition have the following form

$$\tau(t) = \tau_e(t) + \tau_v(t), \tag{2.3}$$

$$\gamma(t) = \gamma_e(t) = \gamma_v(t). \tag{2.4}$$

Combining of equation (2.3) with properties of members (2.1) and (2.2) and applying the continuity condition (2.4) the following differential equation of relationship between stress and strain for Kelvin cell is obtained

$$\tau(t) = G\gamma_e(t) + \eta\dot{\gamma}_v(t) = G\gamma(t) + \eta\dot{\gamma}(t). \tag{2.5}$$

For the validation of results of the thought experiment, we set the strain as an unknown function and the stress as the prescribed function, which is zero to time t_0, jumps up to $\hat{\tau}$ in time t_0 and is kept constant in times $t > t_0$. For simplicity, we choose $t_0 = 0$. For uniqueness of the solution in every time, we set the stress in time $t = t_0$ as $\hat{\tau}$. The differential equation now has the form

$$\gamma(t) + \frac{\eta}{G}\dot{\gamma}(t) = \frac{\hat{\tau}}{G}, \tag{2.6}$$

and the appropriate solution for time $t \geq 0$ becomes

$$\gamma(t) = \frac{\hat{\tau}}{G}\left(1 - \exp\left(-\frac{G}{\eta}t\right)\right). \tag{2.7}$$

For time $t < 0$, a trivial solution is only permissible. Solution (2.7) is plotted in Figure 2.2 in dimensionless units. If we compare mathematical solution (2.7) with our thought experiment, we get match.

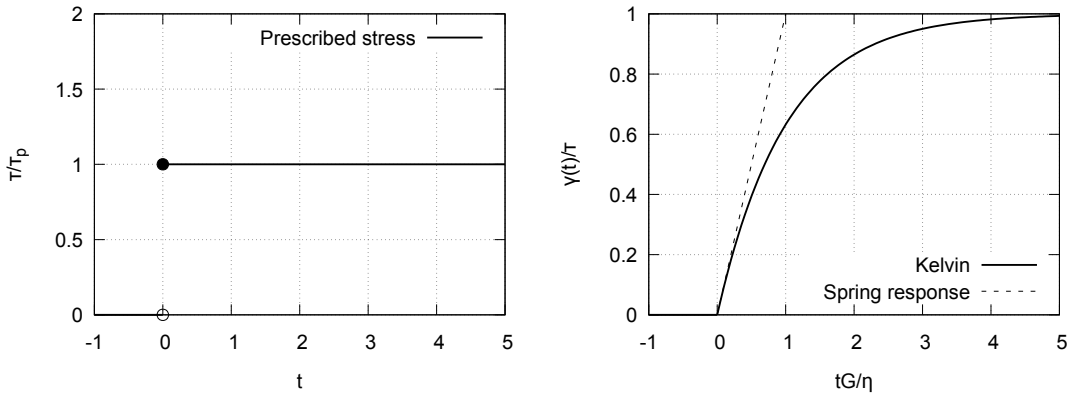

(A) Evolution of prescribed stress (B) Respond strain diagram

FIGURE 2.2: Response of strain to constant prescribed stress in the Kelvin model

Maxwell model The second type of material model is serial connection of damper and spring, see Figure 2.1a. We start with thought experiment again. On the boundary of Maxwell cell we prescribe force at a particular time and since then we keep this force constant. In the first moment, the damper is not deformed and all responding deformation belongs to the spring. Spring responds immediately to the applied stress by a sudden increase in the elastic strain. Since spring is stretched, its deformation does not increase anymore. In this configuration, there is no deformation restrictions, so the deformation of damper linearly increases in time after the mentioned deformation jump. We can write it mathematically. From continuity and equilibrium conditions we get

$$\tau(t) = \tau_e(t) = \tau_v(t), \tag{2.8}$$

$$\gamma(t) = \gamma_e(t) + \gamma_v(t). \tag{2.9}$$

Equation (2.9) with conditions (2.1), (2.2) and (2.8) while considering a sudden increase of the applied stress $\hat{\tau}$ in time $t \geq 0$ can be rewritten as

$$\gamma(t) = \hat{\tau}\left(\frac{1}{G} + \frac{t}{\eta}\right). \tag{2.10}$$

If we consider a trivial solution in time $t < 0$, than discontinuity in function $\gamma(t)$ occurs at time $t = 0$. This is consistent with our assumption about jump increase of deformation. Solution (2.10) is plotted in Figure 2.3.

Both material models are useful, however both have different field of application. From graph in Figures 2.2 and 2.3 it may seem that the Kelvin model is better due to its continuous and exponential course of deformation. This is true for modeling creep, where the stress is prescribed. But for relaxation problem this is exactly the opposite.

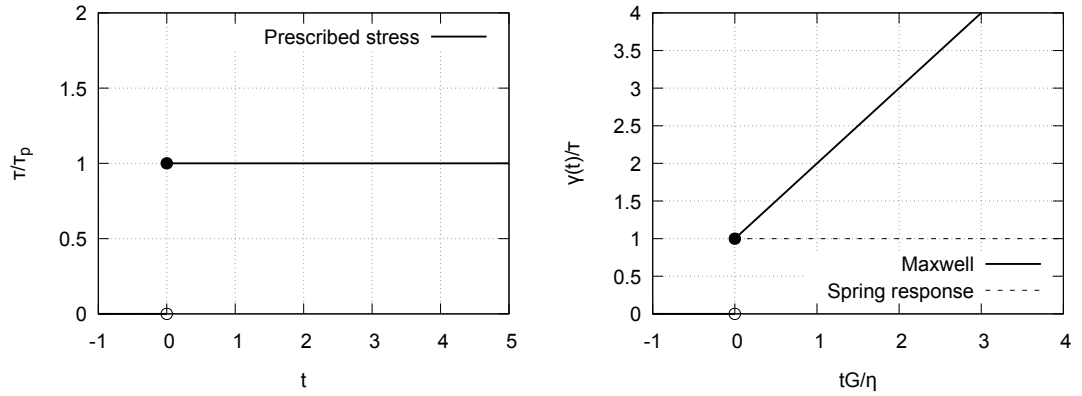

(A) Evolution of prescribed stress (B) Evolution of corresponding strain

FIGURE 2.3: Response of strain on constant prescribed stress in Maxwell model

In this case, the deformation is prescribed and the responding stress is unknown and behavior analysis leads to the exponential course for the Maxwell model. It follows that for polymer, where relaxation plays an important role, the Maxwell model is more suitable. In the following text, where the dynamic load is applied to the rheological model, only the Maxwell model will be employed. More about general viscoelasticity can be found in [5].

2.2 Maxwell model under harmonic load

Goal of this section is to describe the behavior of the Maxwell model under dynamic harmonic loading and to show that this problem naturally leads to a solution involving complex numbers. Firstly, we reformulate differential equation for the Maxwell model from equations (2.8) and (2.9) to a form with general load $\gamma(t)$

$$\dot{\tau}(t) + \frac{G}{\eta}\tau(t) = G\dot{\gamma}(t). \tag{2.11}$$

Solution of equation (2.11), where $\tau(t)$ is unknown function and $\gamma(t)$ is prescribed, is strongly dependent on the right hand side. Firstly, we investigate the homogeneous solution. We assume that the modulus G is non-zero. For the zero right hand side it holds

$$\dot{\gamma}(t) = 0, \forall t \tag{2.12}$$

Consequently $\gamma(t) = \text{const} = \hat{\gamma}$. It is evident that the homogeneous solution is equal to the static solution with constant strain prescribed. Equation (2.11) with condition (2.12) is the first order homogeneous differential equation with constant coefficients and its solution by [11] is given in the form

$$\tau(t) = Ce^{-\frac{G}{\eta}t} = Ce^{-\frac{t}{t_c}} = \tau_h(t). \tag{2.13}$$

The constant C will be quantified later. In equation (2.13) we define $t_c := \eta/G$, which is so called the relaxation time. Its physical meaning can be understood from graph 2.2b.

Let us review differential equation (2.11) again. The main topic of thesis is dynamic loading and vibrations. This means that it is important to understand the behavior of

the Maxwell model under the prescribed harmonic deformation. We assume that for times $t \leq 0$ the deformation $\gamma(t) = 0$ is prescribed and only trivial solution occurs. For time $t > 0$ the harmonic loading is prescribed in the form

$$\gamma(t) = \gamma_0 \sin \omega t, \tag{2.14}$$

where ω is the angular velocity and γ_0 is the strain amplitude. The time evolution (2.14) is plotted in Figure 2.4 by the solid line assuming $\omega = 1$ and $\gamma_0 = 1$. The strain rate reads

$$\dot{\gamma}(t) = \gamma_0 \omega \cos \omega t. \tag{2.15}$$

Combining (2.15) and (2.11) leads to the inhomogeneous differential equation in the form

$$\dot{\tau}(t) + \frac{G}{\eta}\tau(t) = G\gamma_0 \omega \cos \omega t. \tag{2.16}$$

Because of linearity of equation (2.16), a general solution can be obtained as a summation of the homogeneous solution (2.13) and some particular solution. It is difficult to get general particular solution only from properties of equation and therefore we try to limit solution space to 2 dimensions. We do that by requiring particular solution in form

$$\tau_p(t) = A \sin \omega t + B \cos \omega t. \tag{2.17}$$

If identity (2.17) is substituted to (2.16) and compared trigonometric coefficients, system of linear equations is obtained. By solving this linear system an unique particular solution is obtained from space of functions (2.17), where parameters A and B are set as

$$A = \frac{\omega^2 t_c^2}{\omega^2 t_c^2 + 1} G\gamma_0, \tag{2.18}$$

$$B = \frac{\omega t_c}{\omega^2 t_c^2 + 1} G\gamma_0, \tag{2.19}$$

where we used definition of relaxation time t_c. Finally, particular solution is

$$\tau_p(t) = \frac{\omega^2 t_c^2}{\omega^2 t_c^2 + 1} G\gamma_0 \sin \omega t + \frac{\omega t_c}{\omega^2 t_c^2 + 1} G\gamma_0 \cos \omega t \tag{2.20}$$

and total solution $\tau(t) = \tau_h(t) + \tau_p(t)$ with initial condition $\tau(t = 0) = 0$ takes form

$$\tau(t) = \frac{\omega^2 t_c^2}{\omega^2 t_c^2 + 1} G\gamma_0 \sin \omega t + \frac{\omega t_c}{\omega^2 t_c^2 + 1} G\gamma_0 \cos \omega t - \frac{\omega t_c}{\omega^2 t_c^2 + 1} G\gamma_0 e^{-\frac{t}{t_c}}, \tag{2.21}$$

where we define two parameters G' and G''

$$G' := \frac{\omega^2 t_c^2}{\omega^2 t_c^2 + 1} G, \tag{2.22}$$

$$G'' := \frac{\omega t_c}{\omega^2 t_c^2 + 1} G, \tag{2.23}$$

so

$$\tau(t) = G'\gamma_0 \sin \omega t + G''\gamma_0 \cos \omega t - G''\gamma_0 e^{-\frac{t}{t_c}}, \tag{2.24}$$

Its physical meaning will be demonstrated later. Solution (2.21) is plotted in graph 2.4 for time around $t = 0$. Until strain is zero, also responding stress is zero. Since

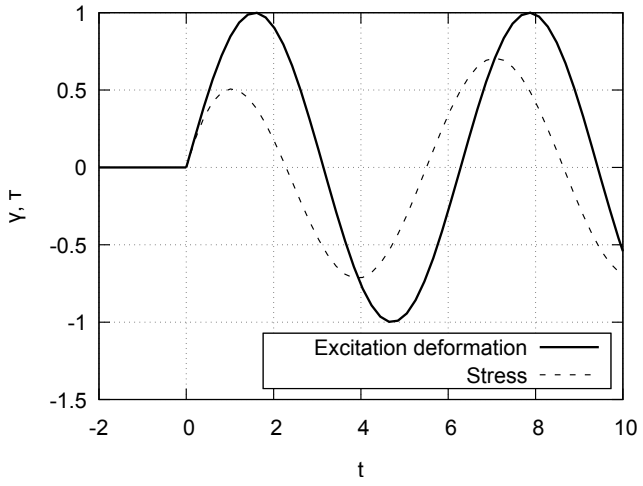

FIGURE 2.4: Graph of prescribed strain and corresponding stress with all parameters equal zero

prescribed strain is excited, corresponding stress also starts to oscillate, but not at regular intervals and not with regular amplitudes. This phenomenon is visible at the beginning of excitation in graph and is called transient event. It is caused by a sudden change of state of the system. In this thesis, only eigen-oscillations are investigated, so the behavior during transient events is irrelevant. It can also be evident from mathematical solution (2.21), where the transient event disappears in the limit case $t \to \infty$, when last member in (2.21) goes to zero. This fact is important in the next section, where the complex numbers for harmonic vibrations are employed and the complex number notation can not take into account the transient events. Oscillation functions for the Maxwell cell in a theoretical point $t \to \infty$ is plotted in Figure 2.5.

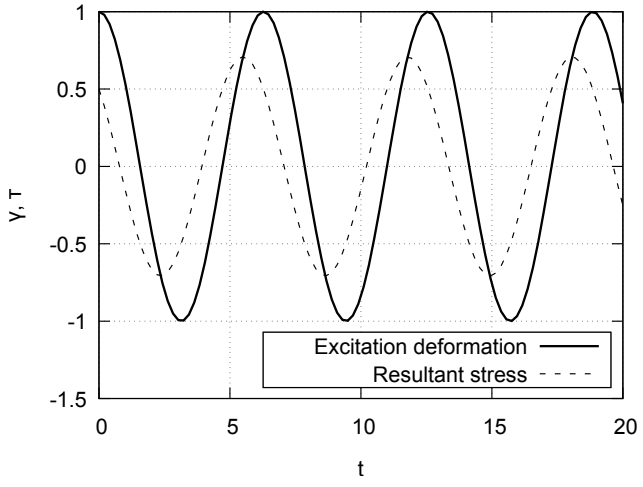

FIGURE 2.5: Vibration of Maxwell model without transient events

In this point, we try to understand the meaning of individual members from equation (2.21) only by intuition. For example, we can assume for a while, that the model is ideally elastic. This assumption leads to the idea that the stress must be described also only by sine function as strain. Second member in equation (2.21) disappears. Now from the rest of equation it is obvious that member G' plays the role of elastic modulus. If the

second member from (2.21) is not zero but small, then the superposition of sine signal with high amplitude and cosine signal with low amplitude cause small phase shift of the resultant stress. When cosine coefficient increases, the phase shift increases. Thus, it can be said, that the cosine member corresponds to damping of model and therefore G'' controls the energy dissipation. It turns out that this conception is correct.

2.3 Phasor formulation

In this section the notion of phasor for vibration description is introduced. Phasor represents a vector in the complex plane which rotates with a constant angular frequency around the origin. Each phasor is characterized by a constant magnitude and by the position in a frozen time. The position can be a complex number which implies that the phasor is also a complex number in general. The phasors are mainly used for vibrations and harmonic motions because if we project a rotating vector to the real axis in dependence on time, we get a goniometric function. This can be evident from Figure 2.6, where unusually the real axis is represented in the vertical direction.

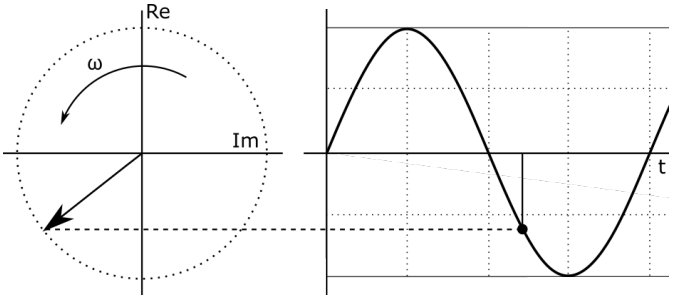

FIGURE 2.6: Phasor in complex plane generating sinus wave on real axis

If the phasor generates a sine wave to the real axis, than it generates a cosine wave to the complex axis, it corresponds to Euler equation [11]

$$e^{\mathrm{i}x} = \cos x + \mathrm{i}\sin x. \tag{2.25}$$

This means that the rotating vector with angular velocity ω and amplitude A can be expressed with respect to (2.25) as $Ae^{\mathrm{i}\omega t}$. This formula, where amplitude $A \in \mathbb{C}$ is phasor, represents one rotating vector in the complex plane, see again 2.6. The phasor is still a complex number, so all algebra taken from the theory of complex numbers is unchanged. In the next text the theory of viscoelasticity is formulated using phasors. In this section complex numbers are denoted with asterisk.

We can express the prescribed strain (2.14) as

$$\gamma(t) = \mathrm{Re}(\gamma_0 e^{\mathrm{i}\omega t}). \tag{2.26}$$

The right hand side generates a cosine wave with the amplitude γ_0. Here we are using cosine function for the excited load, which affects the transient event only and has no influence on the harmonic response. It is convenient to remove the real part operator and write the strain in the complex form. This transfers the task to the complex plane and after an arbitrary analysis, the real result is obtained as a real part of the resultant

complex number. So the generalized prescribed complex strain is

$$\gamma^*(t) = \gamma_0^* e^{\mathrm{i}\omega t} = \gamma_0 e^{\mathrm{i}\omega t}. \tag{2.27}$$

The corresponding stress can be expressed analogically. Particular solution (2.17) can be generalized as

$$\tau^*(t) = \tau_0^* e^{\mathrm{i}\omega t} = (B - \mathrm{i}A) e^{\mathrm{i}\omega t}, \tag{2.28}$$

where the phasor τ_0^* is complex. Particular solution (2.17) can be obtained as a real part of the above equation, thus

$$\tau(t) = \mathrm{Re}(\tau^*(t)). \tag{2.29}$$

Equations (2.27) and (2.28) generate two generally different rotating vectors in the complex plane. These vectors have different amplitude and also different angular position but must have the same angular velocity. Example of this situation is plotted in Figure 2.7. There two phasors generate two harmonic curves with the phase shift between theirs peaks.

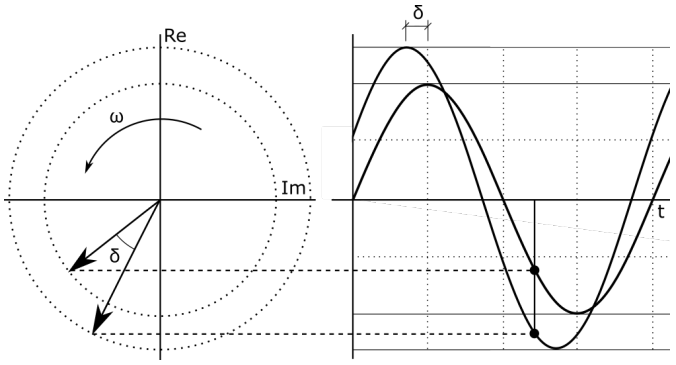

FIGURE 2.7: Two phasors in complex plane generating two shifted goniometric functions on real axis

Now, we can define complex modulus G^* as a proportion of the stress and strain phasors. Thus

$$G^* := \frac{\tau_0^* e^{\mathrm{i}\omega t}}{\gamma_0 e^{\mathrm{i}\omega t}} = \frac{\tau_0^*}{\gamma_0}. \tag{2.30}$$

Parameter (2.30) does not rotate, so it is not a phasor, but it is still a complex number which relates the strain and stress phasors analogous to "Hooke's law" $\tau^* = G^*\gamma^*$. Fraction τ_0^*/γ_0 cannot be enumerate because the complex stress τ^* is unknown. Missing information are contained in the differential equation of the Maxwell model. To arrive at the solution in the complex form it is necessary to express the time derivative of the complex strain and stress as

$$\dot{\gamma}^*(t) = \mathrm{i}\omega\gamma_0^* e^{\mathrm{i}\omega t}, \tag{2.31}$$

$$\dot{\tau}^*(t) = \mathrm{i}\omega\tau_0^* e^{\mathrm{i}\omega t}. \tag{2.32}$$

Now, equations (2.31) and (2.32) can be substituted into differential equation (2.11). We obtain

$$\mathrm{i}\omega\tau_0^* e^{\mathrm{i}\omega t} + \frac{G}{\eta}\tau_0^* e^{\mathrm{i}\omega t} = G\mathrm{i}\omega\gamma_0^* e^{\mathrm{i}\omega t}. \tag{2.33}$$

Here, we used definition (2.30), so the complex modulus is a fraction of stress and strain phasor, where phasor members $e^{\mathrm{i}\omega t}$ are reduced and we get

$$G^* = \frac{\tau^*}{\gamma^*} = \frac{\tau_0^* e^{\mathrm{i}\omega t}}{\gamma_0 e^{\mathrm{i}\omega t}} = \frac{\tau_0^*}{\gamma_0} = G\frac{\mathrm{i}\omega t_c}{\mathrm{i}\omega t_c + 1}. \tag{2.34}$$

To convert the expression of standard shape $z^* = z^r + \mathrm{i}z^i$, it must be expanded by the formula $\mathrm{i}\omega t_c - 1$. It results in

$$G^* = G\frac{\mathrm{i}\omega t_c}{\mathrm{i}\omega t_c + 1} \cdot \frac{\mathrm{i}\omega t_c - 1}{\mathrm{i}\omega t_c - 1} = G\frac{\omega^2 t_c^2}{\omega^2 t_c^2 + 1} + \mathrm{i}G\frac{\omega t_c}{\omega^2 t_c^2 + 1}. \tag{2.35}$$

Note that the real and the imaginary parts of G^* are equal to G' defined in (2.22) and G'' defined in (2.23), respectively. The first quantity is known as the *storage modulus* and the second one as the *loss modulus*. The naming is derived from the physical meaning of the moduli. The storage modulus corresponds to the stored energy (elastic behavior) and the loss modulus corresponds to the lost energy dissipated as heat (viscous behavior). The total complex modulus is therefore

$$G^* = G' + \mathrm{i}G'', \tag{2.36}$$

where

$$G' = \mathrm{Re}(G^*), \quad G'' = \mathrm{Im}(G^*). \tag{2.37}$$

In this case, the storage and loss moduli are a function of internal parameters of the Maxwell cell and of angular velocity. If we want to know the resultant stress, we multiply the phasor of the prescribed strain by the modulus G^*. In this thesis, it appears useful to solve the inverse problem, where we know the strain and stress amplitudes with various frequencies, for finding internal parameters. For this tasks, it is convenient to express the storage and loss moduli in other way.

From Figure 2.7 it is evident that the evolution of responding stress looks like a harmonic function. Indeed, each linear combination of sine and cosine members with the same angular velocity can be overwritten as a single harmonic function shifted in time. Thus, the stress can be rewritten to

$$\tau(t) = \tau_0 \cos(\omega t + \delta), \tag{2.38}$$

where τ_0 is the amplitude of stress and δ is the phase shift. So it says, that the stress corresponds to deformation, but with a different amplitude and is delayed by δ. We can generalize this idea to phasor formulation, so

$$\tau^*(t) = \tau_0 e^{\mathrm{i}(\omega t + \delta)} = \tau_0 e^{\mathrm{i}\omega t} e^{\mathrm{i}\delta}. \tag{2.39}$$

We recall definition (2.30), which leads to formula for the complex modulus

$$G^* = \frac{\tau^*}{\gamma^*} = \frac{\tau_0 e^{\mathrm{i}\omega t} e^{\mathrm{i}\delta}}{\gamma_0^* e^{\mathrm{i}\omega t}} = \frac{\tau_0}{\gamma_0} e^{\mathrm{i}\delta}. \tag{2.40}$$

If we project modulus (2.40) to real and imaginary axis, we get relationships, which evaluate the storage and loss moduli from the strain and stress amplitudes and its phase

shift. The projection to real axis is

$$G' = \frac{\tau_0}{\gamma_0} \cos \delta. \tag{2.41}$$

And by the projection to complex plane we obtain

$$G'' = \frac{\tau_0}{\gamma_0} \sin \delta. \tag{2.42}$$

With this identities, we can investigate the geometric interpretation of the storage and loss modulus. Firstly, we assume an elastic response, so the rotating vectors have zero phase shift and the corresponding phasors are real. This phasor diagram is illustrated in Figure 2.8a. In this case, the strain and stress have the same direction in the complex plane, so the complex modulus is equal to the elastic one and it holds $G = \tau_0/\gamma_0$. For viscoelastic response, the situation is more interesting. In diagram (2.8b), stress phasor is turned by δ due to strain. Now we can decompose the phasor of τ^* to the direction of γ^* and to the direction perpendicular to γ^*. First one represents the same situation as for the elastic case, recall Figure 2.8a, and fraction of this component and magnitude of strain amplitude corresponds to equation (2.41). This confirms our expectation, that storage modulus is connected with elastic behavior. Second member, corresponding to equation (2.42), can not affect the magnitude of stress amplitude because it is perpendicular to the stress phasor. So, energy associated with this component is lost. This is why this member is called the loss modulus.

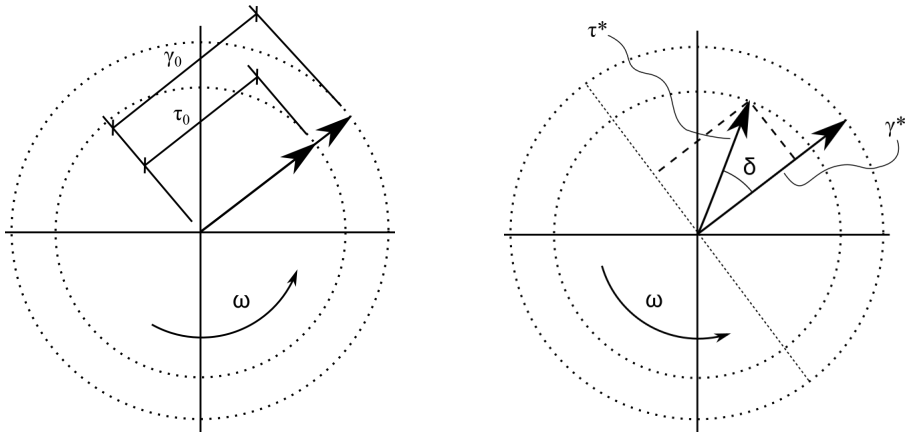

(A) Elastic (B) Viscoelastic

FIGURE 2.8: Phasor diagrams for elastic and viscoelastic response

2.4 Generalized Maxwell model

It turns out that a single Maxwell cell is not flexible enough for a general description of viscous material such as polymers. Luckily, assembling several Maxwell cells in parallel chain can better describe complex viscoelastic materials. This model is called the generalized Maxwell model (or Prony series) and is illustrated in Figure 2.9.

If we want to find the relation between harmonic stress and strain, we again must find the storage and loss modulus, generally the complex modulus G^*. The approach based

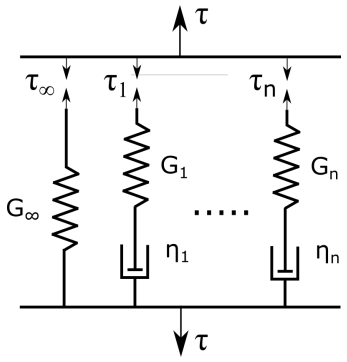

FIGURE 2.9: Generalized maxwell model

on calculation of equations (2.41) and (2.42) remains unchanged, because equations are derived regardless of the internal construction of the material model. But equations (2.35) no longer applies to the whole system. We re-examine some aspects from a simple Maxwell model, but with application of phasors. If we prescribe deformation, every segment is deformed equally. Therefore,

$$\gamma_0^* e^{\mathrm{i}\omega t} = \gamma_{0,\infty} e^{\mathrm{i}\omega t} = \gamma_{0,i}^* e^{\mathrm{i}\omega t}, \tag{2.43}$$

where $i = 1, 2 \dots n$ is the number of a viscoelastic branch, $\gamma_{0,\infty} e^{\mathrm{i}\omega t}$ is the strain of the elastic branch and $\gamma_{0,i}^* e^{\mathrm{i}\omega t}$ is the complex strain of the i-th branch.

Second types of equations are equilibrium conditions. As evident from Figure 2.9 the total stress of the Maxwell chain is a sum of stresses in individual Maxwell units. We get condition

$$\tau_0^* e^{\mathrm{i}\omega t} = \tau_{0,\infty} e^{\mathrm{i}\omega t} + \sum_{i=1}^{n} \tau_{0,i}^* e^{\mathrm{i}\omega t}. \tag{2.44}$$

Adopting Hooke's law on the first term and equation (2.30) on summands we get following identity

$$\tau_0^* e^{\mathrm{i}\omega t} = G_\infty \gamma_{0,\infty} e^{\mathrm{i}\omega t} + \sum_{i=1}^{n} G_i^* \gamma_{0,i}^* e^{\mathrm{i}\omega t}. \tag{2.45}$$

Assuming (2.43) it is possible to rewrite equation (2.45) as

$$\tau_0^* e^{\mathrm{i}\omega t} = \left(G_\infty + \sum_{i=1}^{n} G_i^* \right) \gamma_0^* e^{\mathrm{i}\omega t} = G^* \gamma_0^* e^{\mathrm{i}\omega t}. \tag{2.46}$$

So we can define the complex modulus for the generalized Maxwell model as

$$G^* = G_\infty + \sum_{i=1}^{n} G_i^*. \tag{2.47}$$

The storage and the loss modulus of the generalized Maxwell model is obtained as real and imaginary part of the complex modulus, respectively. Thus

$$G' := \mathrm{Re}(G^*) = G_\infty + \sum_{i=1}^{n} G_i \frac{\omega^2 t_{c,i}^2}{\omega^2 t_{c,i}^2 + 1}, \tag{2.48}$$

$$G'' := \mathrm{Im}(G^*) = \sum_{i=1}^{n} G_i \frac{\omega t_{c,i}}{\omega^2 t_{c,i}^2 + 1}. \tag{2.49}$$

2.5 Parameters identification

The dynamic behavior of the generalized Maxwell model is described by dynamic modulus, which gives the stress response. For full description, we need to determine all free parameters in the model. These parameters are the set of elastic moduli $G_1, \ldots, G_n$ and the set of relaxation times $t_{c,1}, \ldots, t_{c,n}$. For simplicity, we denote the first set as $\{G_i\}$ and the second as $\{t_{c,i}\}$. Relaxation time $t_{c,i}$ can be investigated as free parameter, but this leads to multi-criteria optimization during parameters identification. However, relaxation time has a physical meaning of time of interest. This can be seen from the following example. We assume one Maxwell unit and we want to quantify the storage modulus in the frequency domain. The result of this task in the logarithm scale is displayed in Figure 2.10, where only the shape is important. The curve has predictive value in the center, around frequency equal to 1, but farther from the center, say for the value above 10 and below 0.1, the curve is very flat and the predictive value is low. The frequency of center point, in this case 1, corresponds to the selected value of the relaxation time. If we want to investigate neighborhood of another frequency, we just change the relaxation time t_c. But, if the domain of interest is unacceptably large, we can not describe it by one Maxwell cell and we need to add another cell with a different value of t_c.

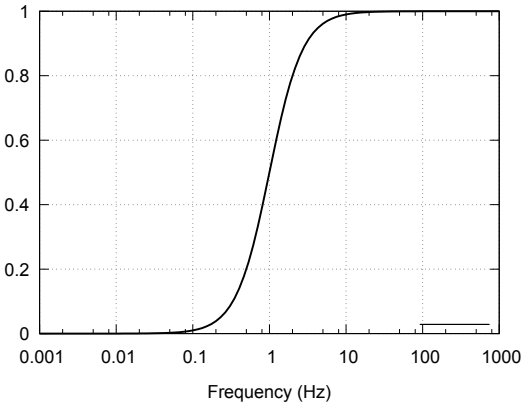

FIGURE 2.10: Storage modulus of one Maxwell cell in frequency domain

Consequently, the set of relaxation times $\{t_{c,i}\}$ can be chosen based on the frequency domain of interest. This simplifies the identification of parameters $\{G_i\}$.

There is one more advantage of the Maxwell model, which is worth mentioning. We derived the relation for complex modulus in the previous sections. We found that the complex modulus is a function of internal parameters $\{G_i\}$. Mathematically written

$$G^*(\omega) = G'(\omega) + \mathrm{i}G''(\omega) = G^*(G_\infty, G_1, \ldots, G_n). \tag{2.50}$$

In addition, the solution in the time domain has the form given by equation (2.51). We present it without proof

$$G(t) = G_\infty + \sum_{i=1}^{n} G_i e^{t/t_c} = G(G_\infty, G_1, \ldots, G_n). \tag{2.51}$$

From form (2.51) it is obvious that it is also a function of internal moduli $\{G_i\}$. So, the use of this generalized Maxwell model suggests that we can describe not only the vibration problem, but also each time-dependent model by these set of $\{G_i\}$. Question stay how gain this parameters. One possible way is get it from experiments by calibration. In next sections, we discuss one type of dynamic experiment which can provide the complex modulus for a laminated glass interlayer and we also discuss the data processing for the identification of parameters of Maxwell model.

2.6 Influence of temperature

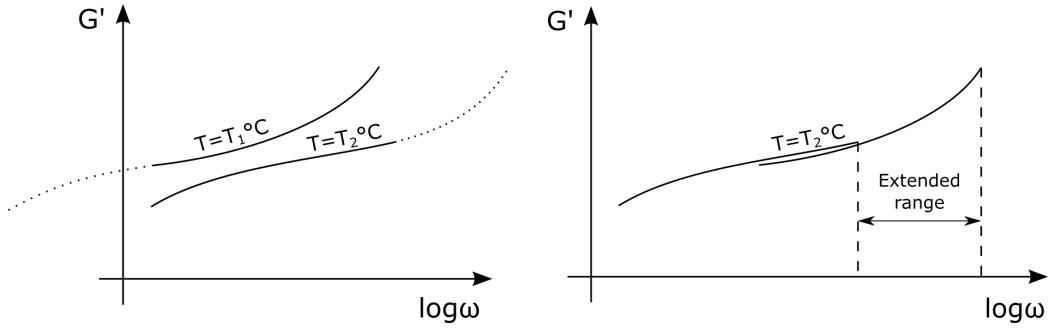

(A) Before shifting (B) After shifting

FIGURE 2.11: Meaning of scale factor in logarithmic scale

The interlayer is a polymer, which is strongly dependent on temperature. For the description of temperature dependency we follow the time-temperature superposition principle [10]. This concept presumes that the storage and loss moduli depend not only on frequency but also on temperature. If the material has some mechanical property $\mu(t, T)$ a function of time and temperature, we can simplify the relation by binding time and temperature via factor a_T expressed for a chosen temperature T_R. So the property $\mu(a_T \cdot t, T_R)$ is a function of time only. Applying this concept to our frequency analysis we get a similar relationship but with inverse use of the shift factor. So for the complex modulus G^* it holds

$$G^*(\omega, T) = G^*(a_R(T) \cdot \omega, T_R), \tag{2.52}$$

where shift factor $a_R(T)$ is

$$a_R(T) = \frac{1}{a_T(T)} \tag{2.53}$$

Equation (2.52) represents the scale transformation of modulus G^*, but it is more convenient to think in logarithmic scale, where the shift factor cause only shifting of curves, see Figure 2.11. For calculation of shift factor, we use empirical relation called the Williams-Landel-Ferry (WLF) equation [12], which has the following form

$$\log a_R(T) = \left(\frac{-C_1(T - T_R)}{C_2 + T - T_R} \right), \tag{2.54}$$

where log is a decadic logarithm, C_1 and C_2 are free parameters available for calibration and T_R is reference temperature. Two shifted curves for the complex modulus are illustrated in Figure 2.11a. But from experiments we get only part of this curve, this is indicated in picture by the solid line. If we performed shifting, see Figure 2.11b, we get new continuous curve for one reference temperature, but with extended domain. This larger one is called the mastercurve. Consequently, evaluating the shift factor not only brings a full description of the temperature influence, but also suppling points with high and low frequencies which are difficult to obtained experimentally.

Next, we assume that the polymer foil is fully described by the generalized Maxwell model and the WLF equation. The free model parameters are calibrated from experimental data.

Chapter 3

Experiments

In the previous chapter, we introduced the model for laminated glass interlayer. Because it is a viscous time-depend material, we employed the generalized Maxwell chain for the description of the material point behavior. This model has many free parameters (one for each unit of the Maxwell chain) and it is necessary to calibrate them for a particular material. To do this we can use the data from either static or dynamic experiments. We prefer to use the dynamic tests because they fully describe thermorheological properties of the polymer interlayer. Other types of experiments are discussed for example in [13]. In this thesis, we are dealing with rheometer experiment only. This type of experiment was introduced in [14] and we perform tests in this course.

3.1 Rheometer experiment

(A) Rheometer HAASE MARS

(B) Laminated glass specimen in rheometer

FIGURE 3.1: Rheometer apparatus

A rheometer is an apparatus, which measures viscous properties of liquids or solids. There are two different types of rheometers, distinguished according to the prescribed parameter. Rotational rheometer prescribes shear stress or strain, whereas extensional type prescribes normal tension or compression. For experiments presented in this paper

we used rotational shear rheometer, type DSR (Dynamic shear rheometer). Specifically, the rheometer HAASE MARS photographed in Fig. 3.1a, was used. Figure 3.2 shows the basic principle of this type of apparatus. A sample is placed between two plates. Bottom plate, hatched in the picture, is fixed and the top plate, filled by solid gray, is movable. The top plate is called the adapter. A harmonic torque is applied to the upper plate and the device monitors the induced strain. The applied torque corresponds to picture 3.2, so the adapter rotates about vertical axis, which is perpendicular to horizontal plate. We assume that only the shear strain appears in the sample in such experiment configuration.

The polymer ply is a material which is also very strongly temperature depend, so we need test specimens under a representative temperature range. Rheometer HAASE MARS does not have temperature chamber and only the bottom plate can be heated or cooled. This is not obstacle, because we can insulate the sample and the adapter by some additional teflon case, which helps to maintain a stable temperature inside. Disadvantage is, that we must wait until the temperature field is stationary within the sample.

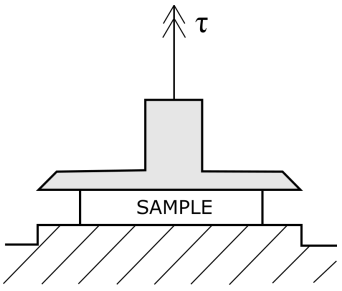

FIGURE 3.2: Principal scheme of rheometer

Our goal is to obtain the complex modulus G^* of the polymer layer. The processing software computes the complex modulus based on the known diameter of the adapter and its known distance from the base plate. The sample of the laminated glass, however, has different geometry so we have to adjust the value. The apparatus prescribes a harmonic, for example sine, evolution of the stress and records the corresponding strain. From this two recorded harmonic signals the software extracts amplitudes of the stress and strain and also the phase shift δ. With these quantities the evaluation of the complex modulus is straightforward

$$G^* = G' + \mathrm{i}G'' = \frac{\tau_0}{\gamma_0}\cos\delta + \mathrm{i}\frac{\tau_0}{\gamma_0}\sin\delta, \tag{3.1}$$

where index 0 represent amplitude of a given quantity.

However, processing software expects a linear strain distribution over the entire height of the sample. This assumption is adequate for asphalt mixtures, for which the rheometer DSR was designed, but it is not fullfiled for laminated glass and therefore the value of the complex modulus produced by the device has to be adjusted. Fortunately, the transformation procedure is straightforward. It is derived in the next section.

3.2 Transformation of rheometer output

Dynamic shear type of rheometer is mostly used for asphalts mixtures, for which mounting the sample is simple task. Asphalt is heated and a drop of liquid mixture is put on

bottom plate. Appropriate height of the sample is set by the user and a vertical shift of the upper plate spreads asphalt between horizontal plates (see Fig. 3.3a). In this case, the asphalt specimen has the same diameter as the upper adapter and a linear distribution of strain along the height can be assumed. From Figure 3.3b it is evident, that this assumption does not hold for the laminated glass sample. Due to a high difference in stiffness of glass and polymer it is justifiable to neglect the deformation of glass and assume that all strain occur in the interlayer. The strain has a linear distribution over the thickness of the ply.

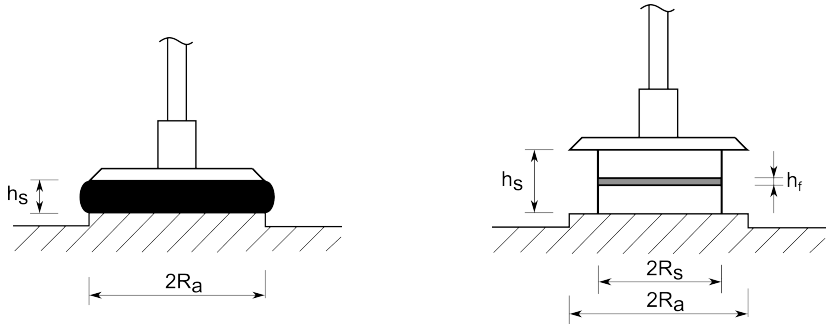

(A) Asphalt setup (B) Laminated glass setup

FIGURE 3.3: Rheometer setup

Further adjustment is necessary because one of the rheometer input parameter is circumferential stress, but the specimen is loaded by the prescribed torque, which is calculated from this value. This means that if the laminated glass sample has smaller radius than the adapter (see Figure 3.3b), different torque is evaluated. It should be obvious that we need to transform the data for both the thickness and radius. For the derivation of transformation equation, we start from the relation between torques and rotations in upper surface. The derivation of the transformation formula is based on the theory of elasticity.

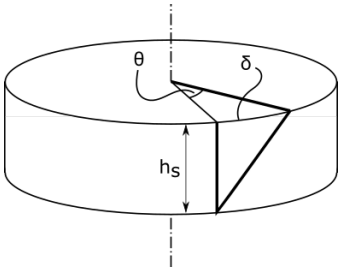

FIGURE 3.4: Torsional strain

Rheometer software is aware of the radius of adapter R_a and the height of the whole sample h_s from geometry and position of adapter. In case of asphalt sample, if we imagine rotation of the upper plate about angle θ whilst lower plate is fixed, see Figure 3.4, peripheral shear strain is given by equation

$$\gamma_s(t) = \frac{\delta_s(t)}{h_s} = R_a \frac{\theta(t)}{h_s}. \tag{3.2}$$

For the laminated glass sample we further assume that the glass deformation is zero, so the same rotation θ generates the strain in the plastic interlayer, which is different from

(3.2) in general. Foil has height h_f and radius R_s, so the shear strain reads

$$\gamma_f(t) = \frac{\delta_f(t)}{h_s} = R_s \frac{\theta(t)}{h_f}. \tag{3.3}$$

In equations (3.2) and (3.3) θ is rotation. We want the relation between strains assuming rotations be the same. Combining these equations yields the relation between γ_s and γ_f in the form

$$\gamma_f(t) = \gamma_s(t) \frac{R_a}{R_s} \frac{h_s}{h_f}. \tag{3.4}$$

One of the input is the prescribed circumferential stress. The software recalculates this value into torque T. Relation between torque T and circumferential stress τ_s follows from theory of elasticity [15] and is provided by

$$T(t) = \frac{\tau_s(t) I_p}{R_a} = \frac{\tau_s(t)}{R_a} \frac{1}{2} \pi {R_a}^4. \tag{3.5}$$

If the same torque is applied to the sample with smaller radius R_f, it holds

$$T(t) = \frac{\tau_f(t) I_p}{R_s} = \frac{\tau_f(t)}{R_s} \frac{1}{2} \pi {R_s}^4. \tag{3.6}$$

Again, combining equations (3.5) and (3.6) gives

$$\tau_f(t) = \tau_s(t) \frac{{R_s}^3}{{R_f}^3}. \tag{3.7}$$

We already mentioned that the rheometer calculates the complex modulus from equation (3.1). In terms of phasors, we can rewrite this equation as

$$G_s^* = \frac{\tau_{0,s}}{\gamma_{0,s}} e^{\mathrm{i}\delta}, \tag{3.8}$$

where $\tau_{0,s}$ is the amplitude of $\tau_s(t)$ and $\gamma_{0,s}$ is the amplitude of $\gamma_s(t)$. But, we need to calculate the modulus from foil values $\tau_{0,f}$ and $\gamma_{0,f}$. For reformulating, we used equations (3.4) and (3.7). The complex modulus of the foil then reads

$$G_f^* = \frac{\tau_{0,f}}{\gamma_{0,f}} e^{\mathrm{i}\delta} = \frac{\tau_{0,s}}{\gamma_{0,s}} \frac{{R_s}^4}{{R_f}^4} \frac{h_f}{h_s} e^{\mathrm{i}\delta} = \frac{{R_s}^4}{{R_f}^4} \frac{h_f}{h_s} G_s^* = G_s^* \cdot P(R_a, R_s, h_s, h_f). \tag{3.9}$$

Therefore, the desired modulus G_f^* can be obtained by multiplying the reometer modulus G_s^* by factor $P(R_a, R_s, h_s, h_f)$, which depends on radii and heights.

3.3 Calibration of the Maxwell model

From the experiments, we get the complex modulus in form $\overline{G}^*(\omega, T) = \overline{G}'(\omega, T) + \mathrm{i}\overline{G}''(\omega, T)$ for each measured temperature and frequency. We denote measured values with bar. Now, when we have this data, we can use it for the identification of free parameters of the material model. This is an important step because the data are discrete per and can not be directly used in further analysis.

3.3.1 Linear calibration

Calibration of shear moduli $\{G_i\}$ and G_∞ from measured pairs $\overline{G}'$ and $\overline{G}''$ for one specific temperature leads to linear fitting problem. It is caused by linearity of equations (2.48) and (2.49), to recall

$$G'(\omega) = G_\infty + \sum_{i=1}^{n} G_i \frac{\omega^2 t_{c,i}^2}{\omega^2 t_{c,i}^2 + 1}, \tag{3.10}$$

$$G''(\omega) = \sum_{i=1}^{n} G_i \frac{\omega t_{c,i}}{\omega^2 t_{c,i}^2 + 1} \tag{3.11}$$

where n is the number of viscoelastic Maxwell cells.

Calibration of parameters of a linear system is very straightforward and the presented solution follows [16]. The objective function, which is minimized is chosen to be the sum of squares of residues between the point on a theoretical curve and the discrete measured value. So the objective function is

$$F(\{G_i\}, G_\infty) := \sum_{j=1}^{m} \left(G'(\omega_j) - \overline{G}'_j \right)^2 + \sum_{j=1}^{m} \left(G''(\omega_j) - \overline{G}''_j \right)^2, \tag{3.12}$$

where m is the number of discrete measurements and $\overline{G}'_j$ and $\overline{G}''_j$ are the values obtained from experiments for frequency ω_j.

Minimizing condition for the objective function based on calculus have the following general form

$$\frac{\partial F}{\partial G_\infty} = 0, \frac{\partial F}{\partial G_i} = 0, i = 1, \ldots, n. \tag{3.13}$$

Specifically, for the objective function (3.12), we get

$$\frac{\partial F}{\partial G_\infty} = \sum_{j=1}^{m} 2 \left(G'(\omega_j) - \overline{G}'_j \right) = 0, \tag{3.14}$$

$$\frac{\partial F}{\partial G_i} = \sum_{j=1}^{m} 2 \left(G'(\omega_j) - \overline{G}'_j \right) \frac{\omega^2 t_{c,i}^2}{\omega^2 t_{c,i}^2 + 1} + \sum_{j=1}^{m} 2 \left(G''(\omega_j) - \overline{G}''_j \right) \frac{\omega t_{c,i}}{\omega^2 t_{c,i}^2 + 1} = 0. \tag{3.15}$$

Minimizing conditions (3.14) and (3.15) is linear in parameters and can be solved explicitly. If we arrange unknown parameters to vector $\boldsymbol{\beta}^\mathsf{T} = \{G_1, G_2, \cdots, G_n, G_\infty\}$ we can formulate this system of linear equation in the form

$$\mathbf{A}\boldsymbol{\beta} = \boldsymbol{b}, \tag{3.16}$$

where components of the system matrix $\mathbf{A}$ and the right side vector $\boldsymbol{b}$ are following

$$A_{i,j} = \sum_{k=1}^{m} \frac{t_{c,i}^2 \omega_k^2}{1 + t_{c,i}^2 \omega_k^2} \frac{t_{c,j}^2 \omega_k^2}{1 + t_{c,j}^2 \omega_k^2} + \sum_{k=1}^{m} \frac{t_{c,i} \omega_k}{1 + t_{c,i}^2 \omega_k^2} \frac{t_{c,j} \omega_k}{1 + t_{c,j}^2 \omega_k^2}, \tag{3.17}$$

$$A_{i,n+1} = A_{n+1,i} = \sum_{k=1}^{m} \frac{t_{c,i}^2 \omega_k^2}{1 + t_{c,i}^2 \omega_k^2}, \tag{3.18}$$

$$A_{n+1,n+1} = m, \tag{3.19}$$

$$b_i = \sum_{k=1}^{m} \frac{t_{c,i}^2 \omega_k^2}{1 + t_{c,i}^2 \omega_k^2} \overline{G}'_k + \sum_{k=1}^{m} \frac{t_{c,i} \omega_k}{1 + t_{c,i}^2 \omega_k^2} \overline{G}''_k, \tag{3.20}$$

$$b_{n+1} = \sum_{k=1}^{m} \overline{G}'_k. \tag{3.21}$$

Solution of (3.16) gives the optimal set of $\{G_i\}$ and G_∞.

3.3.2 Nonlinear calibration

When we want to include influence of temperature, we must also calibrate parameters C_1 and C_2 from equation (2.54), but WLF equation is nonlinear in its free parameters. Since we want to avoid the approximate approach based of visually shifting the curves into a single master curve we utilize the coupled method, presented in [17], for fitting all parameters of the model, i.e. the elastic moduli and the parameters C_i. This method finds one mastercurve for the chosen reference temperature. Consequently, the vector of parameters $\boldsymbol{\beta}$ is expanded by two members, thus

$$\boldsymbol{\beta}^\mathsf{T} = \{G_\infty, G_1, G_2, \ldots, G_n, C_1, C_2\}. \tag{3.22}$$

For better implementation of the solution method, we introduce the vector of residuals $\boldsymbol{r}$, which contains residuals of a theoretical curve and the measured data. Formally

$$\boldsymbol{r}^\mathsf{T}(\boldsymbol{\beta}) = \{\{G'(\omega_i a_T(T_i)) - \overline{G}'_i\}, \{G''(\omega_i a_T(T_i)) - \overline{G}''_i\}\}, i = 1, \ldots, m. \tag{3.23}$$

Again, we minimize the objective function F, which is defined as a sum of squares of the residuals. It can be represented by scalar dot product of two vectors $\boldsymbol{r}$, thus

$$F(\boldsymbol{\beta}) := \boldsymbol{r}(\boldsymbol{\beta})^\mathsf{T} \boldsymbol{r}(\boldsymbol{\beta}). \tag{3.24}$$

The objective function (3.24) looks similar to linear fitting case. But now, the vector of residuals $\boldsymbol{r}$ contains the shift factor a_T, which is nonlinearly dependent on C_1 and C_2. We want still to minimize the objective function F, but the solution can not be found in the closed form. We employed the Gauss-Newton method [11], which iteratively finds the minimum of the objective functions in form (3.24). We only introduce this method here, the derivation of relations can be found in appendix A. Iterations start from point $\boldsymbol{\beta}^{(0)}$ and each next step is evaluated from identity

$$\boldsymbol{\beta}^{(s+1)} = \boldsymbol{\beta}^{(s)} - \left(\mathbf{J}^\mathsf{T}\mathbf{J}\right)^{-1} \mathbf{J}^\mathsf{T} \boldsymbol{r}(\boldsymbol{\beta}^{(s)}), \tag{3.25}$$

where $\mathbf{J}$ is the Jacobian matrix of the residual vector $\boldsymbol{r}$

$$\mathbf{J} = \frac{\partial}{\partial \boldsymbol{\beta}} \boldsymbol{r}(\boldsymbol{\beta}^{(s)}). \tag{3.26}$$

Each iterative step is fully determined by identities (3.25) and (3.26). Listing of items of the Jacobian matrix can be found in appendix B together with the implementation pseudocode.

Chapter 4

Results from rheometer

The theoretical background of the rheometer measurements and the Maxwell model calibration was introduced in the previous section. In this section we present the results of real experiments performed on laminated glass with two types of polymer foils.

Samples for rheometer tests are typically cylindrical. Samples were drilled out of from the laminated glass plate. It is preferable option, because polymer ply might change its properties during the lamination process and it has a different behavior in the laminated and unlaminated state. Samples are 20 mm in diameter with typical heights of layers about 5/0.76/5 mm. Some variability of total thickness in orders of 10^{-2} mm was observed and it is attributed to the variability of foil thickness only. Two types of polymer plies were tested. First is the ethylene-vinyl acetate (EVA) foil and second is the polyvinyl butyral (PVB) ply. Description of chemistry of these polymers is out of scope of this thesis. We only note, that these two materials belong to the most common polymers used in the laminated glass.

4.1 Measurement scenario

We measured several samples from each polymer type with similar scenarios. Basic set of frequencies, which the sample was subjected to, is the following

$$\mathcal{F} = \{0.001, 0.005, 0.01, 0.05, 0.1, 0.5, 1.0, 5.0, 10.0, 20.0, 30.0, 40.0, 50.0\}[\text{Hz}]$$

and the temperature set is

$$\mathcal{T} = \{10°\text{C}, 20°\text{C}, 30°\text{C}, 40°\text{C}, 50°\text{C}, 60°\text{C}\}.$$

EVA scenario In next pseudo table the measurement scenario for EVA foil type is introduced. In day zero, the sample was glued to rheometer by high stiffness epoxid glue. This type was ideal, because it creates only a small layer of glue between the sample and adapter. In post processing, we assume that no deformation occurs in this negligible layer. We have to wait until glue hardens, so the measurements started the next day. So called the first measurement run was performed firstly, when the sample was heated up to one of temperature from $\mathcal{T}$ and measurement was performed over each frequency. This

DAY 0:	Sample EVA was glued to rheometer
DAY 1:	1^{st}run: Measurement of sample loaded by temperature set $\mathcal{T}$ and harmonic strains with frequencies $\mathcal{F}$
DAY 2:	2^{nd}run: Measurement of sample loaded by temperature set $\mathcal{T}$ and harmonic strains with frequencies $\overline{\mathcal{F}}$
DAY 3:	3^{rd}run: Measurement of sample loaded by temperature set $\mathcal{T}$ and harmonic strains with frequencies $\overline{\mathcal{F}}$

TABLE 4.1: Measurement scenario for EVA foil

procedure was repeated for each temperature. The second and third run were performed in the same manner, but over smaller frequency set

$$\overline{\mathcal{F}} = \mathcal{F} \backslash \{0.001, 0.005\}.$$

Each run was carried out within one day. Over night, the specimen was always left without heating, exposed to room temperature only. The scenario for EVA foil is summarized in table 4.1.

PVB scenario The second run is over smaller set of frequencies, because the measurement for frequencies 0.001 and 0.005 Hz is time-consuming and moreover the second run serves only to check the results. In case of EVA foil, a different behavior in the second run against the first one was observed. Consequently, we added third run for better understanding what is going on. This phenomenon was not observed in PVB test, so the third run of measurements was not necessary. Scenario for PVB polymer ply is summarized in table 4.2.

DAY 0:	Sample PVB was glued to rheometer
DAY 1:	1^{st}run: Measurement of sample loaded by temperature set $\mathcal{T}$ and harmonic strains with frequencies $\mathcal{F}$
DAY 2:	2^{nd}run: Measurement of sample loaded by temperature set $\mathcal{T}$ and harmonic strains with frequencies $\overline{\mathcal{F}}$

TABLE 4.2: Measurement scenario for PVB foil

4.2 Results

Property	Value
Specimen label	EVA07
Radius R_s	10 mm
Height h_s	10.327 mm
Height of glasses t_g	9.6 mm
Foil height $h_f = h_s - t_g$	0.727 mm

TABLE 4.3: EVA07 parameters

Property	Value
Specimen label	PVB03
Radius R_s	10 mm
Height h_s	10.356 mm
Height of glasses t_g	9.6 mm
Foil height $h_f = h_s - t_g$	0.756 mm

TABLE 4.4: PVB03 parameters

Experiments were performed on several cylindrical specimens with EVA and PVB foil. In this section, we introduce the results for one specimen with EVA and one PVB sample.

Dimensions of these specimens are arranged in tables 4.3 and 4.4. The specimen label uniquely identifies the sample. R_s and h_s are the radius and total height of the cylinder. The height is measured by the rheometer device, so it is exactly the distance between the bottom plate and the movable adapter. Height of glasses t_g is sum of the thicknesses of both solid glass layers. This value was obtained after experiments, when the polymer interlayer was removed. From thicknesses h_s and t_g the height of foil as $h_f = h_s - t_g$ is calculated. We observed that the real thickness of foil is not exactly 0.75 mm but it is relatively close. Parameters in tables directly serves for the calculation of transformation coefficient $P(R_a, R_s, h_s, h_f)$ from equation (3.9). The last unknown parameter is the radius of adapter R_a which is given by the adapter geometry and in our case is $R_a = 25$ mm. After the experiment and transformation via equation (3.9) was done we obtained the values of storage and loss moduli for EVA07 and PVB03 sample. The results are illustrated in Figures 4.2 and 4.1.

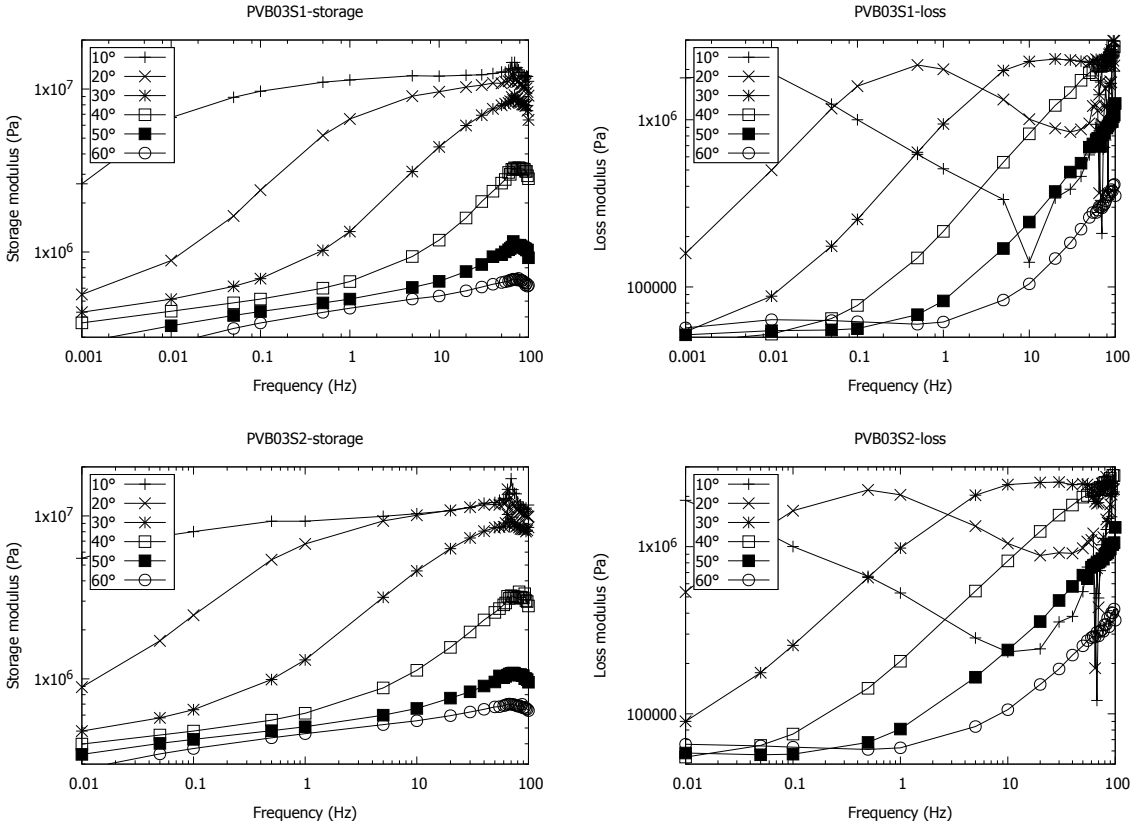

FIGURE 4.1: Storage and loss moduli of PVB03 sample in dependence on frequency for two consecutive runs

Individual graphs are arranged in the figures as follows. Left and right column represent the storage, respectively the loss modulus and individual rows are tied to one of the consecutive runs. For EVA foil, there are three rows for three runs and for PVB foil two runs are presented only. Each graph illustrate dependence of moduli on frequency in logarithm scale. We measured data for frequency up to 100 Hz, although in our set $\mathcal{F}$ assumed the maximum of 50Hz. From the plotted results it is evident that frequencies 50-100 Hz are very volatile. This unreliable domain is always excluded from our analysis.

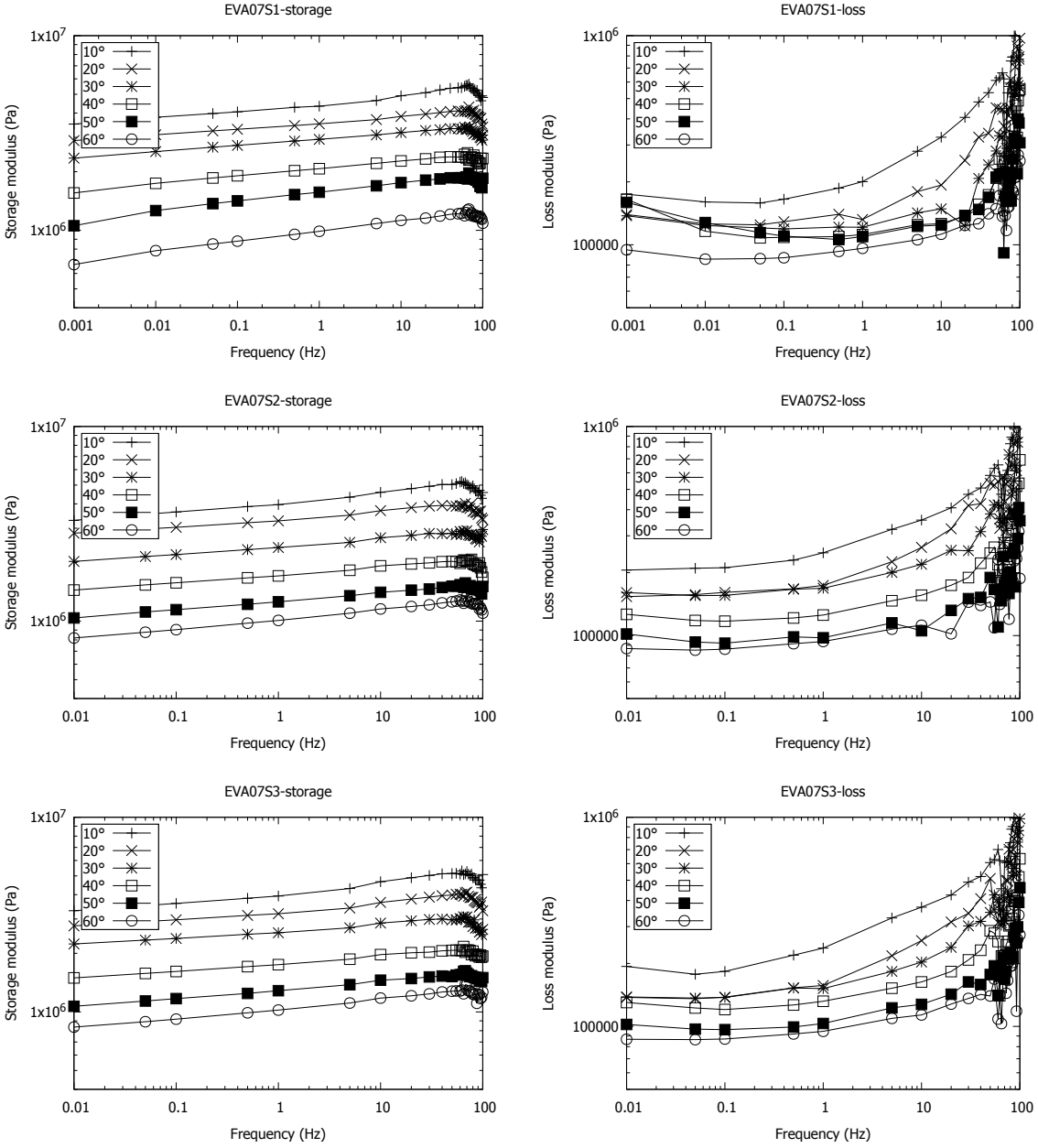

FIGURE 4.2: Storage and loss moduli of EVA07 sample in dependence on frequency for three consecutive runs

The difference between the two types of polymers is evident from the graphs. For lower temperatures, say 10°C, 20°C and 30°C, the PVB foil has a higher stiffness than the EVA foil, while for other temperatures the trend is opposite. The PVB foil has a rapid decline with increasing temperature, whereas EVA is relatively stable in the temperature domain. The same behavior is observed for the loss moduli. It is also interesting that for the EVA foil the loss and the storage modulus differs by orders. In case of PVB, the curves are closer and the values are roughly of the same order. Graphs also show two strangeness in polymers behavior. First oddity can be obvious from the loss modulus plot labeled as *EVA07-S1-loss* in Figure 4.2. The curves for temperatures 10°C, 20°C, 30°C and 60°C looks alright, but the remaining curves overlap the others and have unlikely shape. This phenomenon occurred on several specimens but the cause is unknown.

The loss modulus for the EVA foil has lower values, so the cause can be the device inaccuracies. Second discrepancy follows from the graphs for storage moduli in Figure 4.2. If we compare the graphs for different measurement runs we observe, that the curves for certain temperature differs quite significantly. For temperature 30°C it can be seen from Figure 4.3. Figure 4.4 is the same comparison for temperature 60°C, where the

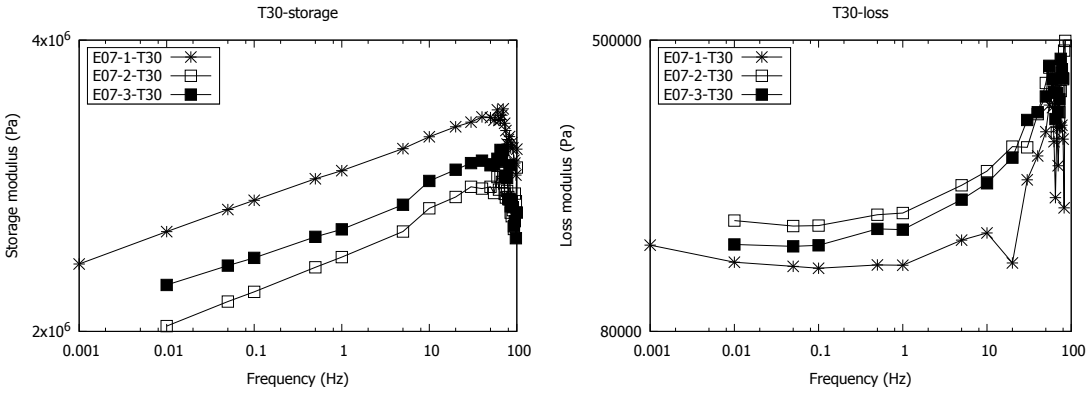

(A) Storage modulus (B) Loss modulus

FIGURE 4.3: Curves for EVA07 sample for temperature 30°C over three consecutive runs

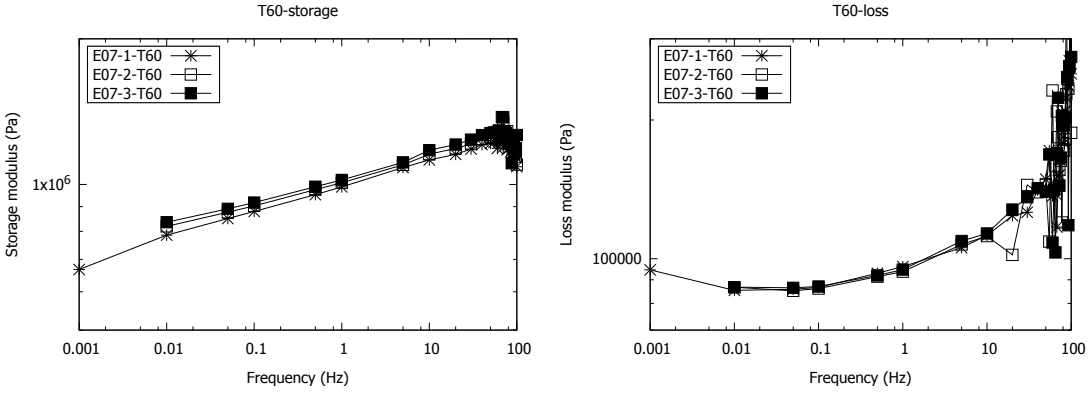

(A) Storage modulus (B) Loss modulus

FIGURE 4.4: Curves for EVA07 sample for temperature 60°C over three consecutive runs

curves have not this strange behavior. The difference in stiffness in the first and the following measurement runs was not observed on PVB samples. It is not so obvious from graph 4.3a, but the results from the third run often lie close to curve from the second run, but always there was some shifting down (softening) after the first measurement day. This softening was observed over all temperatures with exception of 60°C. It can be caused by tempering or by mechanical loading. Either way there is some type of long term hysteresis. In other words, the EVA foil is not only time and temperature depend, but also load-history depend. This behavior has not been sufficiently explained yet and research is still ongoing.

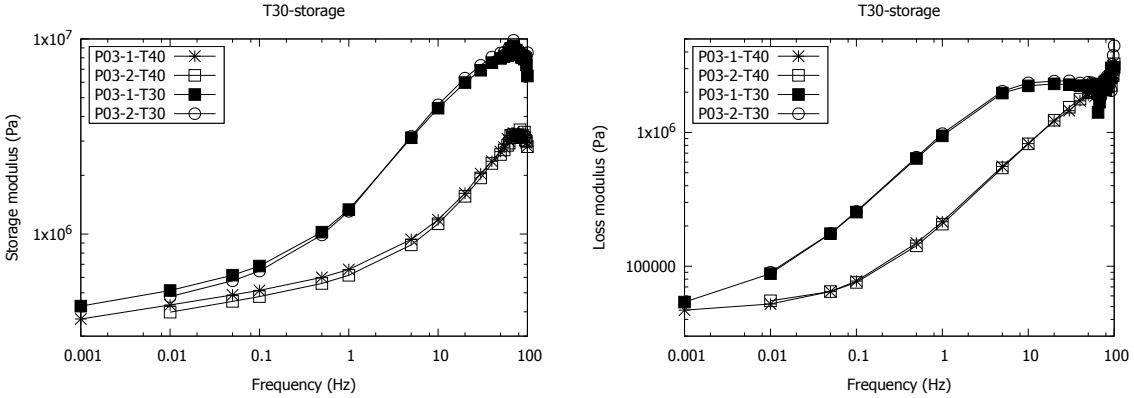

FIGURE 4.5: Curves for PVB03 sample for temperature 30°C and 40°C over three consecutive runs

4.3 Calibration

In the previous chapter, we have introduced the calibration procedure theoretically and now it will be applied to our measured data. We have two goals. Primarily, we want to obtain free parameters of the generalized Maxwell model and the shift factor parameters of the WLF equation and secondary we want to extract the master curve (which is basically the same task). Firstly, we must define a region of interest by choosing the number of Maxwell cells and values of relaxation times τ_i. Sufficient compromise is one relaxation time (one Maxwell unit) for one decade, thus set $\tau_{i,E}$ for the EVA foil is selected as

$$\tau_{i,E} = 10^i, i = \{-3, -2, \ldots, 6, 7\}, n = 11,$$

and for the PVB foil the set $\tau_{i,P}$ is

$$\tau_{i,P} = 10^i, i = \{-3, -2, \ldots, 9, 10\}, n = 14.$$

After running the calibration process we obtain value of free parameters G_i, G_∞, C_1 and C_2, which fully describe our material model. For specimens EVA07 the values are summarized in table 4.5, where only the first run (S1) was considered. For sample PVB03 (all runs, S1 and S2) results are listed in table 4.6.

Parameter	Value	Parameter	Value
G_1	984825.3 Pa	G_{10}	158709.4 Pa
G_2	213045.1 Pa	G_{11}	363715.6 Pa
G_3	302524.2 Pa	G_{12}	107063.5 Pa
G_4	301446.8 Pa	G_{13}	169494.8 Pa
G_5	187313.9 Pa	G_{14}	229645.9 Pa
G_6	486441.7 Pa	G_∞	752332.8 Pa
G_7	159285.0 Pa	C_1	335.98
G_8	296281.9 Pa	C_2	1340.58 °C
G_9	288590.1 Pa		

TABLE 4.5: Parameters of generalized Maxwell chain and WLF equation for EVA07 mastercurve

Parameter	Value	Parameter	Value
G_1	946751.8 Pa	G_8	77670.3 Pa
G_2	1384505.4 Pa	G_9	84159.5 Pa
G_3	3963454.0 Pa	G_{10}	94135.1 Pa
G_4	4088688.3 Pa	G_{11}	92988.0 Pa
G_5	581477.5 Pa	G_∞	113026.4 Pa
G_6	242174.8 Pa	C_1	18.33
G_7	78461.4 Pa	C_2	121.58 °C

TABLE 4.6: Parameters of generalized Maxwell chain and WLF equation for PVB03 mastercurve

Correctness of the calibration process is best seen on the master curve, which is constructed based on the optimal parameters C_1 and C_2. The resulting graphs for the EVA foil are shown in Figure 4.6 and for the PVB foil in Figure 4.7, where the experimental data are plotted with crosses and the theoretical master curve given by the Maxwell model and the WLF equation is plotted by the solid line.

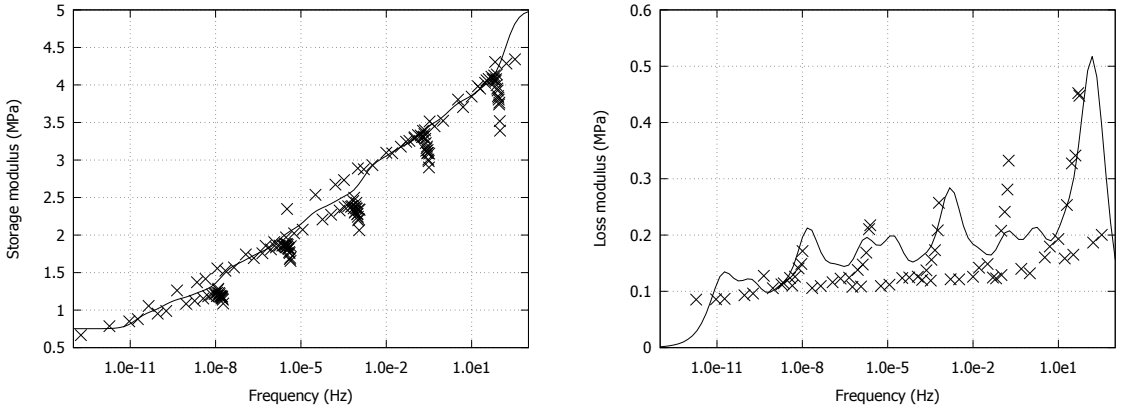

FIGURE 4.6: Mastercurve of storage modulus for specimen with EVA foil for experimental data and curve of mathematical estimation

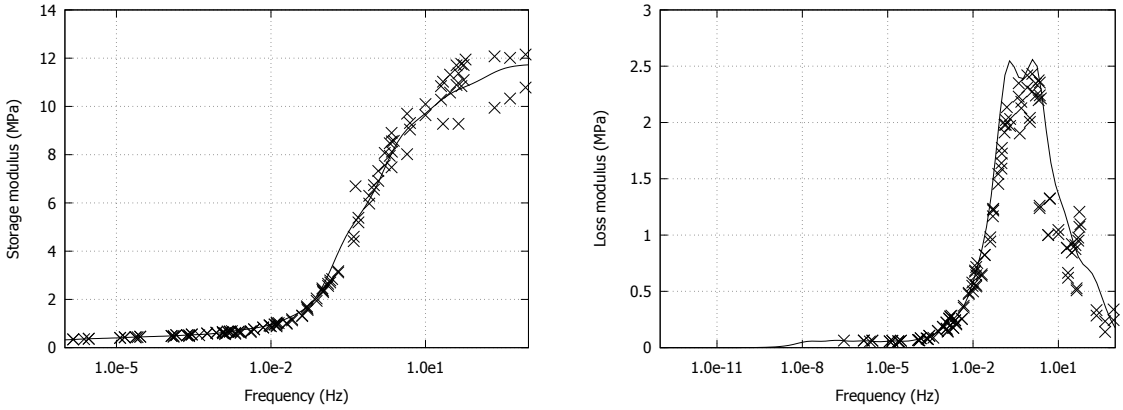

FIGURE 4.7: Mastercurve of storage modulus for specimen with PVB foil for experimental data and curve of mathematical estimation

It is obvious from the graphs of storage moduli (on the left) that the calibration process and the resulting model curve fit the experimental data very well. As for the loss moduli situation is more complicated. For the PVB foil there it is very sufficient estimation of loss mastercurve, but for EVA foil is not. It was discussed before, that the measurement of the loss moduli of the EVA foil has a high inaccuracy and this inaccurate confirmed here. Also the shape of each temperature curve of the experimental data suggests poor calibration ability. However, for now, there is no alternative than to use these parameters for further analysis.

Calibration analysis for the EVA foil is done for the first run (S1) only, because the EVA specimens exhibits some type of hysteresis discussed above. This phenomenon can be seen in graph 4.8, where all measurement runs are plotted. It is obvious, that one mastercurve can not include this discrepancy in the measured data since it is not described by our WLF-Maxwell model. This behavior needs further investigation.

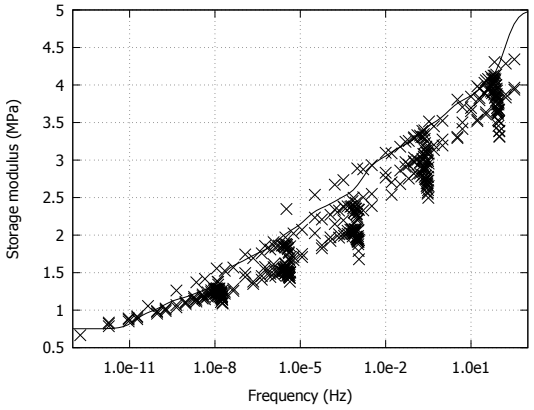

FIGURE 4.8: Mastercurve of EVA foil for all measurement runs.

Chapter 5

Finite element for laminated glass

In previous parts of the thesis, we discussed the experiment for laminated glass interlayer and calibration process for the determination of viscoelastic model parameters. In second part of the thesis, we focus on the laminated glass at a structural level. Our goal is to perform finite element analysis to examine natural vibration of laminated glass beams such that the result match the macroscopic experiments. Till the end, a three layer element will be formulated. The polymer interlayer is loaded predominantly in shear, so we need to consider the Mindlin hypothesis, which anticipates planar cross-section not necessarily perpendicular to the center line. Although deriving the Mindlin element for FEM is a common task and can be found in most FEM books, its derivation is presented here to show specifics of the adopted multilayer theory. For more details we recommended for example [18] or [19].

5.1 Mindlin beam ODE

FEM is one of the numerical method for solving differential equations. General description of beams is very complicated nonlinear problem, but if we accept several simplifying assumptions, we get linear differential equations for deformation of the beam centerline. Final equation arises from three basic types of equation sets. We consecutively introduce these sets with the used assumptions. In general, position coordinates are restricted by beam domain $\mathcal{B} \subset \mathbb{R}^3$ and time domain is set by interval $\mathcal{T} = \langle 0, T \rangle \subset \mathbb{R}$. Every four-coordinate vector is picked from this domain $\mathcal{B} \times \mathcal{T}$.

Equilibrium conditions

First, we investigate conditions of equilibrium and get relation between internal forces. If we limit our attention to small deflections only, we can assembly these conditions on undeformed beam (first order analysis) with relatively good accuracy. With this assumption, we can imagine infinitesimal element cut out of the beam. Forces acting on this element are illustrated in Figure 5.1. Because we analyze natural vibrations, no external forces are considered. Black dot represents a concentrated mass of the beam

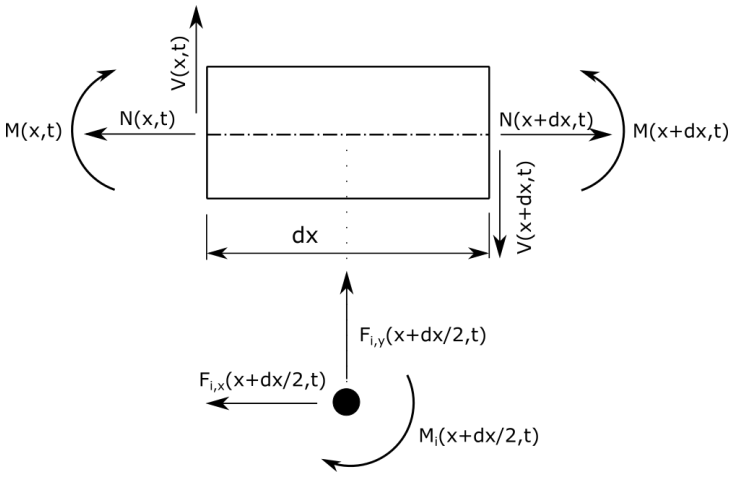

FIGURE 5.1: Reactions on infinitesimal small piece of beam without external forces

element. Inertia forces and angular momentum from this mass are

$$F_{i,x}(x+dx/2,t) = \rho(x+dx/2)A(x+dx/2)\ddot{u}(x+dx/2,t)dx, \tag{5.1}$$
$$F_{i,z}(x+dx/2,t) = \rho(x+dx/2)A(x+dx/2)\ddot{w}(x+dx/2,t)dx, \tag{5.2}$$
$$M_i(x+dx/2,t) = \rho(x+dx/2)I_y(x+dx/2)\ddot{\varphi}_y(x+dx/2,t)dx, \tag{5.3}$$

where we consider that area $A(x,t) = A(x)$, moment of inertia $I_y(x,t) = I_y(x)$ and density $\rho(x,t) = \rho(x)$ are not function of time. It can be shown that placement of concentrated mass in the x-direction is irrelevant for inertia forces, so we can replace point $(x+dx/2,t)$ by only (x,t) for clarity. Now, we can assembly equilibrium conditions in two directions (x and z) and the momentum condition around the center of gravity of the beam element. We obtain

$$\begin{aligned}
\rightarrow &: \quad N(x+dx,t) - N(x,t) - \rho(x)A(x)\ddot{u}(x,t)dx = 0,\\
\downarrow &: \quad V(x+dx,t) - V(x,t) - \rho(x)A(x)\ddot{w}(x,t)dx = 0,\\
\curvearrowleft &: \quad M(x+dx,t) - M(x,t) - \tfrac{1}{2}V(x,t)dx - \tfrac{1}{2}V(x+dx,t)dx - \rho(x)I_y(x)\ddot{\varphi}_y(x,t)dx = 0.
\end{aligned} \tag{5.4}$$

We can expand the normal and shear force into the Taylor series and neglect members of quadratic and higher orders. For the general force $F(x,t)$ it holds

$$F(x+dx,t) \approx F(x,t) + \frac{\partial F(x,t)}{\partial x}dx + \mathcal{O}(dx^2). \tag{5.5}$$

Similarly we can extend moment of force around infinitesimally close point, where only the first member of Taylor series is linear. Therefore

$$F(x+dx,t)dx \approx F(x,t)dx + \mathcal{O}(dx^2). \tag{5.6}$$

If we substitute assumptions (5.5) and (5.6) into equilibrium conditions (5.4) and divide all equations by element size dx, we get the final relations between internal forces given by the following identities

$$\frac{\partial N}{\partial x}(x,t) - \rho(x)A(x)\ddot{u}(x,t) = 0, \tag{5.7}$$

$$\frac{\partial V}{\partial x}(x,t) - \rho(x)A(x)\ddot{w}(x,t) = 0, \tag{5.8}$$

$$\frac{\partial M}{\partial x}(x,t) - V(x,t) - \rho(x)I_y(x)\ddot{\varphi}_y(x,t) = 0. \tag{5.9}$$

Geometric equations

Before we apply geometric equations to our model, we must describe the displacement field. We consider that the beam is bent in the plane xz and is incompressible in z direction. Axis direction can be obvious from Figure 5.2. As stated, for simplicity of displacement field $u(x,z)$ we assume validity of the Mindlin beam hypothesis, which says

> *Cross-section that was planar before the deformation and perpendicular to centerline is planar also after deformation, but not necessarily perpendicular to center line.*

The Mindlin theory is schematically illustrated in Figure 5.2, where dots represent perpendicular cross section to the centerline, i.e. rotation of the cross section due to bending, and the solid line represents the cross section with influence of shear. If we denote rotation φ_y we can described the displacement field as

$$u(x,z,t) = u_0(x,t) + u_\varphi(x,z,t) = u_0(x,t) + \varphi_y(x,t)z, \tag{5.10}$$

where $u_0(x,t)$ is the normal stretch of the center line and $u_\varphi(x,z,t)$ is the horizontal displacement caused by the cross section rotation, see Figure 5.2. Moreover, we assume small deformation theory. Thus, we assume that projection of element length into x-axis is preserved (not real length of element) and also we assume validity of $\varphi_y \approx \tan\varphi_y$. This assumptions are reflected in identity (5.10) and also imply the following geometric equations

$$\varepsilon_x(x,z,t) = \frac{\partial u(x,z,t)}{\partial x} = \frac{\partial u_0(x,t)}{\partial x} + \frac{\partial \varphi_y(x,t)}{\partial x}z = \varepsilon_0(x,t) + \kappa_y(x,t)z, \tag{5.11}$$

$$\gamma_{zx}(x,t) = \frac{\partial w(x,t)}{\partial x} + \frac{\partial u(x,z,t)}{\partial z} = \frac{\partial w(x,t)}{\partial x} + \varphi_y(x,t), \tag{5.12}$$

where $\varepsilon_0(x,t)$ is the strain of the centerline and $\kappa_y(x,t)$ is curvature.

Physical equations

For relation between strain and stress we employ general Hook's law. This is sufficient for solid glass layer, but for viscous interlayer this model is inappropriate.[1] In addition, we assume that material moduli $E(x,y,z,t) = E$ and $G(x,y,z,t) = G$ are constant in space and time, so Hooke's laws states

$$\sigma_x(x,z,t) = E\varepsilon_x(x,z,t), \tag{5.13}$$

$$\tau_{xz}(x,t) = k(x)G\gamma_{zx}(x,t), \tag{5.14}$$

[1] However, transition to viscoelastic Mindlin beam is very straightforward. The natural vibration problem is solved in the domain of complex numbers $\mathbb{C}$ instead of $\mathbb{R}$.

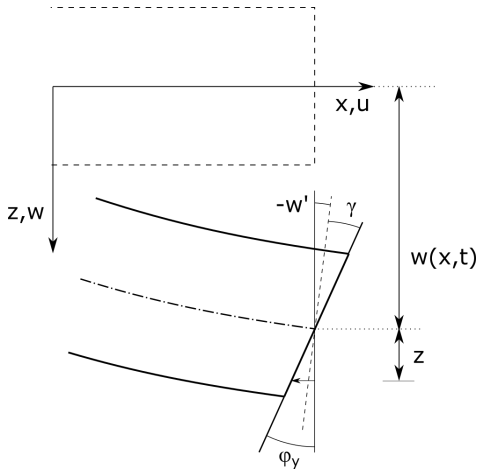

FIGURE 5.2: Deflection of Mindlin beam

where $k(x)$ is the shear coefficient which takes into account the difference between real shear stress and shear stress on Mindlin beam, where it is constant across the height. Parameter value $k(x)$ is derived from equality of mentioned stresses. It comes out

$$k(x) = \frac{I_y^2(x)}{A(x)\int_{A(x)} \frac{\overline{S}_y^2(z,x)}{b^2(z,x)} dA(x)}, \tag{5.15}$$

and for a rectangular cross section is $k = 5/6$. With identities (5.11) and (5.12) physical equations become

$$\sigma_x(x,z,t) = E\left(\varepsilon_0(x,t) + \kappa_y(x,t)z\right), \tag{5.16}$$

$$\tau_{xz}(x,t) = k(x)G\left(\frac{\partial w(x,t)}{\partial x} + \varphi_y(x,t)\right). \tag{5.17}$$

ODE for Mindlin beam

We can obtain internal forces by integrating corresponding stress components over the cross-section. From definition of internal forces it follows

$$N(x,t) = \int_{A(x)} \sigma_x(x,z,t) dA(x), \tag{5.18}$$

$$V(x,t) = \int_{A(x)} \tau_{xz}(x,t) dA(x) = \int_{A(x)} k(x) G\gamma_{xz}(x,t) dA(x) = \int_{A^*(x)} G\gamma_{xz}(x,t) dA^*(x), \tag{5.19}$$

$$M(x,t) = \int_{A(x)} z\sigma_x(x,z,t) dA(x), \tag{5.20}$$

where the reduced area $A^*(x)$ is defined as

$$A^*(x) := k(x)A(x). \tag{5.21}$$

Next, we express internal forces in dependence on the centerline displacements as

$$N(x,t) = E\int_{A(x)} \left(\frac{\partial u_0(x,t)}{\partial x} + \frac{\partial \varphi_y(x,t)}{\partial x} z\right) dA(x) = EA(x)\frac{\partial u(x,t)}{\partial x}, \tag{5.22}$$

$$V(x,t) = G\int_{A^*(x)} \left(\frac{\partial w(x,t)}{\partial x} + \varphi_y(x,t)\right) dA^*(x) = GA^*(x)\left(\varphi_y(x,t) + \frac{\partial w}{\partial x}(x,t)\right), \tag{5.23}$$

$$M(x,t) = E\int_{A(x)} \left(\frac{\partial u_0(x,t)}{\partial x} z + \frac{\partial \varphi_y(x,t)}{\partial x} z^2\right) dA(x) = EI_y(x)\frac{\partial \varphi_y(x,t)}{\partial x}. \tag{5.24}$$

Finally, we assembly the differential equations from the above identities. In particular we substitute relations (5.18)-(5.20) to equations (5.7)-(5.9) and we get the description of the Mindlin beam via these linear differential equations

$$\boxed{\begin{aligned} \frac{\partial}{\partial x}\left(EA(x)\frac{\partial u_0}{\partial x}(x,t)\right) - \rho(x)A(x)\ddot{u_0}(x,t) = 0, & \quad (5.25)\\ \frac{\partial}{\partial x}\left(GA^*(x)\left(\varphi_y(x,t) + \frac{\partial w}{\partial x}(x,t)\right)\right) - \rho(x)A(x)\ddot{w}(x,t) = 0, & \quad (5.26)\\ \frac{\partial}{\partial x}\left(EI_y(x)\frac{\partial \varphi_y}{\partial x}(x,t)\right) - GA^*(x)\left(\varphi_y + \frac{\partial w}{\partial x}(x,t)\right) - \rho(x)I_y(x)\ddot{\varphi}_y(x,t) = 0. & \quad (5.27) \end{aligned}}$$

Solution of these equations depends on the prescribed boundary conditions. So we need to specify them. First, we denote curve representing centerline as abstract $\Omega \subset \mathbb{R}$ and than boundary of this region by $\Gamma = \partial\Omega$. Boundaries are the same for all three unknown functions $u_0(x,t)$, $w(x,t)$, $\varphi(x,t)$, but we must decompose the boundary to two disjointed sets, where Γ_u is the boundary with the prescribed values of unknowns functions and Γ_f is the boundary with prescribed forces and $\Gamma_u \cup \Gamma_f = \Gamma$ and $\Gamma_u \cap \Gamma_f = \emptyset$. This decomposition is different for displacements u_0, w, φ_y, Formally written as

$$\Gamma^u = \Gamma^u_u + \Gamma^u_f, \tag{5.28}$$

$$\Gamma^w = \Gamma^w_u + \Gamma^w_f, \tag{5.29}$$

$$\Gamma^\varphi = \Gamma^\varphi_u + \Gamma^\varphi_f. \tag{5.30}$$

In natural vibration analysis, we consider no external forces, so roughly speaking we can neglect boundary conditions on Γ_f (In fact, forces act on boundary Γ_f, but are equal to zero and corresponding members vanish). Only kinematic conditions remain

$$\boxed{\begin{aligned} u_0(x) = \overline{u}_0, \forall x \in \Gamma_u, & \quad (5.31)\\ w(x) = \overline{w}, \forall x \in \Gamma_w, & \quad (5.32)\\ \varphi_y(x) = \overline{\varphi}_y(x), \forall x \in \Gamma_\varphi, & \quad (5.33) \end{aligned}}$$

where overlined quantities represented the prescribed values of individual functions. In the following text we reduce our general requirements and we put characteristics $A(x), I_y(x)$ and $\rho(x)$ independent of x.

5.2 Weak solution

Strong solution of (5.25)-(5.27) can not be found in closed form for most of the engineering tasks and we need to reduce our requirements. In particular, we do not require equations to be satisfied everywhere but only on average over the Ω, that means

$$\int_\Omega \delta u_0(x)\left(\frac{\partial}{\partial x}\left(EA\frac{\partial u_0}{\partial x}(x,t)\right) - \rho A\ddot{u_0}(x,t)\right) d\Omega = 0, \tag{5.34}$$

$$\int_\Omega \delta w(x) \left(\frac{\partial}{\partial x} \left(GA^* \left(\varphi_y(x,t) + \frac{\partial w}{\partial x}(x,t) \right) \right) - \rho A \ddot{w}(x,t) \right) d\Omega = 0, \tag{5.35}$$

$$\int_\Omega \delta \varphi_y(x) \left(\frac{\partial}{\partial x} \left(EI_y \frac{\partial \varphi_y}{\partial x}(x,t) \right) - GA^* \left(\varphi_y + \frac{\partial w}{\partial x}(x,t) \right) - \rho I_y \ddot{\varphi}_y(x,t) \right) d\Omega = 0, \tag{5.36}$$

where $\delta u_0(x)$, $\delta w(x)$, $\delta \varphi(x)$ are test weight functions. These are arbitrary but on boundary Γ_u we know exact solution, so the test functions must satisfy

$$\delta u_0(x) = 0, \forall x \in \Gamma_u^u, \tag{5.37}$$

$$\delta w(x) = 0, \forall x \in \Gamma_u^w, \tag{5.38}$$

$$\delta \varphi(x) = 0, \forall x \in \Gamma_u^\varphi. \tag{5.39}$$

Note that the second derivatives of unknown functions appear in the above integrals. The order of the derivatives can be reduced by generalized integration by parts (Gauss divergence theorem [11]), which states

$$\int_\Omega f(x) \frac{d}{dx} g(x) d\Omega = \int_\Gamma f(x) g(x) d\Gamma - \int_\Omega g(x) \frac{d}{dx} f(x) d\Omega. \tag{5.40}$$

The first term on the right hand side vanishes, because acting forces on Γ_f are equal to zero and the test function is zero on boundary Γ_u. However, $\Gamma = \Gamma_u + \Gamma_f$, so the member itself must be zero. This yields

$$\int_\Omega f(x) \frac{d}{dx} g(x) d\Omega = - \int_\Omega g(x) \frac{d}{dx} f(x) d\Omega. \tag{5.41}$$

Applying the Gauss theorem of above form to (5.34)-(5.36) gives

$$\int_\Omega \frac{d\delta u_0(x)}{dx} \left(EA \frac{\partial u_0}{\partial x}(x,t) \right) + \delta u_0(x) \rho A \ddot{u_0}(x,t) d\Omega = 0, \tag{5.42}$$

$$\int_\Omega \frac{d\delta w(x)}{dx} \left(GA^* \frac{\partial w}{\partial x}(x,t) \right) + \delta w(x) \frac{\partial}{\partial x} \left(GA^* \varphi_y(x,t) \right) + \delta w(x) \rho A \ddot{w}(x,t) d\Omega = 0, \tag{5.43}$$

$$\int_\Omega \frac{d\delta \varphi_y(x)}{dx} \left(EI_y \frac{\partial \varphi_y}{\partial x}(x,t) \right) + \delta \varphi_y(x) GA^* \left(\varphi_y + \frac{\partial w}{\partial x}(x,t) \right) + \delta \varphi_y(x) \rho I_y \ddot{\varphi}_y(x,t) d\Omega = 0. \tag{5.44}$$

This is the weak solution in the divergence form.

As a side note let us highlight the direct link between the weak formulation and the principle of virtual displacement. If we assume that test functions have the physical meaning of virtual displacement, then equation (5.42) can be written as

$$\int_V \delta \varepsilon \sigma_x dV + \int_V \delta u_0(x) X dV = 0, \tag{5.45}$$

where $\delta \varepsilon = \delta u_0'(x)$ is a virtual strain, $\sigma_x = E u_0'(x)$ is the normal stress and $X = \rho \ddot{u}_0$ is the inertia force of an infinitesimal element. But, this is energy equilibrium of principle of virtual displacement. Similar conclusion can be drawn for other equations. So if we assume equality of virtual displacements and test functions, then these principles are identical.

5.3 Discretization

It is convenient to split the domain Ω into small segments Ω^e, where $\bigcup_e \Omega^e = \Omega$ and $\bigcap_e \Omega^e = \emptyset$. We require the unknown function to solve the set of differential equation in the weak form. We approximate the unknown functions in terms of the shape functions and nodal values. If we denote the left node by lower index 1 and the right node by index 2, we can arrange the element nodal values into vectors

$$\boldsymbol{r}_u^e(t) = \{u_1^e(t), u_2^e(t)\}^\mathsf{T} \quad \delta\boldsymbol{r}_u^e(t) = \{\delta u_1^e(t), \delta u_2^e(t)\}^\mathsf{T}, \tag{5.46}$$

$$\boldsymbol{r}_w^e(t) = \{w_1^e(t), w_2^e(t)\}^\mathsf{T} \quad \delta\boldsymbol{r}_w^e(t) = \{\delta w_1^e(t), \delta w_2^e(t)\}^\mathsf{T}, \tag{5.47}$$

$$\boldsymbol{r}_\varphi^e(t) = \{\varphi_1^e(t), \varphi_2^e(t)\}^\mathsf{T} \quad \delta\boldsymbol{r}_\varphi^e(t) = \{\delta\varphi_1^e(t), \delta\varphi_2^e(t)\}^\mathsf{T}. \tag{5.48}$$

Now, we describe internal displacement field on element as a product of nodal values (5.46)-(5.48) and the matrix of shape (base) functions, which are independent of time. Next, we take the derivative of the displacement field with respect to x. Vectors (5.46)-(5.48) are space independent, so we differentiate only the base functions. The matrix of the element base functions is denoted $\mathbf{N}^e$ and its derivatives $\mathbf{B}^e$. The displacement approximation reads

$$\begin{array}{lll} u_0(x,t) \approx \mathbf{N}_u^e(x)\boldsymbol{r}_u^e(t) & w(x,t) \approx \mathbf{N}_w^e(x)\boldsymbol{r}_w^e(t) & \varphi_y(x,t) \approx \mathbf{N}_\varphi^e(x)\boldsymbol{r}_\varphi^e(t), \\ u_0(x,t) \approx \mathbf{B}_u^e(x)\boldsymbol{r}_u^e(t) & w(x,t) \approx \mathbf{B}_w^e(x)\boldsymbol{r}_w^e(t) & \varphi_y(x,t) \approx \mathbf{B}_\varphi^e(x)\boldsymbol{r}_\varphi^e(t). \end{array} \tag{5.49}$$

In FEM we assume that the virtual displacements (test functions) are interpolated by the the same base functions, so we get

$$\begin{array}{lll} \delta u_0(x,t) \approx \mathbf{N}_u^e(x)\delta\boldsymbol{r}_u^e(t) & \delta w(x,t) \approx \mathbf{N}_w^e(x)\delta\boldsymbol{r}_w^e(t) & \delta\varphi_y(x,t) \approx \mathbf{N}_\varphi^e(x)\delta\boldsymbol{r}_\varphi^e(t), \\ \delta u_0(x,t) \approx \mathbf{B}_u^e(x)\delta\boldsymbol{r}_u^e(t) & \delta w(x,t) \approx \mathbf{B}_w^e(x)\delta\boldsymbol{r}_w^e(t) & \delta\varphi_y(x,t) \approx \mathbf{B}_\varphi^e(x)\delta\boldsymbol{r}_\varphi^e(t). \end{array} \tag{5.50}$$

In what follows we omit x and t dependencies in brackets and use the following abbreviated notation

$$\mathbf{N}^e\boldsymbol{r}^e \equiv \mathbf{N}^e(x)\boldsymbol{r}^e(t), \quad \mathbf{B}^e\boldsymbol{r}^e \equiv \mathbf{B}^e(x)\boldsymbol{r}^e(t). \tag{5.51}$$

Now we can substitute this discrete system (5.49)-(5.50) to a divergence form of the weak solution (5.42)-(5.44) and we immediately get

$$\int_{\Omega^e} (\mathbf{B}_u^e\delta\boldsymbol{r}_u^e)^\mathsf{T} EA\mathbf{B}_u^e\boldsymbol{r}_u^e + (\mathbf{N}_u^e\delta\boldsymbol{r}_u^e)^\mathsf{T}\rho A\mathbf{N}_u^e\ddot{\boldsymbol{r}}_u^e d\Omega^e = 0, \tag{5.52}$$

$$\int_{\Omega^e} (\mathbf{B}_w^e\delta\boldsymbol{r}_w^e)^\mathsf{T} GA^* \left(\mathbf{N}_\varphi^e\boldsymbol{r}_\varphi^e + \mathbf{B}_w^e\boldsymbol{r}_w^e\right) + (\mathbf{N}_w^e\delta\boldsymbol{r}_w^e)^\mathsf{T}\rho A\mathbf{N}_w^e\ddot{\boldsymbol{r}}_w^e d\Omega^e = 0, \tag{5.53}$$

$$\int_{\Omega^e} (\mathbf{B}_\varphi^e\delta\boldsymbol{r}_\varphi^e)^\mathsf{T} EI_y\mathbf{B}_\varphi^e\boldsymbol{r}_\varphi^e + \left(\mathbf{N}_\varphi^e\delta\boldsymbol{r}_{\boldsymbol{\varphi}}^{\boldsymbol{e}}\right)^\mathsf{T} GA^* \left(\mathbf{N}_\varphi^e\boldsymbol{r}_\varphi^e + \mathbf{B}_w^e\boldsymbol{r}_w^e\right) + (\mathbf{N}_\varphi^e\delta\boldsymbol{r}_\varphi^e)^\mathsf{T}\rho I_y\mathbf{N}_\varphi^e\ddot{\boldsymbol{r}}_\varphi^e d\Omega^e = 0. \tag{5.54}$$

If we define element stiffness matrices

$$\mathbf{K}_u^e := \int_{\Omega^e} (\mathbf{B}_u^e)^\mathsf{T} EA \mathbf{B}_u^e d\Omega^e, \tag{5.55}$$

$$\mathbf{K}_w^e := \int_{\Omega^e} (\mathbf{B}_w^e)^\mathsf{T} GA^* \mathbf{B}_w^e d\Omega^e, \tag{5.56}$$

$$\mathbf{K}_\varphi^e := \int_{\Omega^e} \left(\mathbf{B}_\varphi^e\right)^\mathsf{T} EI_y \mathbf{B}_\varphi^e d\Omega^e + \int_{\Omega^e} \left(\mathbf{N}_\varphi^e\right)^\mathsf{T} GA^* \mathbf{N}_\varphi^e d\Omega^e, \tag{5.57}$$

$$\mathbf{K}_{w\varphi}^e := \int_{\Omega^e} (\mathbf{B}_w^e)^\mathsf{T} GA^* \mathbf{N}_\varphi^e d\Omega^e, \tag{5.58}$$

$$\mathbf{K}_{\varphi w}^e := \int_{\Omega^e} \left(\mathbf{N}_\varphi^e\right)^\mathsf{T} GA^* \mathbf{B}_w^e d\Omega^e \tag{5.59}$$

and mass element matrices

$$\mathbf{M}_u^e := \int_{\Omega^e} (\mathbf{N}_u^e)^\mathsf{T} \rho A \mathbf{N}_u^e d\Omega^e, \tag{5.60}$$

$$\mathbf{M}_w^e := \int_{\Omega^e} (\mathbf{N}_w^e)^\mathsf{T} \rho A \mathbf{N}_w^e d\Omega^e, \tag{5.61}$$

$$\mathbf{M}_\varphi^e := \int_{\Omega^e} \left(\mathbf{N}_\varphi^e\right)^\mathsf{T} \rho I_y \mathbf{N}_\varphi^e d\Omega^e, \tag{5.62}$$

we arrive at the set of discrete equations written in the compact form

$$(\delta \boldsymbol{r}_u^e)^\mathsf{T} (\mathbf{K}_u^e \boldsymbol{r}_u^e + \mathbf{M}_u^e \ddot{\boldsymbol{r}}_u^e) = \mathbf{0}, \tag{5.63}$$

$$(\delta \boldsymbol{r}_w^e)^\mathsf{T} \left(\mathbf{K}_w^e \boldsymbol{r}_w^e + \mathbf{K}_{w\varphi}^e \boldsymbol{r}_\varphi^e + \mathbf{M}_w^e \ddot{\boldsymbol{r}}_w^e\right) = \mathbf{0}, \tag{5.64}$$

$$(\delta \boldsymbol{r}_\varphi^e)^\mathsf{T} \left(\mathbf{K}_\varphi^e \boldsymbol{r}_\varphi^e + \mathbf{K}_{\varphi w}^e \boldsymbol{r}_w^e + \mathbf{M}_\varphi^e \ddot{\boldsymbol{r}}_\varphi^e\right) = \mathbf{0}. \tag{5.65}$$

Since the leftmost term of each above equation contains arbitrary functions, the equation is fulfilled when the second bracket is equal to zero. Furthermore the equations can be written as one

$$\mathbf{K}^e \boldsymbol{r}^e + \mathbf{M}^e \ddot{\boldsymbol{r}}^e = \mathbf{0}, \tag{5.66}$$

where $\mathbf{K}^e$ is the element stiffness matrix and $\mathbf{M}^e$ is the element mass matrix and $\boldsymbol{r}^e$ is the vector of generalized nodal displacements

$$\mathbf{K}^e = \begin{pmatrix} \mathbf{K}_u^e & \mathbf{0} & \mathbf{0} \\ \mathbf{0} & \mathbf{K}_w^e & \mathbf{K}_{w\varphi}^e \\ \mathbf{0} & \mathbf{K}_{\varphi w}^e & \mathbf{K}_\varphi^e \end{pmatrix} \quad \mathbf{M}^e = \begin{pmatrix} \mathbf{M}_u^e & \mathbf{0} & \mathbf{0} \\ \mathbf{0} & \mathbf{M}_w^e & \mathbf{0} \\ \mathbf{0} & \mathbf{0} & \mathbf{M}_\varphi^e \end{pmatrix}, \tag{5.67}$$

$$\boldsymbol{r}^e = \{\boldsymbol{r}_u^e, \boldsymbol{r}_w^e, \boldsymbol{r}_\varphi^e\}^\mathsf{T}. \tag{5.68}$$

Because (5.66) must be satisfied on every element and neighboring elements share the nodal displacement we must satisfy the following global system of equations

$$\mathbf{K}\boldsymbol{r} + \mathbf{M}\ddot{\boldsymbol{r}} = \mathbf{0}, \tag{5.69}$$

where $\mathbf{K}$ and $\mathbf{M}$ are the global stiffness and mass matrices. The process of assembling $\mathbf{K}$ and $\mathbf{M}$ from each element is called localization [19] and it is formally denoted as

$$\mathbf{K} = \mathrm{Loc}\langle \mathbf{K}^e \rangle_e \quad \mathbf{M} = \mathrm{Loc}\langle \mathbf{M}^e \rangle_e. \tag{5.70}$$

5.4 Linear approximation and discussion

Now we have a general description for the local stiffness and mass matrices, but its actual form depends on the chosen base functions. We use linear shape functions. It turns out that for beams this simplest approximation is sufficient. First, we define an element domain Ω^e and its boundary Γ^e as

$$\Omega^e := x, x \in < 0, L^e > \quad \Gamma^e = \{0, L^e\}, \tag{5.71}$$

where L^e is the length of the beam element centerline and x is the local x-axis. We use the same base functions for the displacement and rotation fields (real and virtual). For the element domain we get the shape functions

$$\mathbf{N}_u^e = \mathbf{N}_w^e = \mathbf{N}_\varphi^e = \left(1 - \frac{x}{L^e}, \frac{x}{L^e}\right), \tag{5.72}$$

and their derivatives

$$\mathbf{B}_u^e = \mathbf{B}_w^e = \mathbf{B}_\varphi^e = \left(-\frac{1}{L^e}, \frac{1}{L^e}\right). \tag{5.73}$$

This linear approximation is the simplest one, but if we use it for displacements as well as for rotations, we get the following contradiction. Consider the case of pure bending without a shear force. For this case the shear strain defined by (5.12) has to be zero on the entire element domain. Then, applying the linear approximation for $w(x)$ and $\varphi(x)$ leads to

$$\gamma_{zx}(x) = \frac{dw(x)}{dx} + \varphi_y(x) \approx \frac{1}{L^e}(w_2 - w_1) + \varphi_1 + \frac{x}{L^e}(\varphi_2 - \varphi_1) = 0. \tag{5.74}$$

This is satisfied only for

$$\varphi_2 - \varphi_1 = 0, \tag{5.75}$$

which on the other hand implies zero curvature defined as

$$\kappa = \frac{\partial \varphi(x)}{\partial x} \approx \frac{1}{L^e}(\varphi_2 - \varphi_1). \tag{5.76}$$

Curvature κ is obviously not zero in pure bending case. It is clear that this linear approximation cannot describe the kinematics of this special case without further modification. This phenomenon is called shear locking. To reduce this effect we use selective integration approach, which assumes constant approximation of rotation φ_y in the shear strain term

$$\gamma_{zx}(x) \approx \frac{1}{L^e}(w_2 - w_1) + \frac{1}{2}(\varphi_2 + \varphi_2). \tag{5.77}$$

For obtaining the local stiffness and mass matrices we substitute the linear base functions into equations (5.55)-(5.59) derived in the previous section in matrix $\mathbf{K}_\varphi$. Note that in submatrix $\mathbf{K}_\varphi$ we perform *selective* integration, i.e. we consider the approximation (5.77).

We get the element stiffness matrix

$$\mathbf{K}^e = \begin{pmatrix} \frac{EA}{L^e} & 0 & 0 & -\frac{EA}{L^e} & 0 & 0 \\ 0 & \frac{GA^*}{L^e} & -\frac{GA^*}{2} & 0 & -\frac{GA^*}{L^e} & -\frac{GA^*}{2} \\ 0 & -\frac{GA^*}{2} & \frac{GA^*L^e}{4} + \frac{EI_y}{L^e} & 0 & \frac{GA^*}{2} & \frac{GA^*L^e}{4} - \frac{EI_y}{L^e} \\ -\frac{EA}{L^e} & 0 & 0 & \frac{EA}{L^e} & 0 & 0 \\ 0 & -\frac{GA^*}{L^e} & \frac{GA^*}{2} & 0 & \frac{GA^*}{L^e} & \frac{GA^*}{2} \\ 0 & -\frac{GA^*}{2} & \frac{GA^*L^e}{4} - \frac{EI_y}{L^e} & 0 & \frac{GA^*}{2} & \frac{GA^*L^e}{4} + \frac{EI_y}{L^e} \end{pmatrix}, \tag{5.78}$$

and the element mass matrix

$$\mathbf{M}^e = \begin{pmatrix} \frac{\rho AL^e}{3} & 0 & 0 & \frac{\rho AL^e}{6} & 0 & 0 \\ 0 & \frac{\rho AL^e}{3} & 0 & 0 & \frac{\rho AL^e}{6} & 0 \\ 0 & 0 & \frac{\rho AI_yL^e}{3} & 0 & 0 & \frac{\rho I_yL^e}{6} \\ \frac{\rho AL^e}{6} & 0 & 0 & \frac{\rho AL^e}{3} & 0 & 0 \\ 0 & \frac{\rho AL^e}{6} & 0 & 0 & \frac{\rho AL^e}{3} & 0 \\ 0 & 0 & \frac{\rho I_yL^e}{6} & 0 & 0 & \frac{\rho I_yL^e}{3} \end{pmatrix}, \tag{5.79}$$

where we assume that nodal displacements are arranged in the following order

$$\boldsymbol{r}^e = \{u_1, w_1, \varphi_1, u_2, w_2, \varphi_2\}^{\mathsf{T}}. \tag{5.80}$$

We described how to solve the set of differential equations by the finite element method in this section, but we used engineering variant of this approach. It is also good to emphasize its links to mathematical variant of this method. Ritz method [11] finds the solution of ODE in form

$$f(x) = \sum_{i=1}^{n} \alpha_i g_i(x), \tag{5.81}$$

where $g_i(x)$ are chosen continuous functions. The set of α_i is obtained by minimizing energy of the system. FEM is based on Ritz method, but functions $g_i(x)$ are chosen non zero only on small region. Example of two such functions is illustrated in Figure 5.3, where we can interpolate solution in interval $\langle 3, 4\rangle$ by linear combination by these two functions. In the context of the previous (engineering) approach, the function $g_i(x)$ for i-th node can be seen as the combination of the corresponding shape functions on the neighboring elements and assumed zero elsewhere, recall $f_1(x)$ from Figure 5.3 extended to domain $\langle 0, 10\rangle$. Consequently, values of constants α_i represent nodal displacements.

5.5 Multi-layer model

In the previous section we have formulated the Mindlin beam element with a homogeneous cross section. But laminated glass beams have the multilayered cross section. In this section we restrict our considerations to three-layered beams –two solid glass plate and one viscous interlayer– and formulate super element for this case. We start from

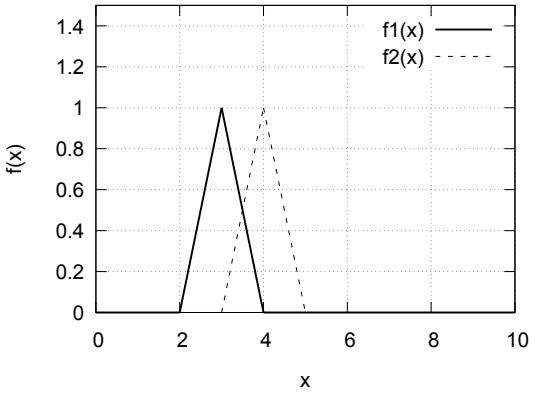

FIGURE 5.3: Example of two approximation functions in finite element approach

the Mindlin beam element for each layer and define additional constraints to enforce deformation continuity on the glass-polymer contact. One way is to use the Lagrange multipliers for assembling the constrained energy functional, where in the additional Lagrange multipliers have a physical meaning of the force between layers, see [20]. But in this case this method is unnecessarily complex and we add additional degrees of freedom to the system. Therefore we enforce the continuity between layers by kinematic conditions which are easily expressed for this case.

Let's index the generalized displacements of the left edge nodes by odd numbers and of right nodes by even numbers, see Figure 5.4a.

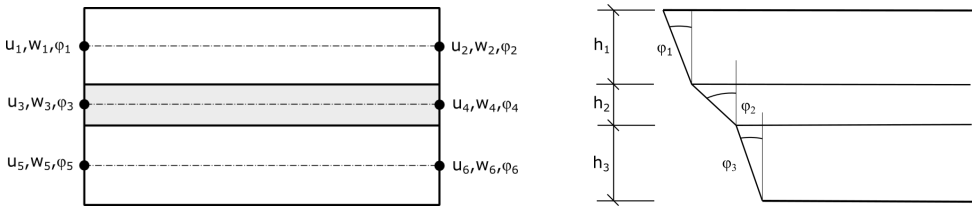

(A) (B)

FIGURE 5.4: Kinematics of layered multi-node beam

If we arrange the generalized nodal displacements into vector in the following order

$$\boldsymbol{r}^e = \{u_1, w_1, \varphi_1, u_2, w_2, \varphi_2, u_3, w_3, \varphi_3, u_4, w_4, \varphi_4, u_5, w_5, \varphi_5, u_6, w_6, \varphi_6\}^{\mathsf{T}}, \tag{5.82}$$

for simple unconstrained case we get the following stiffness and mass matrices

$$\mathbf{K}_s^e = \begin{pmatrix} \mathbf{K}_1^e & \mathbf{0} & \mathbf{0} \\ \mathbf{0} & \mathbf{K}_2^e & \mathbf{0} \\ \mathbf{0} & \mathbf{0} & \mathbf{K}_3^e \end{pmatrix}, \tag{5.83}$$

$$\mathbf{M}_s^e = \begin{pmatrix} \mathbf{M}_1^e & \mathbf{0} & \mathbf{0} \\ \mathbf{0} & \mathbf{M}_2^e & \mathbf{0} \\ \mathbf{0} & \mathbf{0} & \mathbf{M}_3^e \end{pmatrix}, \tag{5.84}$$

where $\mathbf{K}_i^e$ and $\mathbf{M}_i^e$ are matrices for the i-th layer. Assuming the layers are independent, we get the off diagonal terms equal to zero. To arrive of the constrained problem we

introduce restrictive conditions. For practical applications the sandwich beam is assumed incompressible in the transverse direction so relative vertical displacements of nodes in one cross section are negligible. Therefore we get the set of constraints

$$w_1 = w_3 = w_5, \tag{5.85}$$

$$w_2 = w_4 = w_6. \tag{5.86}$$

Next we need to enforce the continuity of horizontal displacements u_i at the interfaces. Such a situation is illustrated in Figure 5.4b, where the deformed face of the left end of the beam element is drawn. Kinematic constraints then read

$$\varphi_1 \frac{h_1}{2} + u_1 = -\varphi_3 \frac{h_2}{2} + u_3, \tag{5.87}$$

$$\varphi_3 \frac{h_2}{2} + u_3 = -\varphi_5 \frac{h_3}{2} + u_5, \tag{5.88}$$

$$\varphi_2 \frac{h_1}{2} + u_2 = -\varphi_4 \frac{h_2}{2} + u_4, \tag{5.89}$$

$$\varphi_4 \frac{h_2}{2} + u_4 = -\varphi_6 \frac{h_3}{2} + u_6. \tag{5.90}$$

Now we have 18 degree of freedom on one beam element and 8 restrictive conditions. It follows that only 10 degrees of freedom are independent. Several combinations are permissible but we choose the following master degrees of freedom

$$\boldsymbol{r}_m^e = \{u_1, w_1, \varphi_1, u_5, \varphi_5, u_2, w_2, \varphi_2, u_6, \varphi_6\}^{\mathsf{T}} \tag{5.91}$$

and the remaining (slaves degrees of freedom) are determined by constraints. Now we can construct the transformation matrix $\mathbf{T}$ which binds all degrees of freedom to master degrees of freedom via relation

$$\boldsymbol{r}^e = \mathbf{T}\boldsymbol{r}_m^e. \tag{5.92}$$

Now recall the equilibrium condition before the virtual displacements were eliminated

$$(\delta \boldsymbol{r}^e)^{\mathsf{T}} \mathbf{K} \boldsymbol{r}^e + (\delta \boldsymbol{r}^e)^{\mathsf{T}} \mathbf{M} \ddot{\boldsymbol{r}}^e = 0. \tag{5.93}$$

If we substitute (5.92) to (5.93) we get

$$(\delta \boldsymbol{r}_m^e)^{\mathsf{T}} \mathbf{T}^{\mathsf{T}} \mathbf{K} \mathbf{T} \boldsymbol{r}_m^e + (\delta \boldsymbol{r}_m^e)^{\mathsf{T}} \mathbf{T}^{\mathsf{T}} \mathbf{M} \mathbf{T} \ddot{\boldsymbol{r}}_m^e = 0. \tag{5.94}$$

We define the super element stiffness matrix as

$$\mathbf{K}_r^e = \mathbf{T}^{\mathsf{T}} \mathbf{K}_s^e \mathbf{T}, \tag{5.95}$$

and the super element mass matrix

$$\mathbf{M}_r^e = \mathbf{T}^{\mathsf{T}} \mathbf{M}_s^e \mathbf{T}, \tag{5.96}$$

where the transformation matrix $\mathbf{T}$ containing the restrictive conditions is given by [21]

$$\mathbf{T} = \begin{pmatrix}
1 & 0 & 0 & 0 & 0 & 0 & 0 & 0 & 0 & 0 \\
0 & 1 & 0 & 0 & 0 & 0 & 0 & 0 & 0 & 0 \\
0 & 0 & 1 & 0 & 0 & 0 & 0 & 0 & 0 & 0 \\
0 & 0 & 0 & 0 & 0 & 1 & 0 & 0 & 0 & 0 \\
0 & 0 & 0 & 0 & 0 & 0 & 1 & 0 & 0 & 0 \\
0 & 0 & 0 & 0 & 0 & 0 & 0 & 1 & 0 & 0 \\
\frac{1}{2} & 0 & \frac{h_1}{4} & \frac{1}{2} & -\frac{h_3}{4} & 0 & 0 & 0 & 0 & 0 \\
0 & 1 & 0 & 0 & 0 & 0 & 0 & 0 & 0 & 0 \\
-\frac{1}{h_2} & 0 & -\frac{h_1}{2h_2} & \frac{1}{h_2} & -\frac{h_3}{2h_2} & 0 & 0 & 0 & 0 & 0 \\
0 & 0 & 0 & 0 & 0 & \frac{1}{2} & 0 & \frac{h_1}{4} & \frac{1}{2} & -\frac{h_3}{4} \\
0 & 0 & 0 & 0 & 0 & 0 & 1 & 0 & 0 & 0 \\
0 & 0 & 0 & 0 & 0 & -\frac{1}{h_2} & 0 & -\frac{h_1}{2h_2} & \frac{1}{h_2} & -\frac{h_3}{2h_2} \\
0 & 0 & 0 & 1 & 0 & 0 & 0 & 0 & 0 & 0 \\
0 & 1 & 0 & 0 & 0 & 0 & 0 & 0 & 0 & 0 \\
0 & 0 & 0 & 0 & 1 & 0 & 0 & 0 & 0 & 0 \\
0 & 0 & 0 & 0 & 0 & 0 & 0 & 0 & 1 & 0 \\
0 & 0 & 0 & 0 & 0 & 0 & 1 & 0 & 0 & 0 \\
0 & 0 & 0 & 0 & 0 & 0 & 0 & 0 & 0 & 1
\end{pmatrix}. \tag{5.97}$$

The global stiffness and mass matrices are again obtained by the localization process

$$\mathbf{K}_r = \mathrm{Loc}\langle \mathbf{K}_r^e \rangle_e \quad \mathbf{M}_r = \mathrm{Loc}\langle \mathbf{M}_r^e \rangle_e. \tag{5.98}$$

5.6 Viscoelastic beam

The last step in the formulation of the finite beam element for the laminated glass is extension to viscoelasticity. We mentioned earlier that the transition to viscoelastic beam for modal analysis can be done by assuming complex modulus $G^*(\omega) \in \mathbb{C}$ instead of real elastic shear modulus $G \in \mathbb{R}$. Note that the complex modulus is also frequency dependent. This modification is performed on unconstrained matrix $\mathbf{K}_s^e$, so the three layer glass-polymer-glass beam has the following super element stiffness matrix

$$\mathbf{K}_r^e = \mathbf{T}^\mathsf{T} \mathbf{K}_s^e \mathbf{T}, \tag{5.99}$$

where

$$\mathbf{K}_s^e = \begin{pmatrix} \mathbf{K}_1^e & \mathbf{0} & \mathbf{0} \\ \mathbf{0} & \mathbf{K}_2^e(G_2^*(\omega)) & \mathbf{0} \\ \mathbf{0} & \mathbf{0} & \mathbf{K}_3^e \end{pmatrix}. \tag{5.100}$$

Matrices $\mathbf{K}_1^e$ and $\mathbf{K}_3^e$ are real and remain the same as in equation (5.78), while viscoelastic members are added in submatrix $\mathbf{K}_2^e$. This matrix can be decomposed into linear and nonlinear part but in this manner we first decompose the complex shear modulus, defined by equation (2.47), to arrive at

$$G^*(\omega) = \underbrace{G_\infty + \sum_{i=1}^{n} G_i}_{G_0} \underbrace{- \sum_{i=1}^{n} G_i \frac{1}{\omega^2 t_{c,i}^2 + 1} + \mathrm{i} \sum_{i=1}^{n} G_i \frac{\omega^2 t_{c,i}^2}{\omega^2 t_{c,i}^2 + 1}}_{G_\omega(\omega)}, \tag{5.101}$$

where G_0 is the frequency independent part and $G_\omega(\omega)$ is the complex, frequency dependent part. Then the stiffness matrix can be also decomposed to

$$\mathbf{K}_r(\omega) = \mathbf{K}_{r,0} + \mathbf{K}_{r,\omega}(\omega), \tag{5.102}$$

and further

$$\mathbf{K}_r(\omega) = G_0\mathbf{K}_{r,c} + G_\omega(\omega)\mathbf{K}_{r,c}, \tag{5.103}$$

where $\mathbf{K}_{r,c}$ is the matrix of constants. It is straightforward to show that matrix $\mathbf{K}^e_{r,0}$ is

$$\begin{pmatrix}
\frac{2(1+\nu)A}{L^e} & 0 & 0 & -\frac{2(1+\nu)A}{L^e} & 0 & 0 \\
0 & \frac{A^*}{L^e} & -\frac{A^*}{2} & 0 & -\frac{A^*}{L^e} & -\frac{A^*}{2} \\
0 & -\frac{A^*}{2} & \frac{A^*L^e}{4} + \frac{2(1+\nu)I_y}{L^e} & 0 & \frac{A^*}{2} & \frac{A^*L^e}{4} - \frac{2(1+\nu)I_y}{L^e} \\
-\frac{2(1+\nu)A}{L^e} & 0 & 0 & \frac{2(1+\nu)A}{L^e} & 0 & 0 \\
0 & -\frac{A^*}{L^e} & \frac{A^*}{2} & 0 & \frac{A^*}{L^e} & \frac{A^*}{2} \\
0 & -\frac{A^*}{2} & \frac{A^*L^e}{4} - \frac{2(1+\nu)I_y}{L^e} & 0 & \frac{A^*}{2} & \frac{A^*L^e}{4} + \frac{2(1+\nu)I_y}{L^e}
\end{pmatrix}. \tag{5.104}$$

Chapter 6

Dynamic analysis

In this section we use the finite element derived in section 5 to analyze the natural frequencies and damping of laminated glass beam.

6.1 Natural vibration analysis

Basic natural vibration is represented by equation (5.69), but it was derived based on not so strong assumptions, so we show the validity of this equation by a more general principle.

Theoretical physics, specifically Lagrangian mechanics, promotes such a way of view. Lagrangian mechanics can be used as general principle of mechanical systems. Lagrangian [22] is a special function of time, all generalized coordinates and all generalized velocities in general. For mechanical systems, there is mostly no time dependency and the Lagrangian is equal to the difference between the sum of kinetic energies and the sum of potential energies, so

$$\mathcal{L}(r_i, \dot{r}_i) = \sum_i E_k(\dot{r}_i) - \sum_i E_p(r_i), \tag{6.1}$$

where $\mathcal{L}(r_i, \dot{r}_i)$ is the Lagrangian. In our system no external forces are applied and the internal forces have character of a linear springs, so the potential energy is given as a sum of the elastic stored energies. Then, the Lagrangian is given as

$$\mathcal{L}(r_i, \dot{r}_i) = \sum_i \frac{1}{2} m_i \dot{r}_i - \sum_i \frac{1}{2} k_i r_i, \tag{6.2}$$

where r_i are generalized coordinates. We can imagine that each nodal degree of freedom in our system is one of the generalized coordinates and energies of this discrete system can be expressed via mass and stiffness matrices in quadratic form

$$\mathcal{L}(\boldsymbol{r}_m(t), \dot{\boldsymbol{r}}_m(t)) = \frac{1}{2} \dot{\boldsymbol{r}}_m(t)^{\mathsf{T}} \mathbf{M} \dot{\boldsymbol{r}}_m(t) - \frac{1}{2} \boldsymbol{r}_m(t)^{\mathsf{T}} \mathbf{K} \boldsymbol{r}_m(t), \tag{6.3}$$

where $\boldsymbol{r}_m$ is the vector of global master degrees of freedom. The Lagrange equation can be extended to more dimensions as well to give the form

$$\frac{\partial \mathcal{L}}{\partial \boldsymbol{r}_m} - \frac{d}{dt} \frac{\partial \mathcal{L}}{\partial \dot{\boldsymbol{r}}_m} = \mathbf{0}. \tag{6.4}$$

This equation is a general expression of a stationary condition of the system, which is described via Lagrangian $\mathcal{L}$. We can enforce the stationary condition by substituting the Lagrangian into the Lagrange equation. For case (6.3) we get

$$\frac{\partial \mathcal{L}}{\partial \boldsymbol{r}_m} - \frac{d}{dt}\frac{\partial \mathcal{L}}{\partial \dot{\boldsymbol{r}}_m} = -\mathbf{K}\boldsymbol{r}_m(t) - \frac{d}{dt}\mathbf{M}\dot{\boldsymbol{r}}_m(t) = -\mathbf{K}\boldsymbol{r}_m(t) - \mathbf{M}\ddot{\boldsymbol{r}}_m(t) = \mathbf{0}, \tag{6.5}$$

Therefore, we get the same result as earlier in equation (5.69).

$$\mathbf{K}\boldsymbol{r}_m(t) + \mathbf{M}\ddot{\boldsymbol{r}}_m(t) = \mathbf{0}. \tag{6.6}$$

This is the global equilibrium condition for our system and the solution of this equation describes its behavior. In the footsteps of classical vibration analysis [23] we prescribe time dependencies of unknowns as a dot product of a unit vector rotating in the complex plane and time independent amplitudes, so

$$\boldsymbol{r}_m(t) = e^{\mathrm{i}\omega t}\boldsymbol{r}_m. \tag{6.7}$$

By differentiating this expression we get the acceleration

$$\ddot{\boldsymbol{r}}_m(t) = -\omega^2 e^{\mathrm{i}\omega t}\boldsymbol{r}_m. \tag{6.8}$$

With these assumptions the general equation (6.6) is transformed into

$$\mathbf{K}\boldsymbol{r}_m(t) + \mathbf{M}\ddot{\boldsymbol{r}}_m(t) = \mathbf{K}\boldsymbol{r}_m - \omega^2\mathbf{M}\boldsymbol{r}_m = \left(\mathbf{K} - \omega^2\mathbf{M}\right)\boldsymbol{r}_m = \mathbf{0}. \tag{6.9}$$

We are searching for such $\boldsymbol{r}$ which satisfies equation (6.9), while $\boldsymbol{r}$ must be non trivial. From mathematical point of view it is the task of searching for eigenvalues. Equation (6.9) has two possible solutions depending on the bracket form. Either it does not have a solution or it has infinitely many solutions (not arbitrary). The second case is what we are looking for. To guarantee existence of a nontrivial solution the system of equations has to be singular and thus

$$\det\left(\mathbf{K} - \omega^2\mathbf{M}\right) = \mathbf{0}. \tag{6.10}$$

From this identity we can obtain eigen-values (i.e. modal frequencies) and then eigen-vectors (i.e. modal shapes) can be calculated from (6.9). Their evaluation can be relatively expensive but not impossible. The situation becomes more complicated if we include viscous interlayer. This is discussed in the next section.

6.2 Application to elastic-viscoelastic-elastic beams

Considering complex and frequency dependent stiffness matrix, the updated eigenvalue problem is provided by

$$\left(G_0\mathbf{K}_{r,c} + G_\omega(\omega)\mathbf{K}_{r,c} - \omega^2\mathbf{M}_r\right)\boldsymbol{r}_m = \mathbf{0}. \tag{6.11}$$

For a well-posed problem we must add a normalization condition. The form of this identity is not very important for the solution but can be important for the convergence. We used condition that eigen-vector belonging to the complex frequency must be perpendicular to real solution, taken from [24], written as

$$\boldsymbol{r}_0^{\mathsf{T}}\left(\boldsymbol{r}_m - \boldsymbol{r}_0\right) = 0, \tag{6.12}$$

where $\boldsymbol{r}_0$ is the real solution, that means the solution of the eigenvalue problem

$$\left(\mathbf{K}_{r,0} - \omega_0^2 \mathbf{M}_r\right) \boldsymbol{r}_0 = \mathbf{0}. \tag{6.13}$$

We can summarize our problem into the following three equations

$$\boxed{\begin{aligned} \left(\mathbf{K}_{r,0} + G_\omega(\omega)\mathbf{K}_{r,c} - \omega^2 \mathbf{M}_r\right) \boldsymbol{r}_m &= \mathbf{0}, && (6.14)\\ \boldsymbol{r}_0^{\mathsf{T}} \left(\boldsymbol{r}_m - \boldsymbol{r}_0\right) &= \mathbf{0}, && (6.15)\\ \left(\mathbf{K}_{r,0} - \omega_0^2 \mathbf{M}_r\right) \boldsymbol{r}_0 &= \mathbf{0}. && (6.16) \end{aligned}}$$

6.3 Numerical solution

We can assume that the solution of the third equation (6.16) can be evaluated analytically or numerically directly (from a mathematical software for example) and that we know its solution $\boldsymbol{r}_0$ and ω_0. Remaining two equations must be solved numerically employing complex numbers. We used the Newton method to solve it. We do not describe the principle of Newton method but it can be found in Appendix A. Employing the Newton method in each iteration step of the nonlinear problem $\boldsymbol{f}(\boldsymbol{x}) = \mathbf{0}$ we get the updating formula

$$\boldsymbol{x}^{(k+1)} = \boldsymbol{x}^{(k)} + \Delta\boldsymbol{x}^{(k+1)}, \tag{6.17}$$

where the increment is given by linearization

$$\mathbf{J}(\boldsymbol{x}^{(k)})\Delta\boldsymbol{x}^{(k+1)} = \boldsymbol{f}(\boldsymbol{x}^{(k)}). \tag{6.18}$$

Our system has two unknowns, scalar frequency ω (note that $\omega \in \mathbb{C}$) and eigenvector $\boldsymbol{r}_m$. The incremental equation for our system can be expressed as

$$\begin{pmatrix} \boldsymbol{r}_m^{(k+1)} \\ \omega^{(k+1)} \end{pmatrix} = \begin{pmatrix} \boldsymbol{r}_m^{(k)} \\ \omega^{(k)} \end{pmatrix} + \begin{pmatrix} \Delta\boldsymbol{r}_m^{(k+1)} \\ \Delta\omega^{(k+1)} \end{pmatrix}, \tag{6.19}$$

where the Jacobian matrix $\mathbf{J}$ can be obtained by differentiation the left hand side of equations (6.14) and (6.16). We get

$$\mathbf{J}(\boldsymbol{r}_m^{(k)}, \omega^{(k)}) = \begin{pmatrix} \mathbf{K}_r(\omega^{(k)}) - (\omega^{(k)})^2 \mathbf{M}_r & \left(\frac{\partial G_\omega}{\partial \omega}(\omega^{(k)})\mathbf{K}_c - \omega^{(k)} 2\mathbf{M}_r\right) \boldsymbol{r}_m^{(k)} \\ \boldsymbol{r}_0^{\mathsf{T}} & \mathbf{0} \end{pmatrix} \tag{6.20}$$

and the iterative process becomes

$$\mathbf{J}(\boldsymbol{r}_m^{(k)}, \omega^{(k)}) \begin{pmatrix} \Delta\boldsymbol{r}_m^{(k+1)} \\ \Delta\omega^{(k+1)} \end{pmatrix} = - \begin{pmatrix} \left(\mathbf{K}_r(\omega^{(k)}) - (\omega^2)^{(k)} \mathbf{M}_r\right) \boldsymbol{r}_m^{(k)} \\ \boldsymbol{r}_0^{\mathsf{T}} \left(\boldsymbol{r}_m^{(k)} - \boldsymbol{r}_0\right) \end{pmatrix}. \tag{6.21}$$

This iterative Newton process for nonlinear systems is illustrated in pseudo code in algorithm 1. We emphasize that this analysis is performed in the complex domain and the obtained frequency is also complex. Now, we need to get some relation between the complex number from the Newton iteration method and real natural frequency and damping. From numerical solution we have the i-th modal frequency in the complex expression

$$\omega_i^2 = a + \mathrm{i}b, \tag{6.22}$$

Algorithm 1: Newton method for solving eigenvalue problem, taken from [25]

Data:
Set tolerance ε;
Assemble $\mathbf{K}_0$, $\mathbf{K}_c$, $\mathbf{M}$;
Get $\boldsymbol{r}_0$, ω_0 solving $\left(\mathbf{K}_{r,0} - \omega_0^2 \mathbf{M}_r\right) \boldsymbol{r}_0 = 0$;
for *MODE i* **do**
  initialization: $k \leftarrow 0$, $\omega^{(0)} = \omega_0$, $\boldsymbol{r}^{(0)} = \boldsymbol{r}_0$;
  while $\varepsilon^{(k)} > \varepsilon$ **do**
    evaluate: $G_\omega(\omega^{(k)})$, $\frac{\partial G_\omega}{\partial \omega^k}$;
    get $\Delta\omega^{(k+1)}$, $\Delta\boldsymbol{r}^{(k+1)}$ by solving (6.21);
    update $\omega^{(k+1)} \leftarrow \omega^{(k)} + \Delta\omega(k+1)$;
    update $\boldsymbol{r}^{(k+1)} \leftarrow \boldsymbol{r}^{(k)} + \Delta\boldsymbol{r}(k+1)$;
    calculate $\varepsilon^{(k)} = \frac{||\left(\mathbf{K_r(\omega^{(k+1)})} - (\omega^{(k+1)})^2 \mathbf{M}\right)\boldsymbol{r}^{(k+1)}||_2}{||\boldsymbol{r}^{(k+1)}||_2}$;
    $k \leftarrow k+1$;
  end
  $\omega \leftarrow \omega^{(k)}$;
  $\boldsymbol{r}_m \leftarrow \boldsymbol{r}^{(k)}$;
end

where

$$a = \mathrm{Re}\left(\omega_i^2\right), \quad b = \mathrm{Im}\left(\omega_i^2\right). \tag{6.23}$$

We know that each point vibrates with the same angular frequency. Its displacement depend on time and can be expressed using the Euler identity as

$$r(t) = Ae^{\mathrm{i}\omega_i t}, \tag{6.24}$$

where A is the real initial amplitude. Now we can substitute our complex angular frequency in form $a + \mathrm{i}b$ into this equation to get

$$r(t) = Ae^{\mathrm{i}\sqrt[2]{a+\mathrm{i}b}t}. \tag{6.25}$$

Note the square root in the exponent. This is quite unpleasant but fortunately it usually holds $a \gg b$ for laminated glass with viscous interlayer. Therefore we can expand the square root function into the binomial series and take only the first two terms without loss of accuracy, so the expansion becomes

$$\sqrt[2]{a+\mathrm{i}b} = \sqrt[2]{a}\sqrt[2]{1+\mathrm{i}\frac{b}{a}} \approx \sqrt[2]{a}\left(1+\mathrm{i}\frac{b}{2a}\right). \tag{6.26}$$

We can substitute this approximation back into equation (6.25) to get

$$r(t) = Ae^{\mathrm{i}\omega t} = Ae^{\mathrm{i}\sqrt{a}t}e^{-\sqrt{a}(b/2a)t}. \tag{6.27}$$

The exponent in the first term is an imaginary number, so it corresponds to oscillatory properties of the system, meanwhile the exponent in the second term is real and corresponds to the amplitude decline in time, i.e. to the damping. It follows that the real

natural frequency is frequency of the first exponential term, so

$$\omega_i = \sqrt[2]{a} = \sqrt[2]{\mathrm{Re}(\omega_i^2)}, \tag{6.28}$$

where ω_i is real natural frequency of the i-th mode. Similarly we can investigate the value of damping. If we label the time dependent amplitude as B we get from (6.27) the following identity

$$B(t) = Ae^{-\alpha t} = Ae^{-\sqrt{a}(b/2a)t}, \tag{6.29}$$

where α is called the rate of exponential decay and for this case is equal to

$$\alpha = \sqrt[2]{a}\frac{b}{2a}. \tag{6.30}$$

Finally, in dynamic systems, damping is characterized via damping ratio [23], which is defined as a fraction of exponential decay rate and natural frequency, so for damping ratio ζ we get the following final identity

$$\zeta = \frac{\alpha}{\omega_i} = \sqrt[2]{a}\frac{b}{2a}\frac{1}{\sqrt[2]{\mathrm{Re}(\omega_i^2)}} = \sqrt[2]{a}\frac{b}{2a}\frac{1}{\sqrt[2]{a}} = \frac{b}{2a} = \frac{\mathrm{Im}(\omega_i^2)}{2\,\mathrm{Re}(\omega_i^2)}, \tag{6.31}$$

and if we define the loss factor as $\eta = b/a$ we get

$$\zeta = \frac{\eta}{2}. \tag{6.32}$$

This identity is derived with the assumption that $b \ll a$. This assumption is acceptable for damping up to 5%, but for more dampened systems, more accurate relationship must be employed. More accurate relation between the loss factor η and damping ratio ζ comes from [26]

$$\eta = 2\zeta\sqrt[2]{1-\zeta^2}. \tag{6.33}$$

In our case the first expression is sufficiently accurate and we utilize it in the modal analysis described in the next section.

Chapter 7

Validation

We have now prepared everything for the validation of our model via experiments. In this chapter we describe natural frequency experiments performed on laminated glass beams and we discuss the results presented in [25]. We also show comparison with the results from our numerical models.

7.1 Experiment setup

In this section we limit our attention to only one boundary condition of beam, namely free-free beam (without supports). To simulate these conditions, a laminated glass beam was suspended on a pair of soft strings as shown in Figure 7.1. Four beams were tested,

FIGURE 7.1: Experimental setup for simulation of free-free boundary conditions

two types of foils (EVA and PVB) and two types of glass plates (float glass and heat strengthened). Experiment scenario was the same for all of these specimens and it proceeded in the footsteps of [27]. A miniature piezoelectric accelerometer type 4519-003 was stick to one corner of the laminated glass plate. After that the sample was impacted by a impact hammer type 8206 at points placed evenly in grid 3x9 (27 points). From the accelerometer we obtained a set of frequency response functions and the post-processing software MEscopeVES extracted the modal parameters, specifically natural frequencies and half of bandwidth. Meaning of these parameters is illustrated in Figure 7.3, where energy is plotted as a function of frequency. In the post-processing software

the energy boundary for bandwidth is set to 3dB. If we denote half of the bandwidth as σit holds

$$2\sigma = \Delta\omega = \omega_2 - \omega_1 \ [\text{rads}^{-1}]. \tag{7.1}$$

Based on the solution of damped oscillator we can compute damping ratio by formula

$$\zeta = \frac{\sigma}{\sqrt[2]{\omega_c^2 + \sigma^2}} \ [\%]. \tag{7.2}$$

From the experiment we obtained first six modal shapes (three bending and three torsional) for each specimen, see Figure 7.2, showing the output from the post-processing software MEscopeVES. In the next section the results for EVA and PVB types of laminated glass are discussed individually. Numerical calculations were performed based on the model presented in the previous chapters.

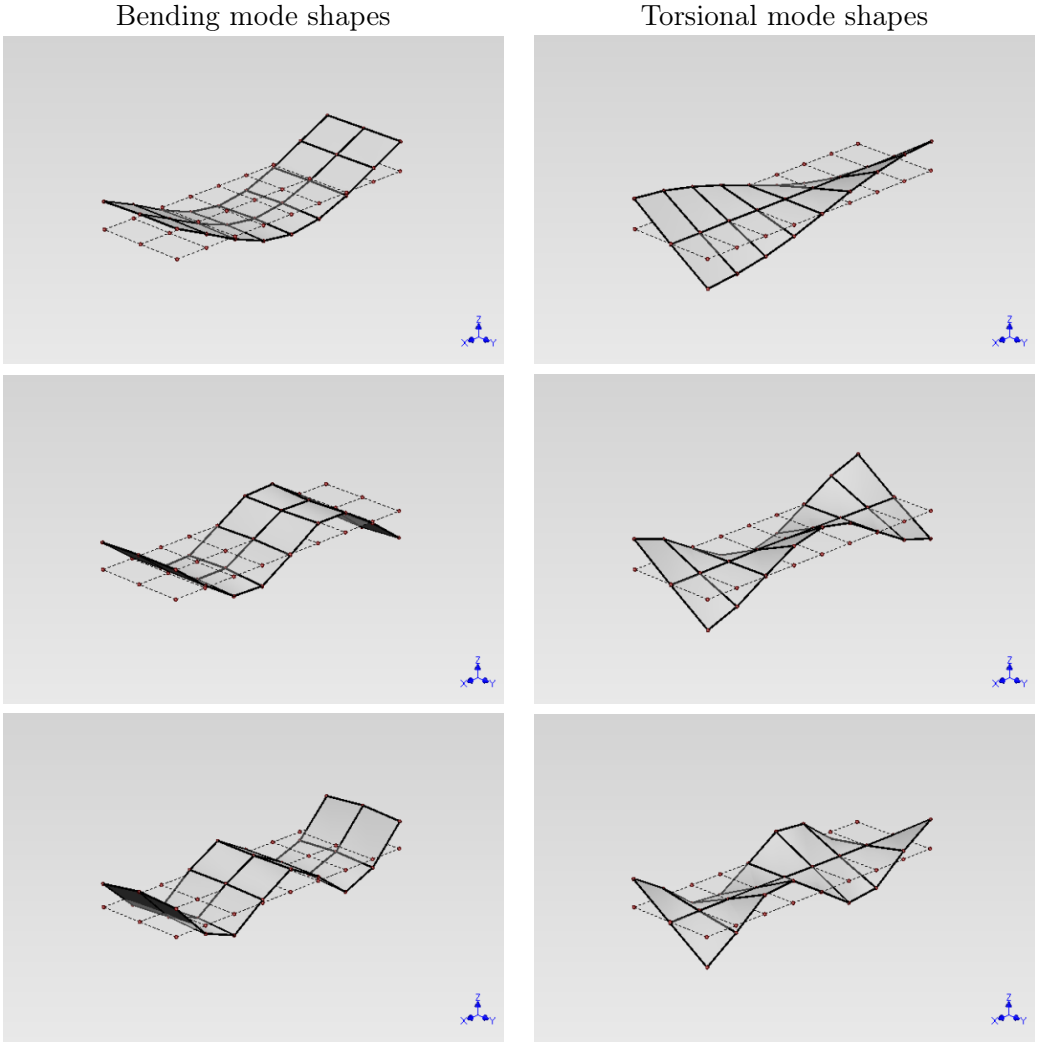

FIGURE 7.2: First six mode shapes from MEscopeVES software on tested 3x9 grid

Mechanical properties of solid glass layers are the same despite tempering process, so we consider that both types of glass plates (float glass and heat strengthened) are described by the same parameters, which are summarized in table 7.1, where density ρ and Poisson's ratio is taken from [28] and Young's modulus was measured by nano indentation using T750 Hysitron TriboIndenter in the Centre of Excellence Telč.

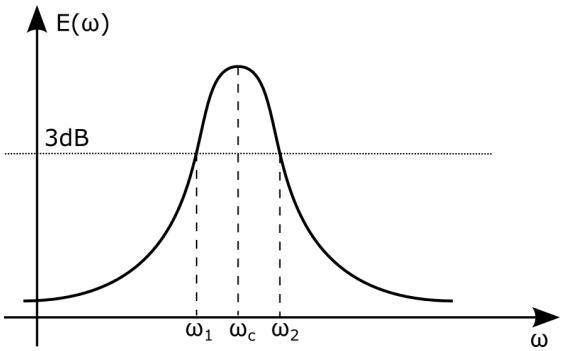

FIGURE 7.3: Bandwidth of damped system with 3dB level

Parameter	Label	Value
Density	$\rho_1 = \rho_3$ [kgm^{-3}]	2500
Young's modulus of elasticity	$E_1 = E_3$ [GPa]	76.6
Poisson's ratio	$\nu_1 = \nu_3$ [-]	0.22

TABLE 7.1: Mechanical properties of solid glass layers

7.2 EVA and PVB foil

Material parameters for the viscoelastic foil were taken from rheometer measurements by a processing calibration, see Chapter 3 and Chapter 4, and the resulting prony series and other fitted parameters are summarized in tables 7.2 and 7.3. Density is taken from the manufacturer and the reference temperature is set to 20°C.

Parameter	Label	EVA	PVB
Density	ρ_2 [kgm^{-3}]	950	1100
Long-term shear modulus	G_∞ [kPa]	1009	85.1
Poisson's ratio	ν_2 [-]	0.49	0.49
Reference temperature	T_0 [°C]	20	20
Parameter C_1	C_1 [-]	113	234
Parameter C_2	C_2 [°C]	404	1341

TABLE 7.2: Mechanical properties of EVA foil interlayer

EVA				PVB			
$t_{c,i}$	G_i[kPa]	$t_{c,i}$	G_i[kPa]	$t_{c,i}$	G_i[kPa]	$t_{c,i}$	G_i[kPa]
10^{-3}	1177	10^{4}	126	10^{-3}	952	10^{4}	132
10^{-2}	447	10^{5}	425	10^{-2}	869	10^{5}	28.9
10^{-1}	265	10^{6}	203	10^{-1}	2400	10^{6}	76.8
10^{0}	323	10^{7}	224	10^{0}	5010	10^{7}	47.5
10^{1}	267	10^{8}	206	10^{1}	2479	10^{8}	9.9
10^{2}	350	10^{9}	133	10^{2}	650	10^{9}	160
10^{3}	411	10^{10}	278	10^{3}	130		

TABLE 7.3: Prony series for EVA and PVB foils

Mode	Natural frequency [Hz]			Damping ratio [%]		
	EVA-HS	EVA-AN	EVA-NM	EVA-HS	EVA-AN	EVA-NM
1st bending	80.32	81.08	82.26	1.298	1.286	0.70
2nd bending	182.4	183.8	182.37	2.298	2.252	0.99
3rd bending	318.0	320.3	317.05	2.302	2.218	0.96

TABLE 7.4: Experiment and numerical results for laminated glass with EVA foil

Mode	Natural frequency [Hz]			Damping ratio [%]		
	PVB-HS	PVB-AN	PVB-NM	PVB-HS	PVB-AN	PVB-NM
1st bending	92.33	92.48	90.54	1.231	1.270	0.85
2nd bending	247.9	248.0	215.14	2.611	2.648	1.23
3rd bending	471.2	470.5	372.78	3.656	3.658	1.21

TABLE 7.5: Experiment and numerical results for laminated glass with PVB foil

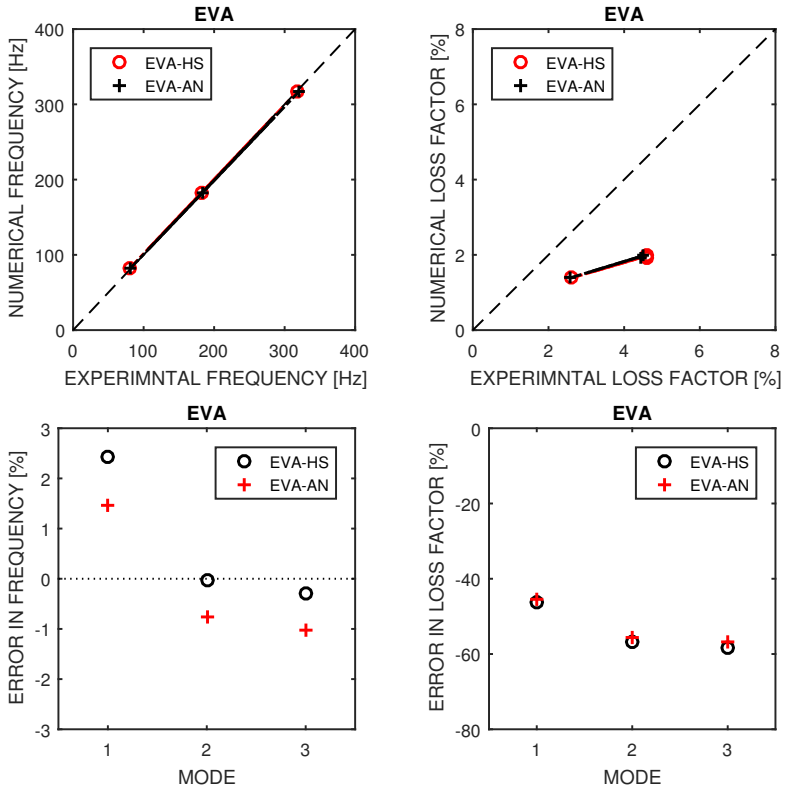

FIGURE 7.4: Quantile-quantile plots for storage and loss moduli of laminated glass with EVA foil and errors

The results from experiments and numerical calculations for both interlayer types are presented in tables 7.4 and 7.5, where only the bending modes are compared because the beam theory derived in Section 5 does not describe torsion effects. Suffix AN (Annealed glass) and HS (Heat strengthened) belongs to experiments and suffix NM means the Newton method, i.e. the method actually used in the analysis. The comparison of the results is provided in the form of graphs in Figures 7.4 and 7.5. The first row contains quantile-quantile plots for the storage and loss moduli, where the dashed line represents perfect match of experiments and numerical models. The second row presents errors of experiments due to computation model.

First, note that the experimentally obtained and computed natural frequencies relatively match each other. Although the third mode of laminated glass plate with PVB foil has high error, other cases have reasonable error. But it is not true for the estimation of loss factor (or damping ratio), where the relative difference between experiment and model goes up to 80%. These hight errors have several possible sources and are still under investigation. We plan to perform the same experimental modal analysis with a single monolithic glass to obtain the level of damping in hinges. The problem can be also in rheometer experiments because rheometer measures the storage and loss modulus with the same absolute error. Since the loss modulus is relatively small it is significantly less certain than the storage modulus. In future, we plan to develop approach, which could solve this issue.

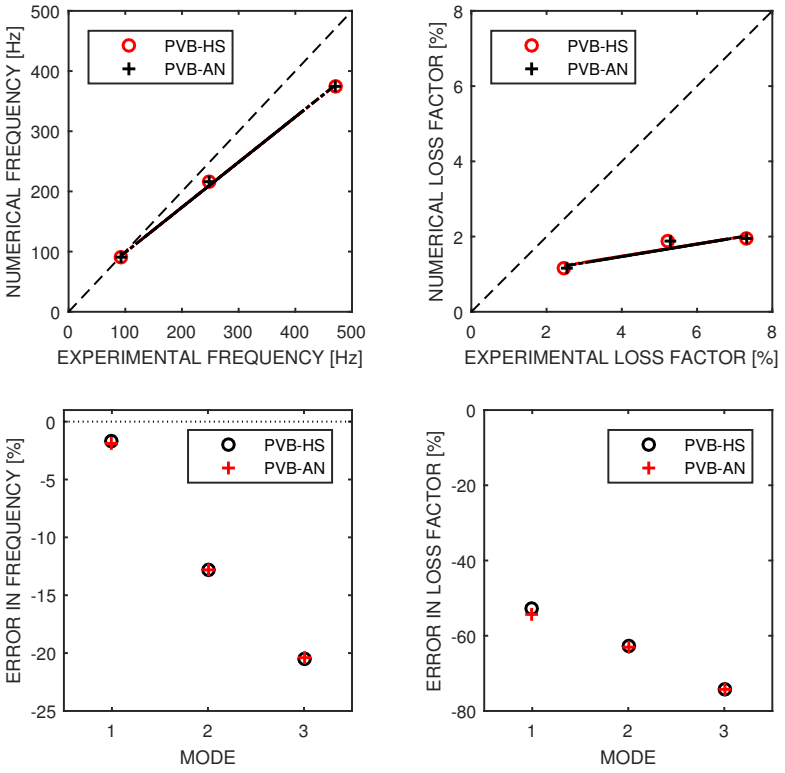

FIGURE 7.5: Quantile-quantile plots for storage and loss moduli of laminated glass with PVB foil and errors

Chapter 8

Conclusions

This chapter shortly summarizes the thesis and concludes what we have learned.

A brief history of glass and the path of laminated glass invention is introduced in chapter 1. The theory of viscoelasticity for modal analysis is outlined in chapter 2 where the integration of the temperature influence into the model is also introduced. Chapters 3 and 4 are focused on the rheometer experiments and post processing of the measurement data. The calibration of the Maxwell model from chapter 2 leads to fully described model for a viscous interlayer. The remainder of the text is a transition from the material point description to the analysis of laminated glass beams at a structural level. In chapter 5 the Mindlin beam element is derived and the super element for a three-layer beam with viscoelastic interlayer is assembled. These elements are used for dynamic natural vibration analysis in the next section and natural frequencies and loss factors are calculated by the Newton method. In the last chapter the validation of the model is performed against experimental measurements of unsupported beams. The thesis covers three main steps of research: A mathematical model for the material and the structure is defined first. Then experimental measurements are performed. Finally the model is compared to the experimental data to validate it.

The thesis is focused on creating laminated glass model suitable mainly for natural vibration analysis. However, extension to arbitrary temperature and time dependent case with a general right hand side is a relatively inexpensive matter. Major part of the thesis is about polymer viscoelasticity under harmonic loading and about calibration process because the material model of the polymer ply is an important component of structural analysis. In chapter 3, experimental setup for cylindric samples drilled out from laminated glass table is introduced. Rheometer device is not designed primarily for this type of experiment and modification of interpreting the data and measurement process is necessary. In chapter 3 an appropriate procedure is designed and transformation for software data is derived. In the next chapter the results for EVA and PVB type of polymer interlayer are presented and post processing is performed. Complex modulus G composed of storage modulus G' and loss modulus G'' is evaluated. Experimental data behave strangely for frequencies above 50 Hz. This was observed for all specimens regardless of the polymer type. This is probably caused by inaccuracy of the rheometer. Therefore only the data for lower frequencies were used for the calibration process for finding the Maxwell chain parameters. In thesis the calibration process is design and its results are presented. For PVB foil the calibration was accurate for fitting the storage modulus as well as the loss modulus. The model accurately describes the temperate

and time dependency of the foil. The EVA storage modulus calibration also gives a good match with the experimental data but the errors in the loss modulus are quite high. Moreover this type of polymer exhibits hysteresis and its parameters evolve with loading history. This phenomenon can not be described with the presented viscoelastic model. In future we plan to continue in the experimental research utilizing more accurate rheometer device.

The second part of the text employs the finite element method for natural vibration analysis of laminated glass beams. Investigation is focused on evaluating natural frequencies and damping parameters, i.e. the loss factor and the damping ratio. Chapter 5 derives the viscoelastic layer beam super element. This step reduces number of degrees of freedom and simplifies the analysis. In next two chapters natural vibration analysis is performed on laminated glass beams. Both the experimental program and numerical model are described, and the comparison of the numerical results with the measurements is presented in the last chapter. For prediction of natural frequencies, the model match the experiment and the errors are relatively low. For PVB foil error is up to 3%. For second type of interlayer, the results give small error for the first mode shape but for the second and third eigenvalues the error increases. For the third mode shape this value is about 20%. Taking into account that the first mode shape is the most important, these errors are acceptable. Higher errors order we get for prediction of damping. For both types of foil the error in loss factors was obtained about 40-70%. This phenomenon has not been explained by our model with calibrated parameters of the generalized Maxwell model from rheometer. In further investigation we focus on two possible effects that can negatively influence the model. First, the loss modulus is smaller by orders compared to the storage modulus and it is measured by rheometer with a higher absolute error. New rheometer measurements on cylindrical specimens may improve the loss modulus estimation and consequently it can improve the predicted damping at a structural level. Second, we assume that the solid glass does not dampen and the energy dissipation takes place only in the interlayer. We plan in future to performed similar modal analysis on a solid layer glass table and measure damping. It will show whether our assumption is valid or not. Further research will focus on the improvement of the mathematical description and on the accuracy improvement of the experimental process.

Appendix A

Newton methods

In thesis the Newton method is used in two versions. This appendix briefly shows, how this method works. We begin with the basic 1D Newton method for finding zero value of $f(x)$ (see A.1). In the next iteration step we find a point $x^{(s+1)}$, where the tangent line at $x^{(s)}$ is zero.

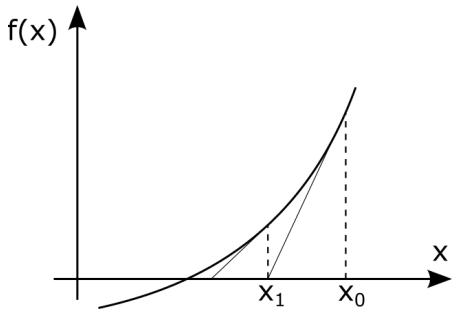

FIGURE A.1: Newton method graphically

So, for the next iteration step we get

$$x^{(s+1)} = x^{(s)} - \frac{f(x^{(s)})}{f'(x^{(s)})}. \tag{A.1}$$

We can extend this 1D problem to n-dimensional space, where we are looking for a zero value of a vector function $F(\boldsymbol{\beta})$, where $\boldsymbol{\beta}$ is an n-dimensional base vector. Inverse of the first derivative $f'(x)$ is extended to inverse of the Jacobian matrix, so we get

$$\boldsymbol{\beta}^{(s+1)} = \boldsymbol{\beta}^{(s)} - \mathbf{J}_{\mathsf{F}}^{-1}\boldsymbol{F}(\boldsymbol{\beta}^{(s)}), \tag{A.2}$$

where we want to find a vector $\boldsymbol{\beta}^*$ for which $\boldsymbol{F}(\boldsymbol{\beta}^*) = \mathbf{0}$ or at least $||\boldsymbol{F}(\boldsymbol{\beta}^*)||_2 < \varepsilon$. Value ε is a sufficient error. The Newton method in form (A.2) is used in chapter 6 for solving natural vibration problem, where the complex analysis is performed. But, it can be shown, that nothing changed when $\boldsymbol{\beta}$, $\boldsymbol{F}(\boldsymbol{\beta}) \in \mathbb{C}$. Chapter 3 also introduces a non-linear calibration problem, which is based on the Newton method. It is an optimization problem, so we do not want to find a zero point, but a minimal point (point, where the first derivative is zero). Consequently, the first order Jacobian matrix $\mathbf{J}$ is changed to

the second order Hessian matrix $\mathbf{H}$, so equation (A.2) can be rewrites as

$$\boldsymbol{\beta}^{(s+1)} = \boldsymbol{\beta}^{(s)} - \mathbf{H}_{\mathsf{F}}^{-1}\boldsymbol{f}(\boldsymbol{\beta}^{(s)}), \tag{A.3}$$

where

$$\boldsymbol{f}(\boldsymbol{\beta}^{(s)}) = \frac{\partial}{\partial \boldsymbol{\beta}}\boldsymbol{F}(\boldsymbol{\beta}^{(s)}). \tag{A.4}$$

This calibration process is an optimization problem in the form

$$F(\boldsymbol{\beta}) = \boldsymbol{r}^{\mathsf{T}}(\boldsymbol{\beta})\boldsymbol{r}(\boldsymbol{\beta}), \tag{A.5}$$

so we can substitute it into (A.4) to get

$$\boldsymbol{f}(\boldsymbol{\beta}) = \frac{\partial}{\partial \boldsymbol{\beta}}\boldsymbol{r}^{\mathsf{T}}(\boldsymbol{\beta})\boldsymbol{r}(\boldsymbol{\beta}) = 2\boldsymbol{r}^{\mathsf{T}}(\boldsymbol{\beta})\frac{\partial \boldsymbol{r}(\boldsymbol{\beta})}{\partial \boldsymbol{\beta}} \equiv 2\mathbf{J}_{\mathsf{r}}^{\mathsf{T}}(\boldsymbol{\beta})\boldsymbol{r}(\boldsymbol{\beta}), \tag{A.6}$$

and for the Hessian matrix $\mathbf{H}$ we obtain (for simplicity we use tensor notation)

$$H_{ij} = 2\sum_{i=1}^{m}\left(\frac{\partial r_i}{\partial \beta_j}\frac{\partial r_i}{\partial \beta_k} + r_i\frac{\partial^2 r_i}{\partial \beta_j \partial \beta_k}\right), \tag{A.7}$$

where the second order member is neglected and finally we arrive at the expression for the Hessian matrix

$$\mathbf{H}_F(\boldsymbol{\beta}) \approx 2\mathbf{J}_{\mathsf{r}}(\boldsymbol{\beta})^{\mathsf{T}}\mathbf{J}_{\mathsf{r}}(\boldsymbol{\beta}). \tag{A.8}$$

Putting all pieces together provides the final iteration identity for this method called the Gauss-Newton algorithm, so

$$\boldsymbol{\beta}^{(s+1)} = \boldsymbol{\beta}^{(s)} - \mathbf{H}_{\mathsf{F}}^{-1}(\boldsymbol{\beta}^{(s)})\boldsymbol{f}(\boldsymbol{\beta}^{(s)}) = \boldsymbol{\beta}^{(s)} - (\mathbf{J}_{\mathsf{r}}^{\mathsf{T}}(\boldsymbol{\beta}^{(s)})\mathbf{J}_{\mathsf{r}}(\boldsymbol{\beta}^{(s)}))^{-1}\mathbf{J}_{\mathsf{r}}^{\mathsf{T}}(\boldsymbol{\beta}^{(s)})\boldsymbol{r}(\boldsymbol{\beta}^{(s)}). \tag{A.9}$$

Appendix B

Gauss-Newton method for fitting

In this appendix the Jacobian of Gauss-Newton method for the calibration process is presented. If we have n cells in the generalized Maxwell chain and m is number of measurements, we get the following Jacobian matrix

$$\mathbf{J} = \begin{bmatrix} \frac{\partial r_1}{\partial G_1} & \cdots & \frac{\partial r_{2m}}{\partial G_1} \\ \vdots & \cdots & \vdots \\ \frac{\partial r_1}{\partial G_n} & \cdots & \frac{\partial r_{2m}}{\partial G_n} \\ \frac{\partial r_1}{\partial G_\infty} & \cdots & \frac{\partial r_{2m}}{\partial G_\infty} \\ \frac{\partial r_1}{\partial C_1} & \cdots & \frac{\partial r_{2m}}{\partial C_1} \\ \frac{\partial r_1}{\partial C_2} & \cdots & \frac{\partial r_{2m}}{\partial C_2} \end{bmatrix}, \tag{B.1}$$

where for $j \in \langle 1, m \rangle$ it holds

$$\frac{\partial r_j}{\partial G_i} = \frac{(a_T \omega_j)^2 t_{c,i}^2}{(a_T \omega_j)^2 t_{c,i}^2 + 1}, \tag{B.2}$$

$$\frac{\partial r_j}{\partial G_\infty} = 1, \tag{B.3}$$

$$\frac{\partial r_j}{\partial C_1} = \sum_{i=1}^{n} G_i \frac{2 a_T \omega_j^2 t_{c,i}^2}{\left(a_T^2 \omega_j^2 t_{c,i}^2 + 1\right)^2} \frac{\partial a_T}{\partial C_1}, \tag{B.4}$$

$$\frac{\partial r_j}{\partial C_2} = \sum_{i=1}^{n} G_i \frac{2 a_T \omega_j^2 t_{c,i}^2}{\left(a_T^2 \omega_j^2 t_{c,i}^2 + 1\right)^2} \frac{\partial a_T}{\partial C_2}, \tag{B.5}$$

and for $j \in \langle m+1, 2m \rangle$

$$\frac{\partial r_j}{\partial G_i} = \frac{a_T \omega_j t_{c,i}}{(a_T \omega_j)^2 t_{c,i}^2 + 1}, \tag{B.6}$$

$$\frac{\partial r_j}{\partial G_\infty} = 1, \tag{B.7}$$

$$\frac{\partial r_j}{\partial C_1} = \sum_{i=1}^{n} G_i \frac{\omega_j t_{c,i}(1 - a_T^2 \omega_j^2 t_{c,i}^2)}{\left(a_T^2 \omega_j^2 t_{c,i}^2 + 1\right)^2} \frac{\partial a_T}{\partial C_1}, \tag{B.8}$$

$$\frac{\partial r_j}{\partial C_2} = \sum_{i=1}^{n} G_i \frac{\omega_j t_{c,i}(1 - a_T^2 \omega_j^2 t_{c,i}^2)}{\left(a_T^2 \omega_j^2 t_{c,i}^2 + 1\right)^2} \frac{\partial a_T}{\partial C_2}. \tag{B.9}$$

And where

$$\frac{\partial a_T}{\partial C_1} = a_T(T) \frac{T_R - T}{C_2 + T - T_R} \ln 10, \tag{B.10}$$

$$\frac{\partial a_T}{\partial C_2} = a_T(T) \frac{C_1(T - T_R)}{(C_2 + T - T_R)^2} \ln 10. \tag{B.11}$$

The Gauss-Newton method algorithm is written in pseudo code in algorithm table 2.

Algorithm 2: Gauss-Newton method for solving calibration problem

Data:
Set tolerance ε;
Set initial guess $\boldsymbol{\beta}_0$;
initialization: $k \leftarrow 0$, $\boldsymbol{\beta}^{(0)} = \boldsymbol{\beta}_0$;
while $\varepsilon^{(k)} > \varepsilon$ **do**
  evaluate: $\mathbf{J}_r(\boldsymbol{\beta}^{(k)})$;
  evaluate residuum $\boldsymbol{r}(\boldsymbol{\beta}^{(k)})$;
  update $\boldsymbol{\beta}^{(k+1)} \leftarrow \boldsymbol{\beta}^{(k)} - \left(\mathbf{J}_r^{\mathsf{T}}(\boldsymbol{\beta}^{(k)})\mathbf{J}_r(\boldsymbol{\beta}^{(k)})\right)^{-1} \mathbf{J}_r^{\mathsf{T}}(\boldsymbol{\beta}^{(k)})\boldsymbol{r}(\boldsymbol{\beta}^{(k)})$;
  calculate $\varepsilon^{(k)} = ||\boldsymbol{\beta}^{(k+1)} - \boldsymbol{\beta}^{(k)}||_2$;
  $k \leftarrow k + 1$;
end
$\boldsymbol{\beta} \leftarrow \boldsymbol{\beta}^{(k)}$;

Bibliography

[1] Ch. O'Regan. *Structural use of glass in buildings.* IStructE Ltd, London, 2014.

[2] J. Wurm. *Glass Structures: Design and Construction of Self-supporting Skins.* Boston, 2007.

[3] C.E. Inglis. Stresses in a plate due to the presence of cracks and sharp corners. *Transactions of the Institute of Naval Architects*, 55:219–242, 1913.

[4] M. Haldimann, A. Luible, and M. Overend. *Structural Use of Glass.* IABSE, Switzerland, 2008.

[5] W. Flligge. *Viscoelasticity.* Springer, Berlin, 1975.

[6] L. Galuppi and G. F. Royer-Carfagni. Effective thickness of laminated glass beams: New expression via a variational approach. *Engineering Structures*, 38(Supplement C):53 – 67, 2012.

[7] M. López-Aenlle and F. Pelayo. Dynamic effective thickness in laminated-glass beams and plates. *Composites Part B: Engineering*, 67(Supplement C):332 – 347, 2014.

[8] J. Schmidt, A. Zemanová, T. Janda, J. Zeman, and M. Šejnoha. Variationally-based effective dynamic thickness for laminated glass beams. *Conference Nano and Macro Mechanics*, 2017.

[9] A. Zemanová. *Numerical modeling of laminated glass structures.* Ph.D. Thesis, CTU in Prague, 2014.

[10] I.M. Ward and J. Sweeney. *An Introduction to the Mechanical Properties of Solid Polymers.* Wiley, 2004.

[11] K. Rektorys. *Survey of Applicable Mathematics.* MIT Press, 1969.

[12] M. L. Williams, R. F. Landel, and J. D. Ferry. The temperature dependence of relaxation mechanisms in amorphous polymers and other glass-forming liquids. *Journal of the American Chemical Society*, 77(14):3701–3707, 1955.

[13] R. Giovanna, F. Zulli, L. Andreozzi, and M. Fagone. Test methods for the determination of interlayer properties in laminated glass. *Journal of Materials in Civil Engineering*, 29(4):04016268, 2017.

[14] L. Andreozzi, S.B. Bati, M. Fagone, G. Ranocchiai, and F. Zulli. Dynamic torsion tests to characterize the thermo-viscoelastic properties of polymeric interlayers for laminated glass. *Construction and Building Materials*, 65:1–13, 2014.

[15] S. Timoshenko. *Theory of elasticity.* McGraw-Hill, 2001.

[16] T. Janda, A. Zemanová, J. Zeman, and M. Šejnoha. Finite element models for laminated glass units with viscoelastic interlayer for dynamic analysis. *High Performance and Optimum Design of Structures and Materials II*, 2016.

[17] J. Schmidt, T. Janda, and M. Šejnoha. Calibration of model for laminated glass polymer interlayer based on rheometer data. *55th Conference on experimental stress analysis*, 2017. Novy Smokovec, Slovakia.

[18] Z. Bittnar and J. Šejnoha. *Numerical Methods in Structural Mechanics.* Faculty of Civil Engineering. CTU in Prague, 1996.

[19] O.C. Zienkiewicz and R.L. Taylor. *The Finite Element Method: Solid mechanics.* Referex collection.Mecánica y materiales. Butterworth-Heinemann, 2000.

[20] A. Zemanová, J. Zeman, and M. Šejnoha. Finite element model based on refined plate theories for laminated glass units. *Latin American Journal of Solids and Structures*, 15:1158 – 1180, 2015.

[21] A. Jaubert. *Numerical free vibration analysis of laminated glass.* Master Thesis, Aarhus University, 2016.

[22] L. D. Landau and E. M. Lifshitz. *Mechanics, Third Edition: Volume 1 (Course of Theoretical Physics).* Butterworth-Heinemann, 1976.

[23] R. Clough and J. Penzien. *Dynamics of Structures.* Computers and Structures, Inc., Berkeley, 1995.

[24] E. Daya and M. Potier-Ferry. Numerical method for nonlinear eigenvalue problems application to vibrations of viscoelastic structures. 79:533–541, 2001.

[25] A. Zemanová, T. Plachý, J. Schmidt, T. Janda, J. Zeman, and M. Šejnoha. Numerical and experimental modal analysis of laminated glass beams. *International Conference Dynamical Systems - Theory and Applications*, 2017. Lodz, Poland.

[26] W. Liu. *Experimental and analytical estimation of damping in beams and plates with damping treatments.* Ph.D. Thesis, University of Kansas School of Engineering, 2008.

[27] S. Lenci, L. Consolini, and F. Clementi. On the experimental determination of dynamical properties of laminated glass. 7:27–43, 2015.

[28] CEN/TC 129. Draft prEN 16612: Glass in building - determination of the load resistance of glass panes by calculation and testing. Technical report, 2013.